A STUDY OF DONOR-ACCEPTOR INTERACTIONS IN π-GELS AND π-CONJUGATED POLYMERS

Thesis Submitted to AcSIR for the Award of the Degree of
DOCTOR OF PHILOSOPHY
in Chemical Sciences

By

VISHNU S.

Registration No: 10CC11J39011

Under the guidance of

Dr. A. AJAYAGHOSH

CSIR-NATIONAL INSTITUTE FOR INTERDISCIPLINARY SCIENCE AND TECHNOLOGY (CSIR-NIIST)
THIRUVANANTHAPURAM-695 019, KERALA, INDIA

June, 2017

DECLARATION

I hereby declare that the matter embodied in the thesis entitled: "**A Study of Donor-Acceptor Interactions in π-Gels and π-Conjugated Polymers**" is the result of the investigations carried out by me at the Photosciences and Photonics Section, Chemical Sciences and Technology Division, CSIR-National Institute for Interdisciplinary Science and Technology (CSIR-NIIST), Thiruvananthapuram, under the supervision of Dr. A. Ajayaghosh and the same has not been submitted elsewhere for any other degree.

In keeping with the general practice of reporting scientific observations, due acknowledgement has been made wherever the work described is based on the findings of other investigators.

Vishnu S.

Thiruvananthapuram
12-06-2017

राष्ट्रीय अंतर्विषयी विज्ञान तथा प्रौद्योगिकी संस्थान
वैज्ञानिक तथा औद्योगिक अनुसंधान परिषद्
इंडस्ट्रियल इस्टेट पी.ओ., पाप्पनंकोड, तिरुवनंतपुरम, भारत-695 019
CSIR-NATIONAL INSTITUTE FOR INTERDISCIPLINARY SCIENCE & TECHNOLOGY (CSIR-NIIST)
Council of Scientific & Industrial Research
Industrial Estate P.O., Pappanamcode, Thiruvananthapuram, India-695 019
डॉ. ए. अजयघोष एफएनए, एफटीडब्ल्यूएस
निदेशक
Dr. A. Ajayaghosh FNA, FTWAS
Director

12-06-2017

CERTIFICATE

This is to certify that the work embodied in this Ph. D. thesis entitled "**A Study of Donor-Acceptor Interactions in π-Gels and π-Conjugated Polymers**" submitted by **Mr. Vishnu S.** to Academy of Scientific and Innovative Research (AcSIR), in partial fulfilment of the requirements for the award of the **Degree of Doctor of Philosophy in Chemical Sciences**, has been carried out under my supervision and guidance at the Photosciences and Photonics Section, Chemical Sciences and Technology Division of the CSIR-National Institute for Interdisciplinary Science and Technology (CSIR-NIIST), Thiruvananthapuram. I further certify that this work has not been submitted to any other University or Institution in part or full for the award of any degree or diploma.

A. Ajayaghosh
(Thesis Supervisor)

ACKNOWLEDGEMENTS

It is with great pleasure that I extend my deep sense of gratitude to Dr. A. Ajayaghosh, my thesis supervisor, for suggesting the research problem, for his valuable guidance, support and encouragement, leading to the successful completion of this work.

I would like to express my gratitude to Prof. M. V. George for being an inspiration.

I thank Dr. Suresh Das former Director and Dr. Gangan Pratap, former Acting Director of the CSIR-National Institute for Interdisciplinary Science and Technology (CSIR-NIIST), Thiruvananthapuram, for providing the necessary facilities for carrying out this work.

My sincere thanks are also due to:

- ✓ *Dr. D. Ramaiah, Dr. K. R. Gopidas, Dr. Narayanan Unni, Dr. Joshy Joseph, Dr. K. Yoosaf, Dr. C. Vijayakumar, Dr. B. Deb and Dr. V. Karunakaran, present and former scientists of the Photosciences and Photonics Section, Chemical Sciences and Technology Division, for their help and support.*
- ✓ *Dr. R. Luxmi Varma, AcSIR co-ordinator.*
- ✓ *Dr. K. R. Gopidas, Dr. Joshy Joseph, Dr. Ravi Shankar L., who are my DAC members.*
- ✓ *Dr. J. D. Sudha and Dr. V. K. Praveen, for their support and fruitful discussions.*
- ✓ *Prof. Deqing Zhang, Dr. Guanxin Zhang and Dr. Zitong Liu, Institute of Chemistry Chinese Academy of Sciences (ICCAS), China, for their help and support.*
- ✓ *Dr. S. Srinivasan, Dr. S. Prasanthkumar, Dr. K. P. Divya, Dr. G. Anesh, Dr. K. Kartha, Dr. P. Anees and Dr. Manoj, former members of the Photosciences and Photonics Section, for their support and advice.*
- ✓ *Dr. R. K. Mishra, Dr. Manas Panda, Dr. Sreejith Sankar, Mr. R. Thirumalai, Mr. A. Sandeep, Dr. B. Vedhanarayanan, Dr. R. D. Mukhopadhyay, Dr. Divya. S. Philips, Mr. C. Sandeep, Mr. S. Ghosh, Mr. K. V. Sudheesh, Mr. A. Mal, Mr. M. Hifsudheen, Mr. S. Das, Mr. G. Das and Dr. R. Ramakrishnan for their help and cooperation.*
- ✓ *Mr. Chandrakanth C. K. for SEM analysis and Mr. Robert Philip and Mr. M. Kiran for TEM analysis.*

- ✓ *Mr. J. S. Kiran for his general help and support.*
- ✓ *Ms. M. Saumini, Mr. Adarsh, Mr. P. Preethanuj, Mr. T. Arun, Mr. Saran P., and Mr. R. Gokul for NMR and Ms. S. Viji and Ms. Aathira for mass spectral analyses.*
- ✓ *All my teachers for their encouragement at different stages of my academic career.*
- ✓ *Council of Scientific and Industrial Research (CSIR), Government of India for Research fellowship.*

I am deeply and forever indebted to my parents and brother for their constant source of love, inspiration and blessings. Finally I would like to thank my friends and relatives for their excellent support and encouragement.

Vishnu S.

CONTENTS

CHAPTER 2

CHAPTER 3

CHAPTER 4

PREFACE

Donor-acceptor π-conjugated systems are potential components of advanced functional materials, whose performance are significantly influenced by the nanoscale organization of supramolecular building blocks. Various inter and intramolecular interactions in the multicomponent π-conjugated molecular systems control the mechanism, nature and output of the functional supramolecular assembly. Chapter 1 has been provided with an overview of the research developments on the supramolecular control over the functional properties of π-conjugated systems. Finally the objective and outline of the present thesis are given. In addition, specific objectives of the present thesis are briefly described at the end of Chapter 1.

Gelation and crystallization are two non-equilibrium supramolecular processes. Hence gel phase crystallization offers a unique opportunity to understand these orthogonal supramolecular processes. Viscous ambiance in the three-dimensional gel matrix slows down the diffusion of the crystallizing units. Self-sorting and hetero-assembly are the two possible outcomes from these multicomponent systems. Depending upon the degree of coupling between the gelator and crystallizing unit, these non-equilibrium processes influences or modifies the final outcome of the molecular assembly. Among the various π-conjugated small molecular gelators, oligo(*p*-phenylenevinylene)s (OPV) occupies a distinct position due to its excellent optoelectronic properties. Crystalline molecular assembly of π-conjugated systems such as fullerenes has significant importance in view of their electronic applications. Second chapter of the thesis demonstrate the heterogeneous

crystallization of C_{60} at OPV based gel interface. Viscous π-gel medium acts as platform for the effortless crystallization of C_{60}. The eventual morphological outcome of the gel phase crystallization and its influence on the functional optoelectronic properties have been studied in details.

It is quite difficult to predict and control the molecular assembly in multicomponent supramolecular systems. Functional group engineering is one of the mostly adopted methods to decide whether self-sorting or mixing of components will occur. In the third chapter we have used acid-pyridine complementary interaction to construct functional co-assembly from oligo(*p*-phenylenevinylene) derivative (**OPV-P**) and perylenebisimide derivative (**PBI-A**). Various spectroscopic and microscopic analyses have used to study the difference in the thermo-mechanical stability and nanoscopic morphology. Complementary interaction between the π-conjugated systems facilitates directional and ordered arrangement of the aromatic cores in the multicomponent supramolecular assembly. This morphological feature favours efficient charge carrier transport. Influence of the supramolecular co-assembly on the conducting properties of the multicomponent system is analysed in detail using four probe conductivity method and conductive atomic force microscopic technique.

Semiconducting properties of donor-acceptor (D-A) π-conjugated polymers significantly depend on the molecular packing in the solid state. Inter- as well as intra molecular interactions in the polymer chain increases its self-assembling ability, which in turn enhances the π-π overlap of adjacent monomer units. Closely packed aromatic stacking with efficient π-electron delocalization and effective charge transportation can be achieved by incorporating rigid and planar monomer units in the semiconductor backbone. Fused

aromatic rings with chalcogen atoms are one of the most used classes of molecules to enhance the molecular rigidity of π-conjugated polymer backbone. Benzothieno [3,2-*b*][1]-benzothiophene (BTBT) is one of the promising fused chalcogenophenes, which facilitates efficient intrinsic charge carrier mobility by reducing the reorganization energy and increasing the transfer integral. Diketopyrrolopyrrole (DPP) occupies a unique position among various electron acceptors used for the construction of numerous efficient molecules having organic field effect transistors (OFET) application. In the last chapter, influence of the aromatic planar rigid core on the molecular packing and OFET performance of the semiconducting polymers has been studied in details. Different percentage of BTBT core is incorporated into DPP based low band gap polymers and its FET mobility has explained with respect to the nature of molecular packing in the film state.

References

1. A π-Gel Scaffold for Assembling Fullerene to Photoconducting Supramolecular Rods. **Nair**, **V. S.**, Mukhopadhyay, R. D., Saeki, A., Seki, S., Ajayaghosh, A. *Sci. Adv*. **2016**, *2*, e1600142.
2. Conjugated Random Donor-Acceptor Copolymers of [1]Benzothieno[3,2-*b*] benzothiophene and Diketopyrrolopyrrole Units for High Performance Polymeric Semiconductor Applications. **Nair**, **V. S.**, Sun, J., Qi, P., Yang, S., Liu, Z., Zhang, D., Ajayaghosh, A. *Macromolecules*, **2016**, *49*, 6334-6342.
3. Supramolecular Co-assembly of π-Gelator and *n*-type Semiconductor Controlled by Acid-Pyridine Interaction. **Nair, V. S.**, Ajayaghosh, A. (Manuscript under preparation).

Chapter 1

Supramolecular Interactions and Functional Properties of π-Conjugated Donor-Acceptor Systems: An Overview

1.1. Abstract

In recent times π-conjugated donor-acceptor systems are widely used as potential components for advanced functional materials. Optoelectronic properties of these systems are significantly influenced by the supramolecular organization of the π-chromophores. Functional group engineering offers a facile way to gain control over the mechanism, nature and output of the supramolecular assembly by introducing various inter- and intramolecular interactions. Therefore, detailed understanding of the supramolecular assembly of the π-conjugated systems, through various non-covalent interactions are necessary to the design of supramolecular functional materials. In this chapter, an overview of the recent developments on the supramolecular control over the functional properties of π-conjugated systems is provided. Finally, the objective and outline of the present thesis are given.

1.2. Introduction

Extensive linear overlapping of p_z orbitals in π-conjugated systems results in profound delocalization of electrons throughout the aromatic backbone, which make them efficient candidates for the optoelectronic applications.[1-4] In contrary to the inorganic counterparts, high extinction coefficient and high photoluminescence

quantum efficiency are additional advantages for π-conjugated systems. Hybrid systems from π-conjugated donor-acceptor components can act as an active medium for electron and/or energy transfer processes. Delocalized π-electron cloud and low band gap enables effective transport of both negative and positive charge carriers along the π-backbone.[3,5] These features make π-conjugated molecules potential candidates for optoelectronic devices such as light emitting diodes (LEDs), field effect transistor (FETs) and photovoltaic devices (PVDs).[1-5]

Efficiency of these optoelectronic devices are significantly influenced by the nanoscale organization of the functional molecules. "Bottom-up" self-assembly is one of the promising approaches to gain control over the molecular aggregation behaviour and its functional properties. Functional molecular assembly can be guided by various supramolecular interactions such as hydrogen bonding, π-π stacking, van der Waals or dipole interactions etc.[6]

1.3. Supramolecular Interactions

Dynamic non-covalent interactions between molecules are efficient tools for the construction of smart functional nanostructures. Reversible nature of these interactions facilitates self-correction in the assembly process, providing better control over size, shape and optoelectronic properties. Compared to the covalent bonds, non-covalent forces are weak and highly dependent on the environmental parameters, such as the temperature, concentration, time etc. Hydrogen bonding, π-π stacking, electrostatic, van der Waals interactions are the most exploited

supramolecular interactions for the construction of functional molecular assembly of π-conjugated systems.[7-9]

Hydrogen bond is formed between the hydrogen attached to an electronegative donor atom and an acceptor atom with lone pair of electrons. Among the non-covalent interactions, hydrogen bonding is the favorite in the supramolecular chemistry due to its tunable strength, directionality and specificity. π-π interaction arise due to the weak electrostatic interaction between the aromatic rings. Electrostatic interactions are basically, ion-ion, ion-dipole and dipole-dipole interactions, which arise due to the delocalization of charges on π-conjugated systems. Temporary polarization of an electron cloud by an adjacent nucleus is responsible for the van der Waals interactions, which is usually non-directional and can be of attractive or repulsive in nature. In most of the cases, more than one such supramolecular interaction determines the pathway of molecular self-assembly as well as the functional properties of the resulting supramolecular nanostructures.

1.4. Effect of Supramolecular Interactions on Functional Properties of π-Conjugated Donor-Acceptor Systems

Supramolecular interaction in donor-acceptor π-conjugated systems is one of the widely studied topics as a result of the success of "bulk heterojunction" concept. Functional properties of these blend systems depend on the intermolecular interaction between the components and eventually on the nanoscopic morphology. There has been lot of attempts to tailor the functional properties of π-conjugated systems by controlling the supramolecular interactions. In the following sections, structure-

property relationships of various π-conjugated systems are described with suitable examples.

1.4.1. Effect of Supramolecular Interactions on Functional Properties of π-Conjugated Small Molecules

Shape defined nanomaterials of π-conjugated systems have potential electronic and photonic applications, since original electrical and optical properties are expected to be enhanced or systematically modulated according to their geometries. Ariga et al. have demonstrated controlled formation of C_{60} based nanostructures by simple solvent engineering method (Figure 1.1a-c).[10] This is due to the solvent controlled three-dimensional π-π interaction between the aromatic cores. 1D crystalline C_{60} nanowires with an aspect ratio up to 3000 was grown from a 1,2,4-trimethylbenzene solution.[11]

Choi et al. have demonstrated the critical correlation between the solvent and the final geometry of the C_{60} self-assembly. Substrate-independent self-assembly of C_{60} can form disc, wire and dot structures of C_{60} by the simple drop-drying process (Figure 1.1d-f).[12] This observation can be ascribed to the difference in the stabilization energy required for solvent-specific self-assembly. These micro-crystalline assemblies of C_{60} can retain the optoelectronic properties of the parent aromatic system.

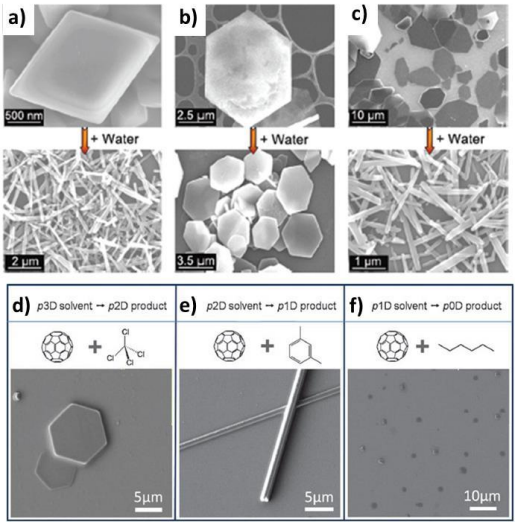

Figure 1.1. SEM images of structural transformation of 2D C_{60} nanosheets using solvent engineering a) nanorhombus (from *tert*-butyl alcohol/toluene) to nanorod, b) nanohexagon (from isopropyl alcohol/CCl_4), and c) mixed polygon (from *tert*-butyl alcohol/benzene) to nanorod. SEM images of C_{60} crystals from d) CCl_4, e) *m*-xylene and f) hexane.

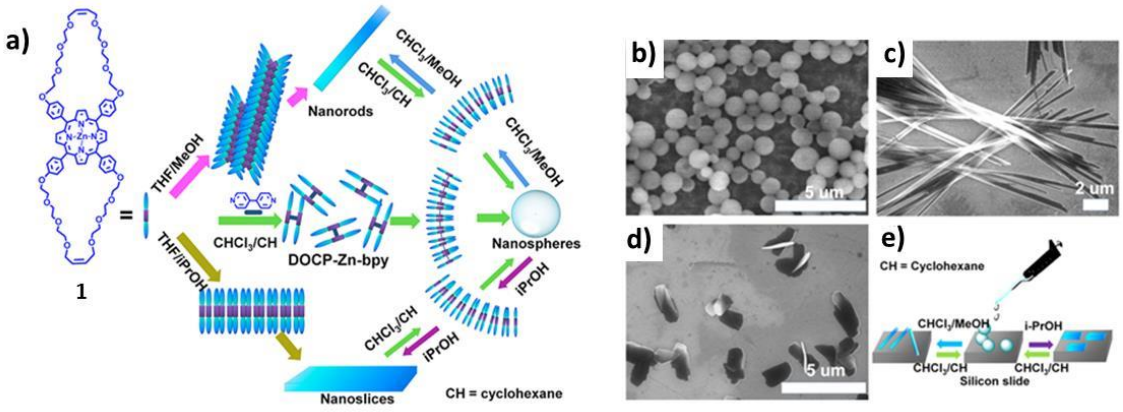

Figure 1.2. a) Schematic representation of aggregation mechanism of **1**. SEM images of the nanostructures of **1**.bpy complex in b) $CHCl_3$/cyclohexane, c) $CHCl_3$/methanol, d) isopropyl alcohol and e) scheme of experimental procedure.

Solution based dynamic molecular self-assembly depends on the subtle balance between molecule-molecule interaction and the molecule-solvent interaction. Selection of solvents and the solvent composition have dramatic influence on the self-

assembled nanostructures. For instance, the axially coordinated complex of dioctaoxacylo-porphyrin zinc (**1**) complex with 4,4′-bipyridine can self-assemble to different patterns depending on the solvent composition.[13] Driving force for the self-assembly comes from the interaction between the porphyrins rings, π-π interaction and hydrogen bonding. Co-ordination complex of the molecule **1** form nanorod structure in tetrahydrofuran/methanol solution, whereas self-assembly from tetrahydrofuran/isopropanol solution resulted in nanoslices (Figure 1.2). Due to its high volatile nature, methanol favours fast self-assembly process leading towards the formation of 1D nanorods, which possess high optical waveguide property compared to the nanoslices.

Zhang and co-workers have reported controlled aggregation behaviour of 9,10-diphenylanthracene (DPA) by surfactant assisted reprecipitation method to convert nanospheres to nanowires.[14] These nanowires were proven to be good for heterojunction light emitting diode (LED) devices. Surfactants having weak dipole-dipole interactions with DPA, hardly affect the aggregation mechanism of DPA which results in the formation of extended crystalline nanostructures. However, surfactants having strong π-π interactions with DPA form amorphous nanostructures due to the perturbation in the self-assembly process.

In general electrical properties of π-conjugated systems depend upon the conjugation length as well as the processing conditions. Stupp et al. have demonstrated the role of self-assembling conditions in conductivity of oligothiophene derivative (**2**).[15] Thin film of **2** made from chlorobenzene solution showed hole mobility of $9.9 \pm 1.7\times10^{-6}$ Scm^{-1}, which was comparable to that of poly (3-

hexylthiophene) film in identical experimental conditions (Figure 1.3). Extended hydrogen bonding and π-π stacking between the thiophene rings are responsible for the conducting supramolecular 1D nanostructure. This is confirmed by the negligible conductivity of the film cast from chloroform, which does not promote extensive self-assembly. Bao and co-workers assembled arrays of aligned single crystal C_{60} nanoribbon and nanoneedle on the silicon wafer through a simple droplet-pinned crystallization (DPC) method. FETs based on these C_{60} nanocrystals exhibited exceptional electron mobility of 11 $cm^2V^{-1}s^{-1}$.[16]

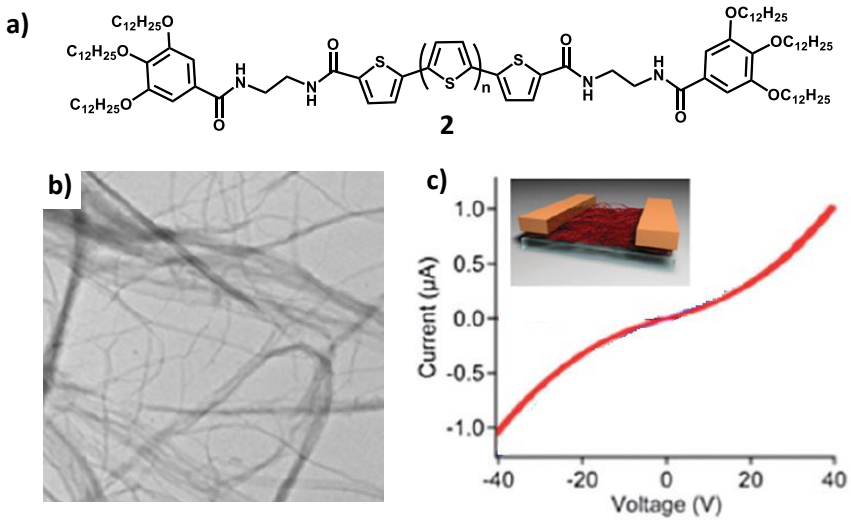

Figure 1.3. a) Molecular structure of **2**, b) TEM image of the bundled nanofiber networks and c) I–V curves of the device (Inset: Schematic of the device).

Blending of supramolecular nanostructures with appropriate dopant can modify the inherent electrical properties. Self-assembled tetrathiafulvalene (TTF) derivatives (**3** and **4**) exhibited a mixed-valence state upon doping with iodine, and showed high electrical conductivity (Figure 1.4).[17,18] Hydrogen bonding driven self-assembly of **4** shows lower oxidation potentials due to the stabilization effect arising from the strong

π-π interaction between the aromatic units. Stupp et al. have studied the influence of self-assembly on the electronic properties of dendron rodcoil molecule containing oligo(thiophene) units.[19] Iodine-doped films cast from the self-assembled gel showed conductivities of 7.9×10^{-5} Scm^{-1}, whereas films cast from tetrahydrofuran (THF) exhibited conductivities that are lower by 3 orders of magnitude (8.0×10^{-8} Scm^{-1}). This property can be ascribed to the improved π-orbital overlap along the conductive pathways in the ribbon-like nanostructures, which was absent in the THF solution.

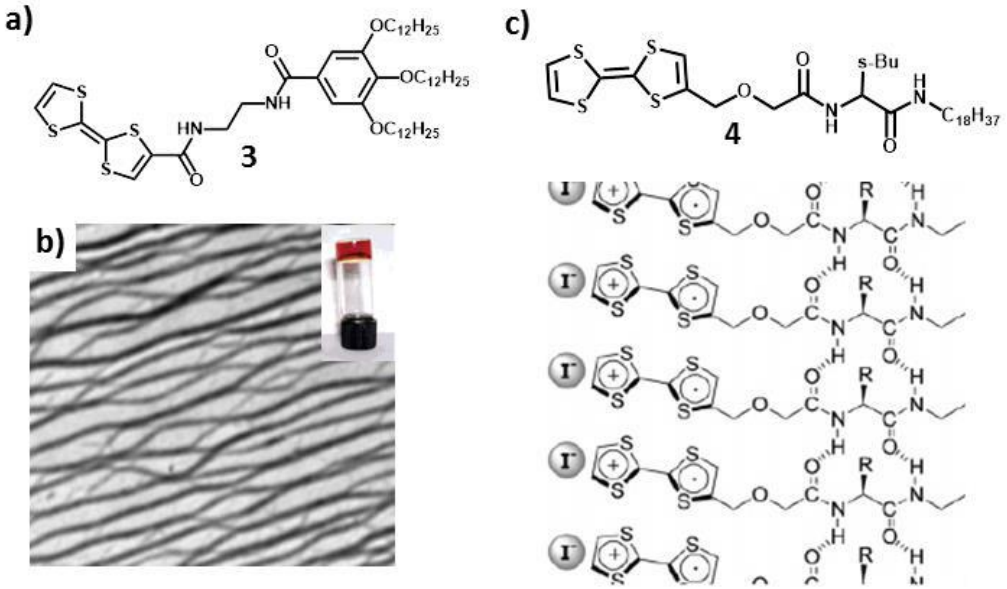

Figure 1.4. a) Chemical structure of **3** and b) TEM images of the hexane gel fibers of **3** (Inset: photograph of hexane gel). c) Chemical structure of **4** and schematic illustration of aggregates of hydrogen bonded TTF derivatives doped with iodine.

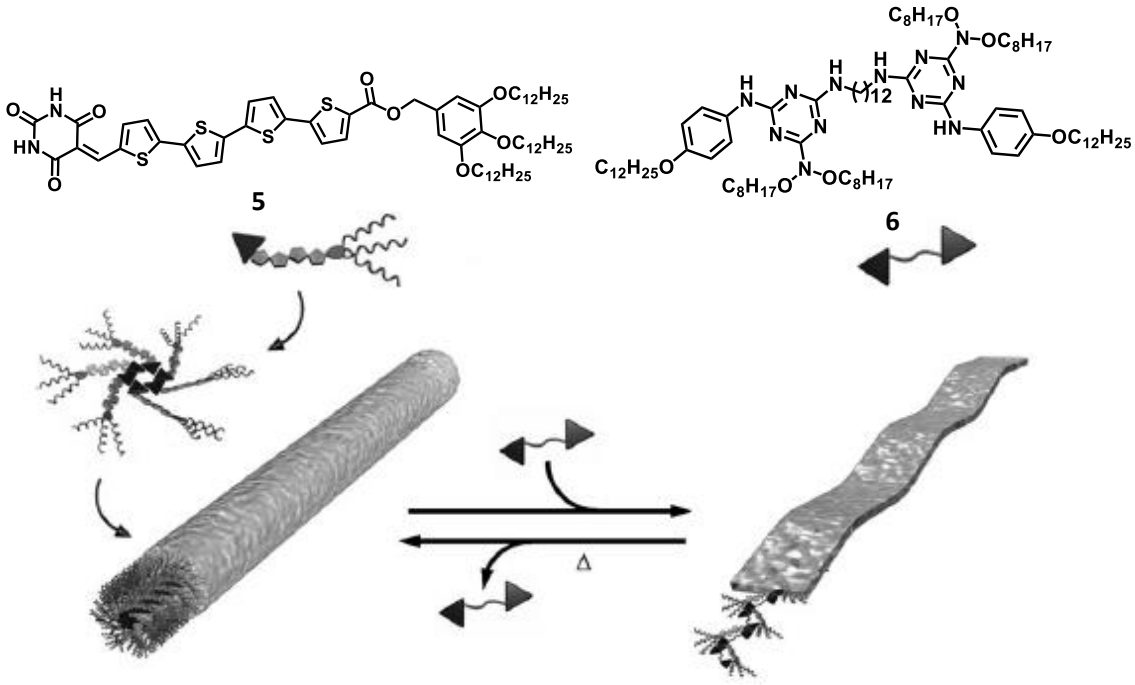

Figure 1.5. Chemical structure of molecules and schematic representation of interconversion between nanorod and nanotape.

Molecular packing has a crucial role in deciding the charge carrier transport mechanism of supramolecular systems. Yagai et al. have demonstrated co-aggregation of oligothiophene derivative (**5**) with a bismelamine receptor (**6**) using complementary hydrogen bonding interaction.[20] Mixed assembly of **5** and **6** leads to the formation of interconvertible nanorods and nanotapes with high charge carrier mobility of 1.3 $cm^2V^{-1}s^{-1}$ and 0.57 $cm^2V^{-1}s^{-1}$, respectively (Figure 1.5). High charge carrier mobility of nanorods is accomplished due to the charge carrier transport along with the long axis of 1D assembly, whereas the interchain transportation of charge carriers within the lamella plays a dominant role for the conductivity of nanotapes.

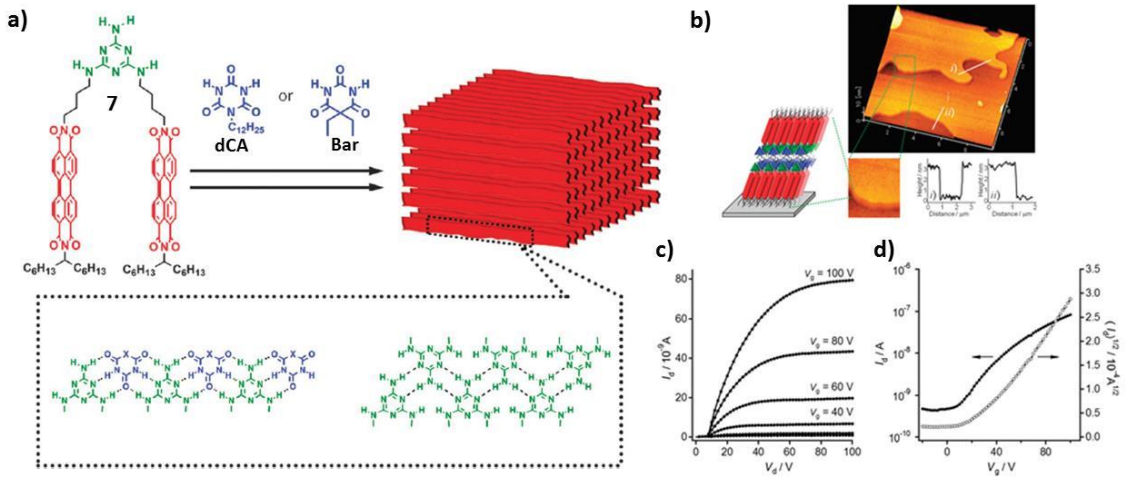

Figure 1.6. a) Chemical structure of **7** and schematic representation of self-assemblies of **7** and its co-assembly with **dCA** or **Bar** into lamellar structures. b) AFM image of annealed thin film of **7.Bar** with cross sectional analysis along white lines in image. c) Output and d) transfer characteristics of the OFET device of **7.Bar**.

Complementary hydrogen-bonding interactions can be used for the controlled organization of rigid π-conjugated systems into lamellar structures through the formation of tapes.[21] Lamellar supramolecular architectures can act as electron transporting layers in organic field effect transistors (OFET) devices. Melamine bearing perylene bisimide (PBI) derivative (**7**) makes complementary hydrogen-bonding with barbiturate units leading to the formation of linear tape like hydrogen-bonded strands which can act as efficient charge transport channel (Figure 1.6).

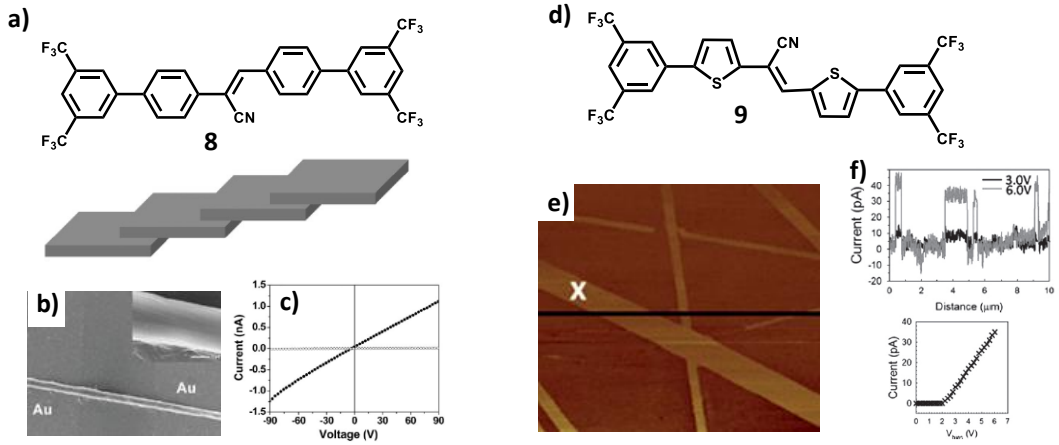

Figure 1.7. a) Chemical structure of **8** and schematic representation of its *J*-type aggregation. b) SEM image of a single patterned wire across a pair of gold electrodes and c) I-V characteristics of devices composed of a patterned single wire of **8**. d) Molecular structure of **9**, e) AFM topographic image of nanowires and f) current profiles obtained from the solid lines and point current versus V_{bias} at a fixed position on the NWs.

Noncovalent forces such as π-π stacking and the electrostatic attraction are crucial factors in creating functional crystalline nanostructures from π-conjugated rigid aromatic systems. 1-Cyano-trans-1,2-bis-(3′,5′-bis-trifluoromethyl-biphenyl) ethylene (**8**) exhibited a spontaneous flow induced 1D assembly due to the strong π-π interactions of the planar and conjugated aromatic segments.[22] Dipolar interactions due to -CF_3 and -CN groups also affect the fibrillar growth of the directional molecular self-assembly (Figure 1.7). The devices fabricated using microwire of **8** exhibited an average electrical conductivity of 4.9×10^{-6} Scm^{-1}. Organic semiconductors offer chemical structure variety as well as the property tunability, which make them potential candidates for molecular electronics. It is observed that when phenyl group in **8** is replaced by thiophene unit, band gap energy of the π-

conjugated system (**9**) gets lowered with prominent improvement in the charge carrier mobility.[23] Polar and bulky cyano groups induce molecular planarization and *J*-type molecular stacking to facilitate the formation of crystalline one dimensional nanowires (1D NW). Enhanced π-π stacking and continuous head-to-tail molecular arrangements along the 1D NW promote effective charge carrier mobility up to 3.1 $cm^2V^{-1}s^{-1}$ (Figure 1.7).

The control over the aromatic stacking is a crucial factor in deciding the crystallinity of 1D nanostructures. Zang et al. have showed the formation of ultra-long 1D self-assembled nanobelts from asymmetric perylene tetracarboxylic diimide.[24] Slow crystallization process facilitate organized molecular stacking and extended growth along the fibrillar long axis, which is dominated by the long range π-π interaction between the perylene tetracarboxylic diimide scaffolds. The effective intermolecular π-electron delocalization enables efficient long-range charge migration by the external charge doping. Rigid planar π-conjugated systems are remarkable candidates for FET applications, which can be ascribed to the dense molecular packing with strong intermolecular interactions along the charge injection layer as well as along the charge carrier transport direction.[25] Würthner et al. have fabricated single crystal field effect transistors from electron deficient 2,6-dichloro-1,4,5,8-naphthalene tetracarboxylic diimide having *n*-channel mobility of up to 8.6 $cm^2V^{-1}s^{-1}$ with the threshold voltage of about 9 V and $I_{on/off} \sim 7 \times 10^7$.

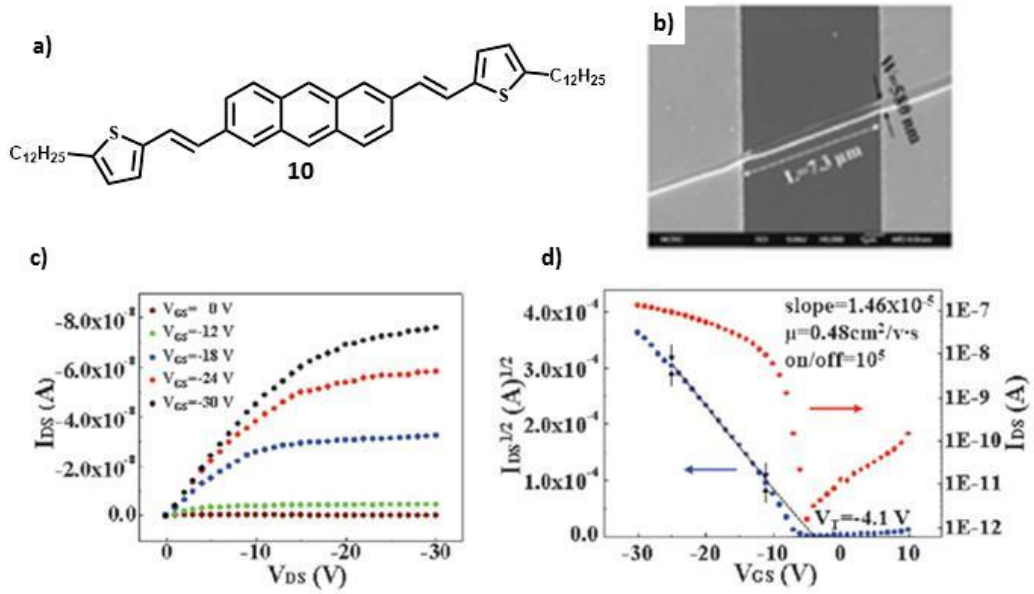

Figure 1.8. a) Molecular structure of **10** and b) SEM image of the bottom-contact single-nanofiber transistor of **10**. c) Output and d) transfer characteristics of a single-nanofiber transistor.

Ordered molecular packing of π-conjugated systems is fundamental requirement for organic field effect transistor application. Lee et al. have constructed organic single-nanofiber transistors from dodecyl-substituted thienylvinyl anthracene (**10**) having hole mobility of 0.48 $cm^2V^{-1}s^{-1}$ with $I_{on/off}$ ratio of 10^5 (Figure 1.8).[26] Highly crystalline single-nanofiber transistor exhibited much higher field effect mobility than a thin film transistor. This is attributed to the strong π-π stacking interactions between the π-backbones and van der Waals interactions between the long alkyl chains. The self-assembly of oligothiophenes into one-dimensional nanostructures can be used as potential candidate for organic electronic applications.

Organic semiconductors having face-to-face molecular packing in the solid state are of particular interest for its high performance in OFETs. Jen et.al have used S•••S interactions and electrostatic interactions in benzothiadiazole-tetrathiafulvalene to obtain single crystal nanowire.[27] FET devices constructed from 1D single-crystal nanowire showed hole mobilities of 0.36 $cm^2V^{-1}s^{-1}$ with $I_{on/off}$ ratio of 1×10^6.

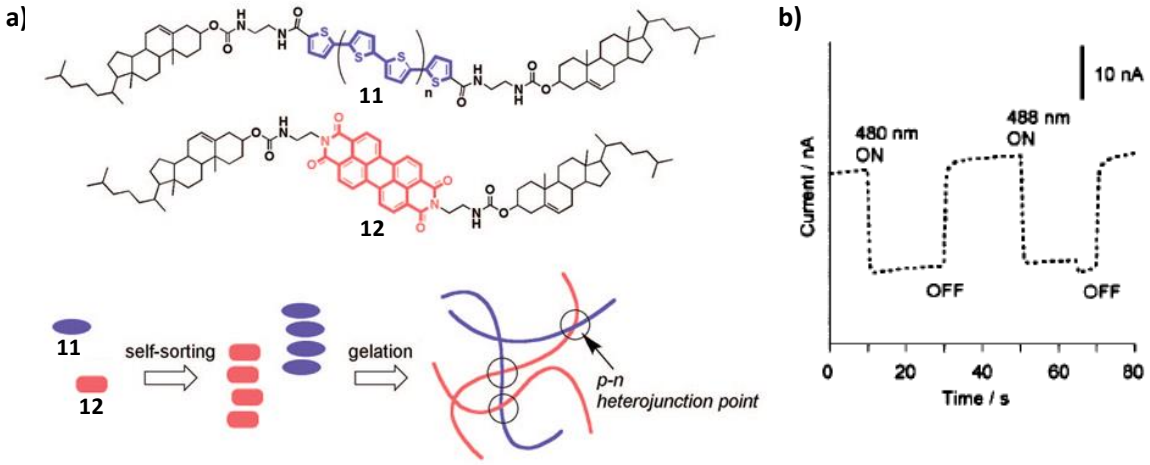

Figure 1.9. a) Chemical Structures of **11** and **12** and schematic representation of self-sorted organogel formation yielding *p-n* heterojunction points. b) Photoelectrochemical response of cast film prepared from self-sorted gel on an ITO electrode (Applied potential :0.2 V vs Ag/AgCl).

Self-sorted assembly of *p*-type and *n*-type gelators facilitates efficient dissociation of photogenerated excitons and produces continuous carrier pathways. For instance, cholesterol appended thiophene and PBI derivatives (**11** and **12**) make self-sorted gel fibers, entangled each other to form *p-n* heterojunction points (Figure 1.9).[28] Photovoltaic devices constructed from hairpin-shaped sexithiophene molecule (**13**) have better efficiency compared to that of linear sexithiophene derivative (Figure 1.10).[29] The molecule **13** self-assembles to form electron donating nanowires which in presence of PCBM creates continuous percolating pathways for the charge

transport. Thermal annealing enhances the power conversion efficiency by promoting domain growth while maintaining network of self-assembled nanowires and fullerene acceptors. Linear derivative does not form 1D structures and thermal annealing lowers the device efficiency due to the excessive phase separation along with the formation of defects. Aggregation behavior of grooved nanowires facilitates interaction with fullerenes in receptor ligand type configurations at the heterojunction of the two domains, thus enhancing device efficiencies by 23%.

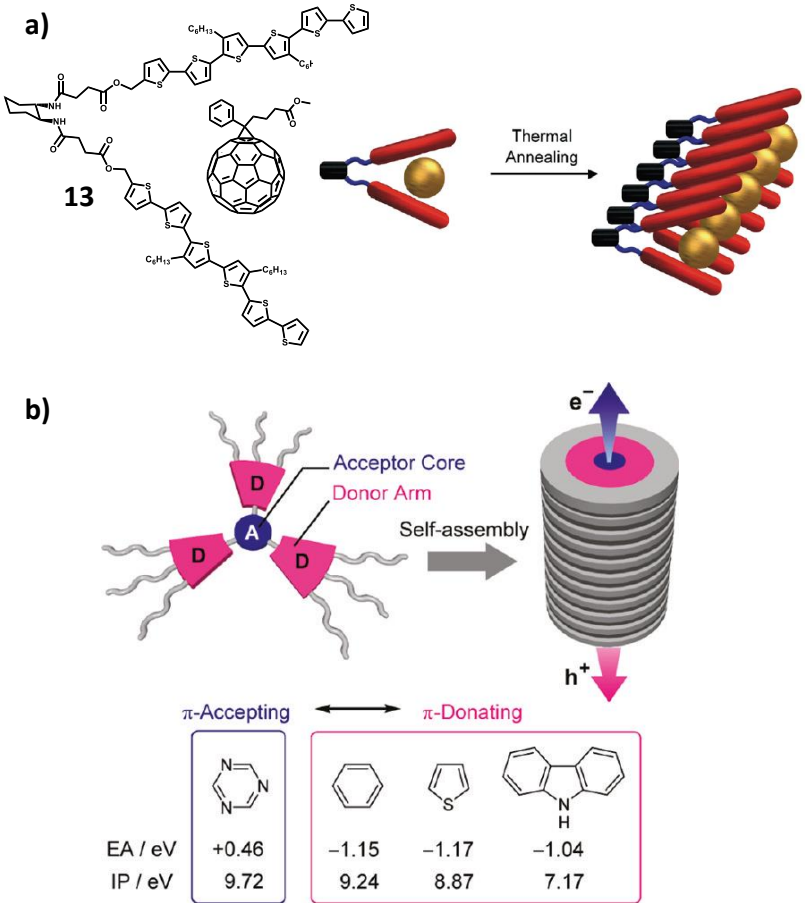

Figure 1.10. a) Nanostructural organization of **13** and PCBM molecules. b) Design of octupolar *π*-conjugated molecule and its self-assembled nanosegregated structure for ambipolar conductive columnar materials.

Columnar nanostructures with extended π-stacks can provide efficient 1D percolation pathways for mobile charge carriers. Kato et al. have fused liquid-crystalline octupolar π-conjugated structures with three electron-donating segments symmetrically attached to an electron-accepting triazine core to have ambipolar charge-transporting property.[30] Electron donor and acceptor segments are assembled individually in each column to facilitate both hole and electron transport (Figure 1.10).

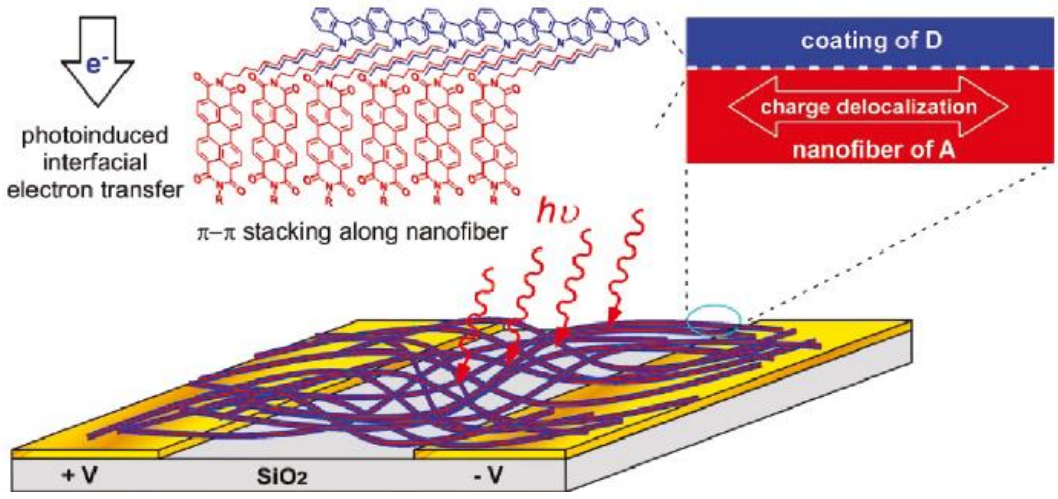

Figure 1.11. Nanofibril heterojunctions composed of electron donor (D)-coated on electron acceptor (A) nanofibers.

Zang et al. have achieved highly photoconductive materials by the interfacial engineering of D-A nanofibril heterojunction.[31] Hydrophobic interaction between long alkyl side-chains has a crucial role in the efficient photocurrent generation. The employed alkyl groups assist effective surface coating of acceptor nanofibers with donor molecules for effective electron-transfer process (Figure 1.11). Alkyl chains also play a key role in preventing charge carrier recombination by spatially separating

them. Photoconductive 1D nanomaterials have potential application in vapor sensing of various oxidizing analytes. Zang et al. have fabricated ultrathin nanoribbons from donor/acceptor (D/A) units comprising perylene as rigid π-backbone.[32] The optimal kinetic balance between the intramolecular charge recombination and the intermolecular one-dimensional charge carrier transport, make these nanoribbons as efficient vapor sensors for nitro-based explosives.

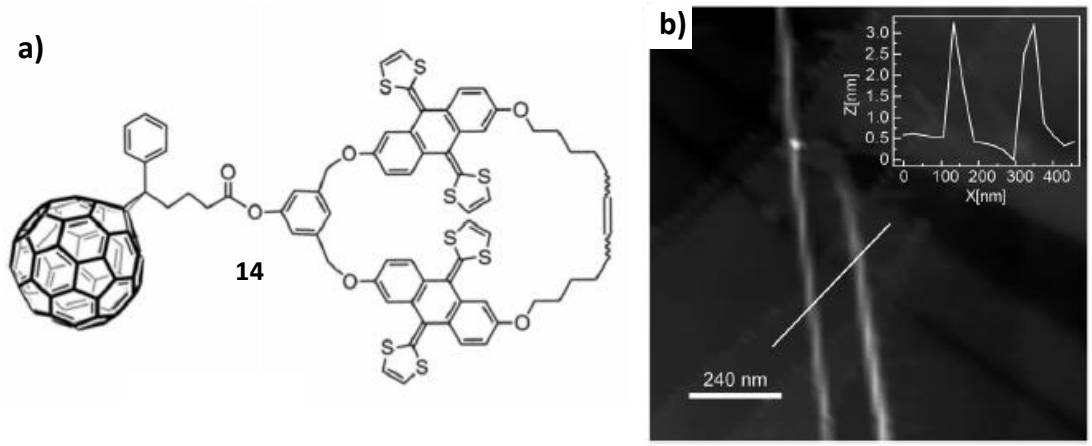

Figure 1.12. a) Chemical structure of **14** and b) AFM images of long straight fibers.

Martin et al. have demonstrated organized donor-acceptor array using π-π stacking as main driving force. Concave aromatic surface of the π-extended tetrathiafulvalene analogue (exTTF) units serves as efficient recognizing motif for the convex surface of C_{60} units. Unlike the usual supramolecular polymers based on dispersion forces, linear supramolecular polymers from two complementary units, a C_{60} derivative and an exTTF-based macrocycle (**14**) showed a remarkable degree of polymerization (Figure 1.12).[33] By introducing preorganization in the exTTF host part of the monomer, high molecular weight (MW > 150 kDa) was obtained in

solution and up to 90 kDa was attained in gas phase, which is the highest degree of polymerization for fullerene-based supramolecular polymer reported to date.

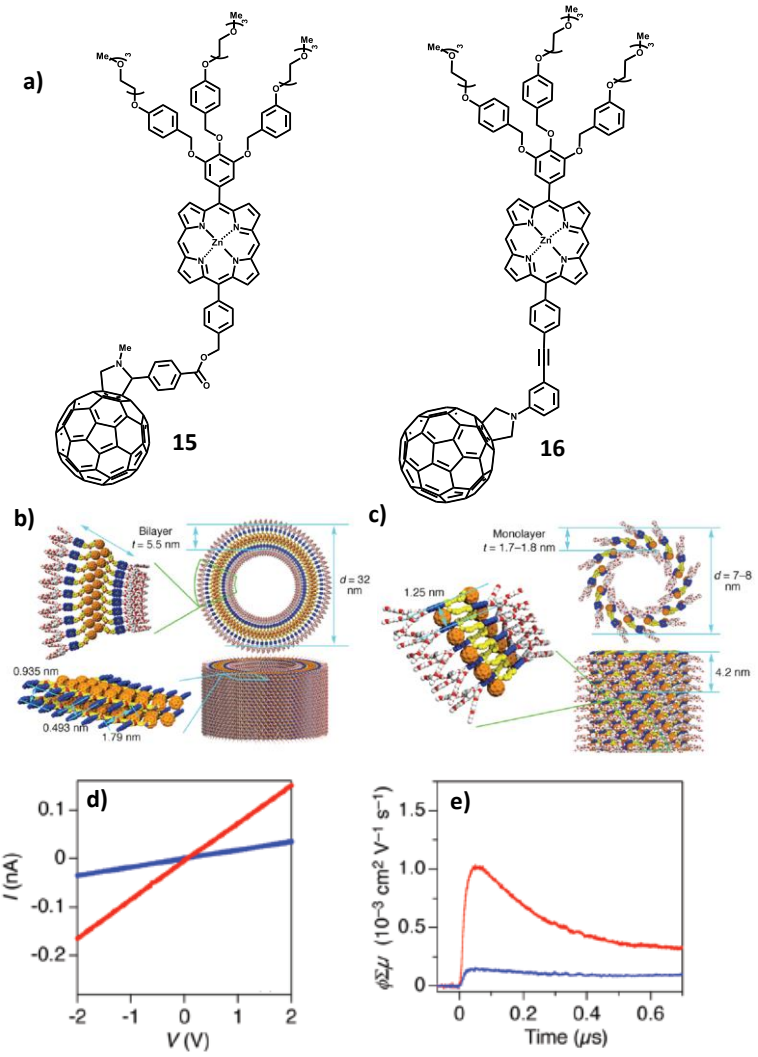

Figure 1.13. a) Molecular structures of dyads. Schematic representations of tubularly assembled b) **15** and c) **16.** d) I−V profiles at 25 °C of cast films of nanotubularly assembled **15** (red) and **16** (blue). e) TRMC profiles at 25 °C of cast films with tubular assembly of **15** (red) and **16** (blue) upon irradiation by a pulsed laser at 355 nm.

Tailoring of D-A heterojunctions is crucial in designing optoelectronic materials with efficient photon-energy conversion. Zinc porphyrin-C_{60} dyad with dissimilar

linkers self-assemble to form nanotubes with different dimensional and geometrical features.[34] Dyad with ester linkage (**15**) form nanotube with bilayer having coaxially segregated D and A nanodomains along the tube axis, whereas dyad with rigid arylacetylene linker (**16**) forms nanotube with monolayer wall having an alternate geometry of D/A stacking. Tubular morphology with segregated D/A domains showed better photoconducting properties than that having alternate D/A stacking geometry (Figure 1.13).

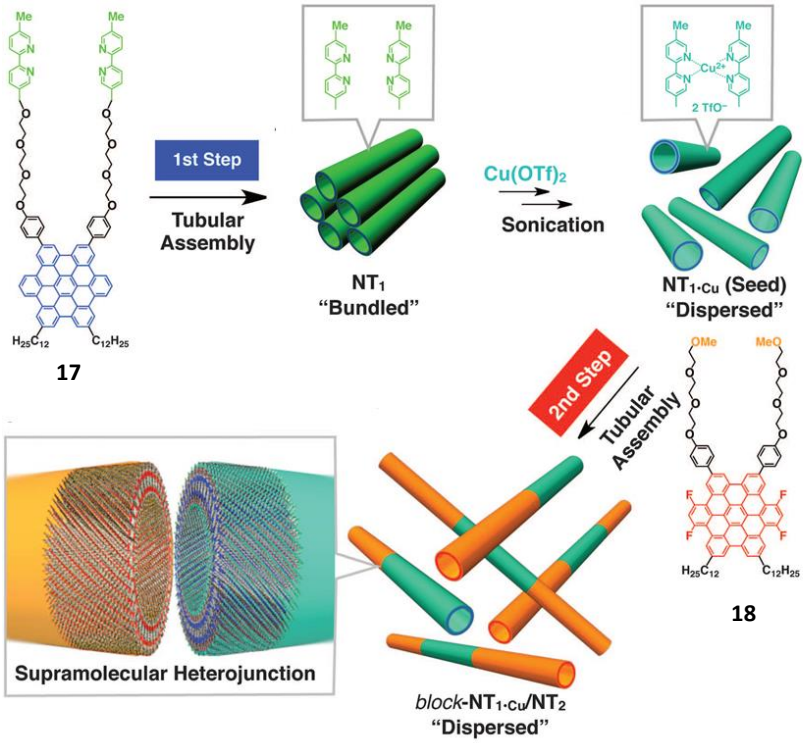

Figure 1.14. Schematic illustrations of linear heterojunction from semiconducting nanotubular segments.

Extensive π-orbital overlap and ordered columnar structures in organic semiconductor ensure effective charge carrier transport along the supramolecular stacks. Hexabenzocoronenes (HBC) is one of such successful organic semiconductor

systems for organic field-effect transistors and photovoltaic devices. Supramolecular nanotubes having complementary semiconducting properties were constructed from HBC derivatives (**17** and **18**). By non-covalently connecting these homotopically assembled nanotubes, Aida et al. have created one-dimensional nanoscale heterojunction (Figure 1.14).[35] This was due to stronger heterotopic π-stacking when compared to homotropic molecular stacking. The formed heterojunction interface showed characteristic excitation energy transfer and charge transfer properties which are not present in the homotropic nanotubes.

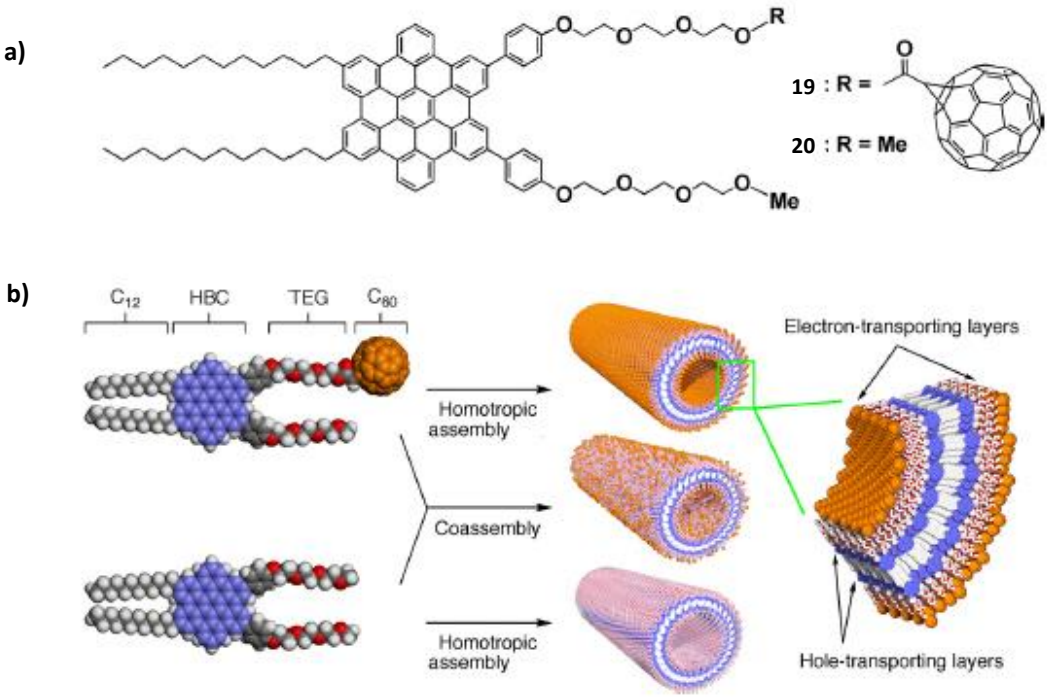

Figure 1.15. a) Molecular structures of **19** and **20**. b) Schematic representation of the formation of homotropic and co-assembled nanotubes of **19** and **20**.

Charge carrier property of supramolecular nanotubes depends on its molecular packing composition. Co-assembly of Gemini shaped HBC derivatives (**19** and **20**) form coaxial nanotube, whose wall consists of graphite-like π-stacked HBC layer

laminated on its both sides by a molecular layer of C_{60} units.[36] Intertubular carrier mobility was comparable to intersheet mobility in graphite and the amphipolar character was shown by these nanotubes in FET device output. π-Stacked HBC array acts as hole conducting layer, whereas a cluster of C_{60} provides pathway for electron-transport along the nanotube (Figure 1.15).

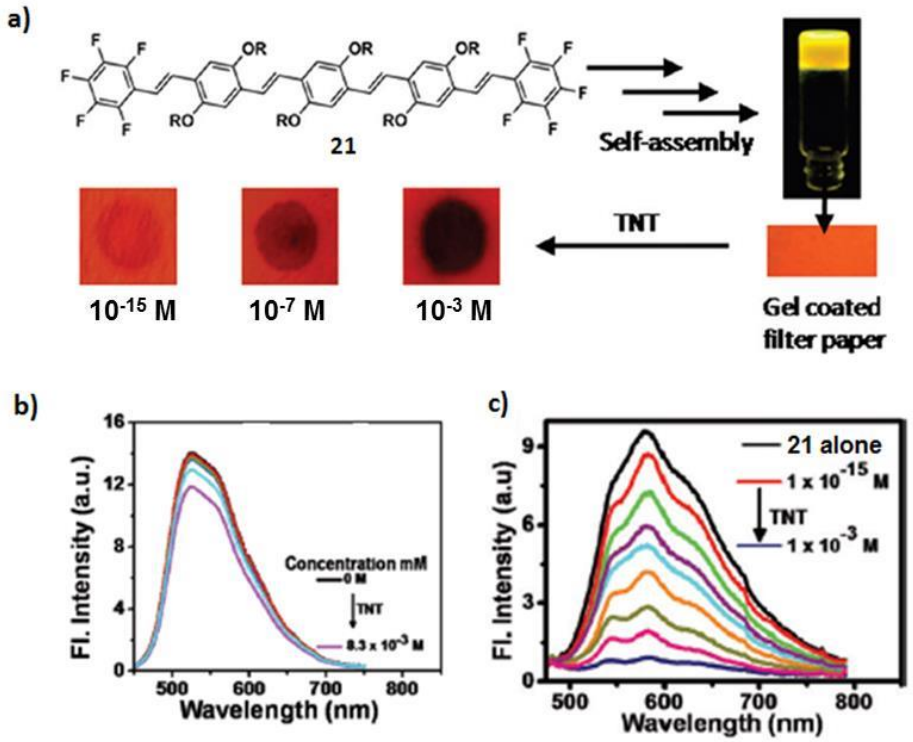

Figure 1.16. a) Molecular structure of gelator (**21**) and its detection of TNT on surfaces. b) Emission spectra of **21** in chloroform upon addition of different amounts of TNT. c) Emission spectral change of the test strips with different concentration of TNT.

In most of the π-conjugated chromophores, self-assembly and gelation significantly affect the emission color and intensity, which make them as useful candidates for the detection of various analytes. Ajayaghosh et al. have shown attogram sensing of TNT by oligo(*p*-phenylenevinylene) (OPV)-based gelator (**21**) in the self-assembled xerogel state (Figure 1.16). TNT sensing was less efficient in the

solution state. High sensitivity self-assembled xerogel is due to the faster exciton diffusion mechanism occurring inside the gel fibers.[37]

Supramolecular gel matrix can be used as an active medium for fluorescence resonance energy transfer (FRET) process.[38] FRET occurs from the self-assembled nanostructures rather than from the individual molecule and so the efficiency of FRET to the physically attached acceptor units within nanostructures depends on the aggregating ability of the π-conjugated systems. Hence energy transfer process in the supramolecular nanostructures depends on many factors such as functional groups, temperature and solvent.

1.4.2. Effect of Supramolecular Interactions on Functional Properties of π-Conjugated Polymers

Due to its excellent optoelectronic properties as well as good thermal and chemical stability, π-conjugated polymers have wide ranging applications as conducting polymers, light-emitting diodes, field-effect transistors and as solar cells. High performing donor-acceptor conjugated polymers possess low exciton binding energy and ultrafast intramolecular charge transfer, which are potential requirements for advanced photovoltaic applications. Molecular structure, frontier orbital energy levels and morphological characteristics in mesoscopic to macroscopic scales are crucial factors which significantly influence the optoelectronic properties of these π-conjugated systems. [39-43]

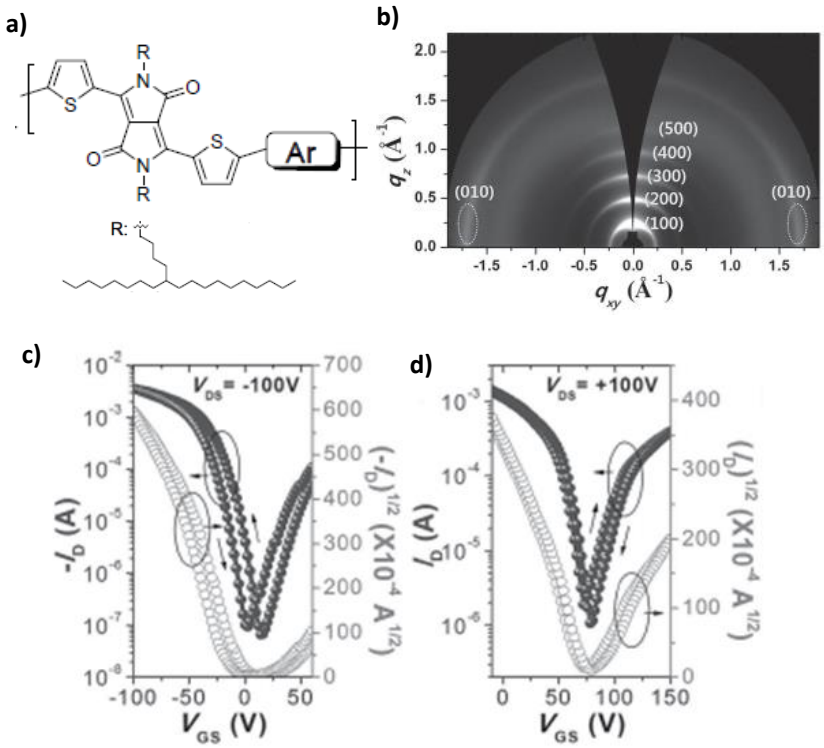

Figure 1.17. a) Representative structures of DPP-based polymers bearing branched side chains. b) 2D-GIXD images of annealed polymer films. Transfer characteristics at c) hole and d) electron-enhancement operation with V_{DS} = −100 and +100 V, respectively.

Side chain engineering is a successful approach to tune molecular packing and charge carrier transport in π-conjugated polymers.[42-46] Oh et al. have demonstrated structure-property relationship by modulating the side-chain branching position (Figure 1.17).[47] Strong π-π stacking and the lamellar molecular packing associated with the side chain modification significantly improve charge-transport properties and hence FET performance. Fibrillar structures with edge-on molecular orientation provide dominant 3D conduction pathway for efficient charge transport. FET devices fabricated using the ambipolar polymers showed excellent electron mobilities (up to 2.25 $cm^2V^{-1}s^{-1}$), ultra-high hole mobilities (up to 12.25 $cm^2V^{-1}s^{-1}$) with $I_{on/off}$ of 10^6. Even though inherently insulating, longer side alkyl chains enable the formation of

electron-percolation pathways in BHJ solar cell by facilitating proper donor-acceptor phase separation.[48] This morphological feature ensures efficient and balanced electron/hole mobilities with higher fill factor.

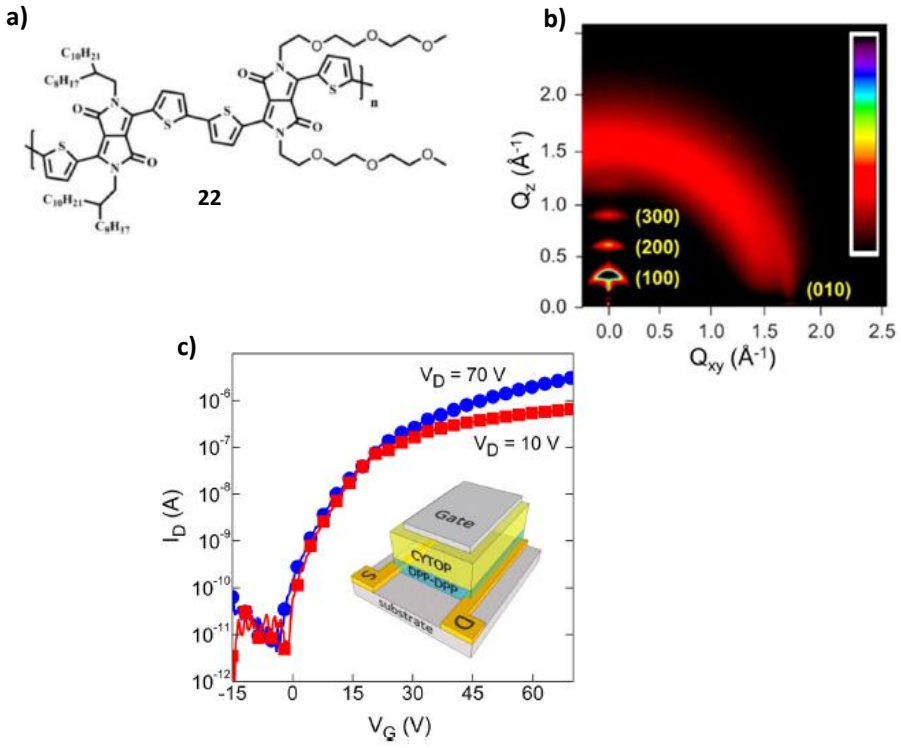

Figure 1.18. a) Chemical structure of the polymer **22**. b) GIXRD pattern for the as-spun thin film, exhibiting four orders of lamellar Bragg sheets. c) Transfer characteristics of the top-gate-bottom-contact (TG-BC) transistors (Inset shows a schematic of the TG-BC transistor architecture used).

Diketopyrrolopyrrole (**DPP**) based conjugated polymers are well studied semiconducting polymers due to strong donor-acceptor interaction which promote self-assembly of the polymer chain. Optimization of the chain packing and formation of large crystalline domains can be further tuned by side chain engineering.[49] Functionalization with triethylene glycol (TEG) side chains induces spontaneous

chain crystallization due to hydrophilic-hydrophobic interaction with concomitant strong π-π stacking interactions. Bottom-gate-bottom-contact (BG-BC) transistors fabricated from diketopyrrolopyrrole (**22**) based conjugated copolymers showed electron mobility about 3 $cm^2V^{-1}s^{-1}$ (Figure 1.18).

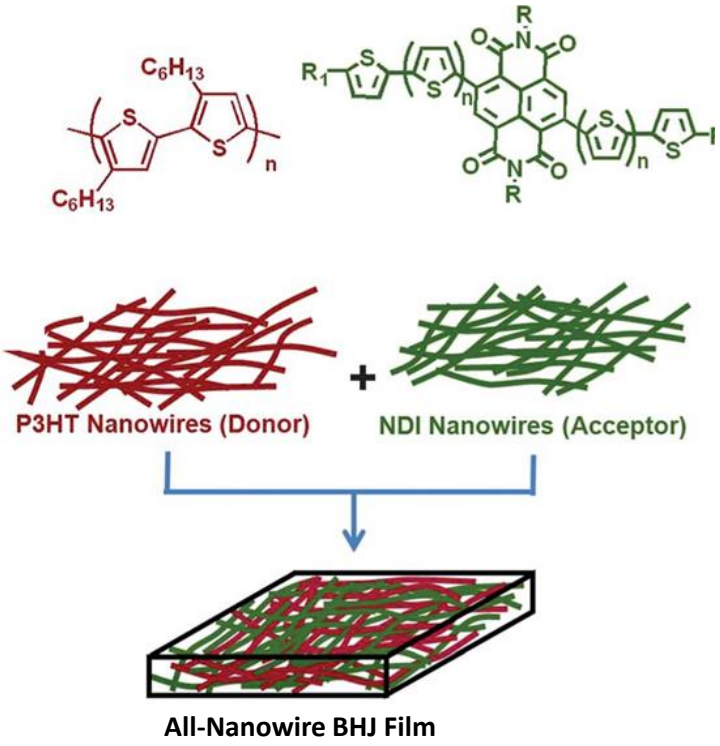

Figure 1.19. Schematic of all-nanowire bulk heterojunction (BHJ) film for organic photovoltaics.

Generally, long-range order and close π-π packing improve semiconducting properties of π-conjugated systems. Small π-π spacing is preferable for efficient charge transport mechanism in polymer since it reduces the energy barrier for interchain charge hopping. Aromatic stacking with an in-plane fashion with respect to the substrate is an essential requirement for efficient charge carrier transport in OFETs.[50] Because of the lower tendency for aggregation, highly soluble polymers

interact spontaneously with the substrates and, thereby forming kinetically favorable molecular packing with out-of-plane π-stacking. Induced aggregation caused by the addition of non-solvent results in films with ordered nanostructures with predominant in-plane π-π orientation and high field-effect hole mobility.

Optimization of device fabrication has a crucial role in deciding active layer morphology and hence photovoltaic properties. Yang et al. have demonstrated the role of solvent composition on polymer chain arrangements which can be explained in terms of conformational changes in polymer chain and functional group interactions with the solvent composition.[51] Nanoscale morphology of donor-acceptor phases in the active layer has key role in the performance of BHJ solar cell. Jenekhe et al. have constructed efficient BHJ solar cell using nanowires of P3HT and naphthalene diimides derivative as donor and acceptor components respectively (Figure 1.19).[52] All-nanowire bulk heterojunction from *p*-type and *n*-type organic semiconductors has advantages of large interfacial surface area with improved crystallinity, which facilitate efficient separation, transport and collection of charge carriers.

Relative molecular orientation in the donor/acceptor heterojunction is an important parameter in realizing high-performance bulk heterojunction solar cells. Donor/acceptor interfaces can preferentially adopt face-on or edge-on orientations in BHJ devices and is a critical parameter for efficient device output. Ade et al. have demonstrated superiority of face-on molecular packing over the edge-on packing due to the reduced recombination of photoexcitons during charge separation.[53] Polymers preferentially follow face-on configuration with improved short-circuit current (J_{sc})

and fill factor (FF) due to efficient exciton dissociation and improved charge carrier transport from heterojunction interfaces.

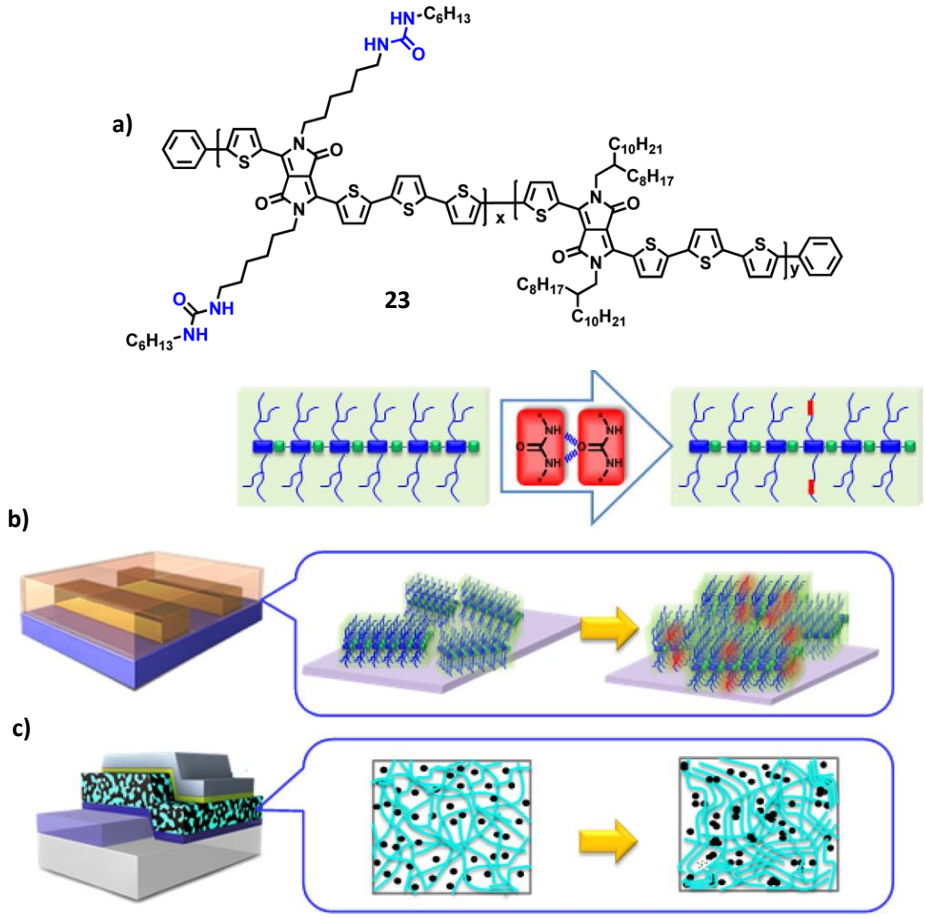

Figure 1.20. a) Chemical structure of **23** and schematic representation of the molecular assembly, b) in OFET and c) BHJ solar cell.

Li and his group demonstrated co-assembly of polyphenylenevinylene based polymer with organofullerene derivative using three-point hydrogen bonding interaction.[54] Presence of hydrogen bonding enhances intermolecular interaction and excited state interaction between the polymer and fullerene. Multiple hydrogen bonding functionalities enhance the intermolecular communication in a mixture of π-

conjugated polymer systems. Zhang et al. have achieved improved molecular packing in a D-A conjugated polymer (**23**) by side-chain engineering via hydrogen-bonding (Figure 1.20).[55] Directional hydrogen-bonding due to urea groups in the side chain, facilitates the formation of crystalline polymer domains. Alkyl chains can direct the self-organization of polymer backbones owing to the need for the side chains to form space-filling structures having low-energy. Improvement in the interchain packing order enhances the charge carrier mobility up to 13.1 $cm^2V^{-1}s^{-1}$. Fibrillar morphology of conjugated polymer facilitates ordered aggregation of $PC_{71}BM$, which enhances photovoltaic performances of polymers.

Relative strength of donor and acceptor units in the conjugated D-A polymers generally determine the nature of the charge carriers. As a matter of fact majority of the D-A semiconducting polymers are ambipolar in nature. In general, stronger donor units favor hole transport (*p*-type semiconductor), while stronger acceptor units leads to electron transport (*n*-type semiconductor). Molecular level orientation of the donor-acceptor copolymer system in the self-assembled nanostructures is important for the efficient electrical properties. Incorporation of the planar fused chalcogenophene promotes intermolecular interaction to propel self-assembly of polymer chain. Solution-processable, ambient-stable, high-performance thin-film semiconductor based on dithienylthieno[3,2-*b*]thiophene (DTT) and a comparatively weaker acceptor moiety, *N*-alkyl diketopyrrolopyrrole (DPP) is used for OFET application (Figure 1.21).[56] DTT units in the polymer chain increases the relative planarity of the polymer backbone, which promotes closer π-π stacking of polymer chains and the charge transport by hopping. OFET devices fabricated with this

polymeric semiconductor exhibited very high mobility (~10.5 $cm^2V^{-1}s^{-1}$) and $I_{on/off}$ ratio about 10^6, together with exceptional device shelf-life and operational stabilities.

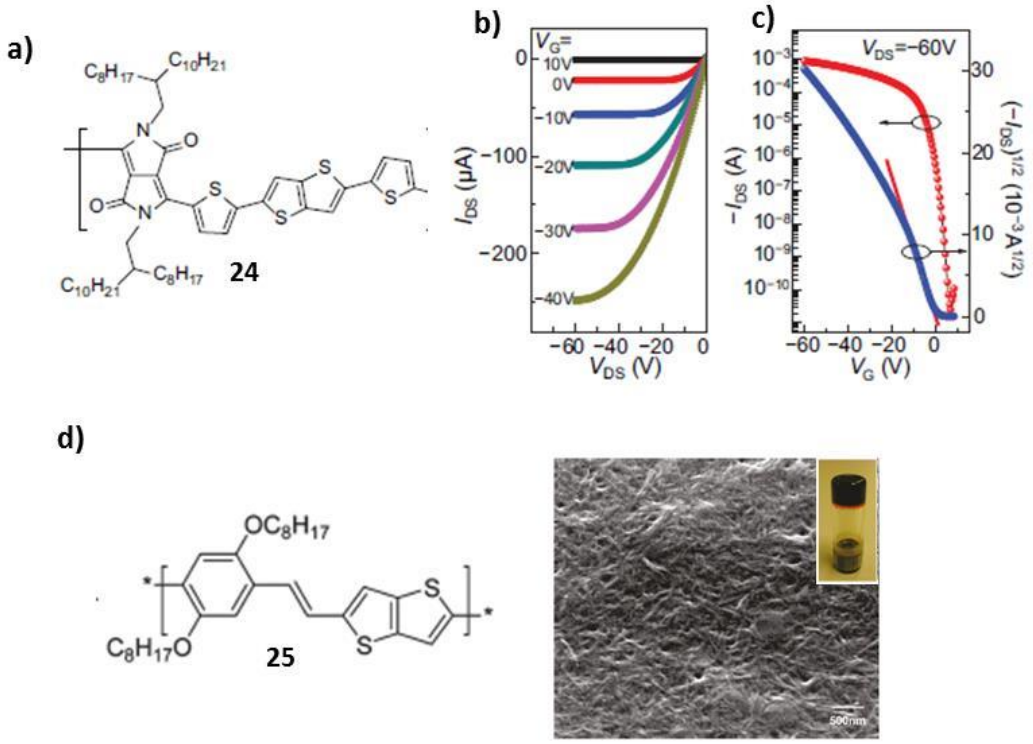

Figure 1.21. a) Chemical structure of the polymer **24**, b) output curves and c) transfer characteristics of BG-BC OFET devices. d) Structure of the polymer **25** and SEM image of the self-assembled gel fibers of **25** [inset: Gel in *o*-dichlorobenzene (*o*-DCB)].

Device performance of polymer photovoltaic cell is significantly affected by the aggregation behaviour of the polymer which in turn depends on the structure of the polymers chain. Phenylenevinylene polymer (**25**) containing thieno[3,2-*b*]-thiophene units has strong aggregation behaviour due to the *π*-*π* interaction between aromatic backbones, which results in the self-assembled gel in *o*-dichlorobenzene (Figure 1.21).[57] Photovoltaic device constructed from preassembled polymer fibers exhibited better power conversion efficiency due to the effective phase separation and reduced recombination between polymer/PCBM. Charge carrier mobility enhancement is due

to the pre-aggregates leading to better short-circuit current (J_{sc}) and the non-aggregated part prevents open-circuit voltage (V_{oc}) drop. Control over supramolecular organization of electronically active π-conjugated polymers is important to optimize their electrical properties. Janssen et al. have demonstrated the direct correlation between external quantum efficiencies (EQE) in organic solar cells and the fibrillar microstructure of active organic layer.[58] Solubility of the polymer and hence the structure of the conjugated backbone controls the dimensions of the fibrillar nanostructures. These nanofibers exhibit a tendency to form semicrystalline domains with PCBM which ensures efficient exciton dissociation and charge carrier transport over the thickness of the active layer.

Incorporation of the heteroatoms to the polymer chain is one of the useful approaches to enhance the aggregation behaviour of the polymer chains due to the introduction of strong intermolecular heteroatom-heteroatom interactions. Ashraf et al. have studied the OFET and photovoltaic performance of the DPP based copolymers with different chalcogenophene monomers (Figure 1.22).[59] Polarizability and intermolecular interaction are significantly depend on the size of the chalcogen atom. This in turn affects the crystallinity of the polymer film. These features reflect in the OFET performance and photovoltaic properties. Bulk heterojunction solar cells based on these chalcogenophene polymers could achieve power conversion efficiencies ranging from 7.1 - 8.8 % when it is blended with fullerene derivatives.

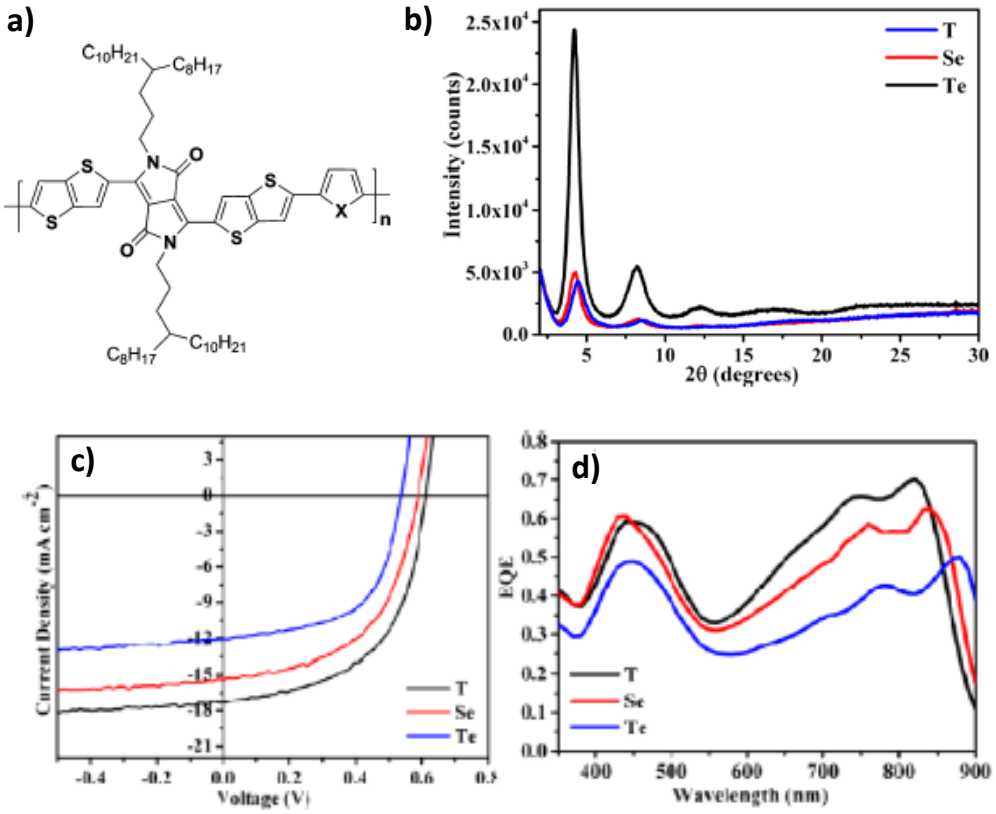

Figure 1.22. a) General structure of polymer, b) XRD diffractogram of polymers films, c) J-V curve and d) External quantum efficiency (EQE) spectra of respective Polymer/PC[60]BM BHJ solar cell (X=Thiophene for T, X=Selenophene for Se and X=Tellurium for Te).

Cho and co-workers have reported the preparation of 1D single-crystalline poly(3-hexylthiophene) (P3HT) microwires by solution crystallization process.[60] P3HT self-organize into 1D microwires via π-π interaction and this co-facial stacking in the solid state provides more efficient orbital overlap and thereby facilitating charge transport. Solution-phase assembly of π-conjugated polymers into crystalline nanostructures is highly dependent on the solubility and hence on the alkyl side chain length. Poly(3-pentylthiophene) (P3PT) self-assembled to form highly crystalline nanowires whose width is perfectly matching with the exciton diffusion length for polymer semiconductors.[61] OFET devices constructed from these nanowires showed

a *p*-type characteristics and good current modulation with $I_{on/off}$ ratio greater than 10^3. P3PT nanowires showed efficient photovoltaic performance when it is blended with $PC_{71}BM$. Jenekhe et al. have constructed crystalline nanowires (NWs) of the diblock copoly(3-alkylthiophene) with variable average aspect ratio, by the proper tuning of the composition and solution temperature.[62] Power conversion efficiency of copolymer NW/fullerene bulk hetero junction solar cell showed a correlation with the aspect ratio of the nanowires. Nanowires with high aspect ratio provide bicontinuous and percolated phase separation. Interconnected dense network increases the rate of exciton generation and dissociation, and the subsequent charge transport and collection.

Jenekhe et al. showed the correlation between overall performance of photovoltaic devices and the local nanostructure.[63] Solvent and temperature controlled self-assembly of poly(3-butylthiophene) (P3BT) leads to the formation of nanowires, which provide an efficient hole transport network and guide the crystallization of PCBM phases into electron transport network. Dense nanowires with an ordered fullerene phase are ideal for the efficient photovoltaic device. Films with a low density of nanowires result in a random bulk heterojunction composed of small crystalline PCBM and P3BT phases. Hence by optimizing the nanowire density average power conversion efficiency of 3.35 % has achieved.

Rigid and planar molecular backbone enables polymer chain to form strong intermolecular π-π interactions. Poly(benzobisimidazobenzophenanthroline) (**26**) form 1D crystalline nanobelts by controlled solution-phase self-assembly in methanol or water.[64] The polymer backbone, packs face-to-face along the nanowire direction.

These nanobelts showed air stable *n*-type semiconducting property with average mobility up to ~ 7×10^{-3} $cm^2V^{-1}s^{-1}$ and $I_{on/off}$ ratios of ~ 1×10^4 (Figure 1.23). Self-assembled single fibers from cyclopentadithiophene-benzothiadiazole copolymer showed average mobility of 5.5 $cm^2V^{-1}s^{-1}$.[65] Polymer chains are aligned along the fiber axis, which provide unhindered charge carrier pathway.

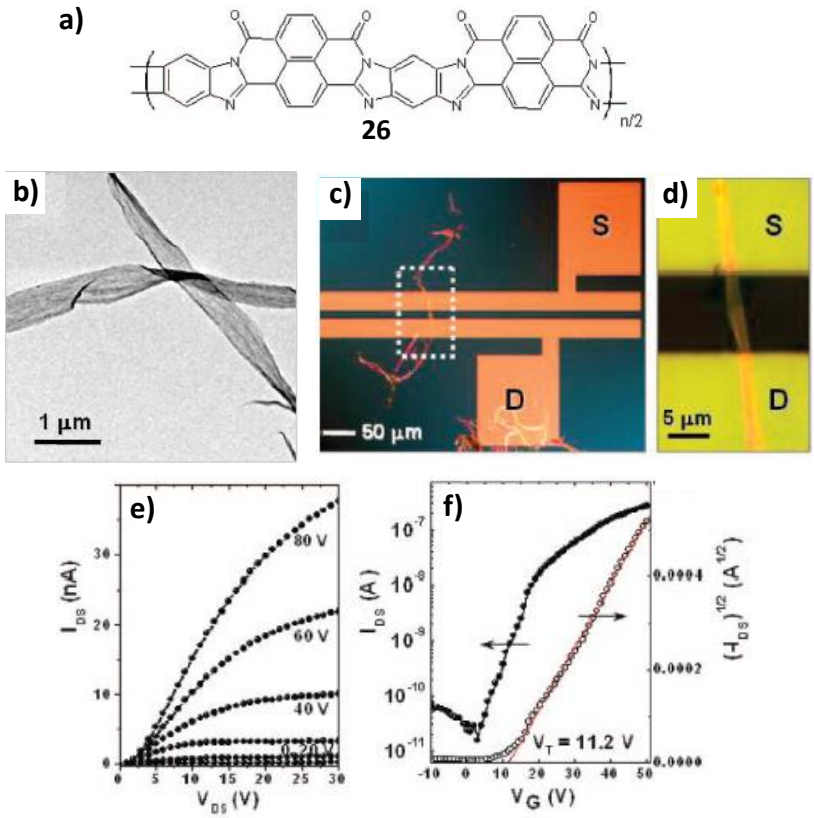

Figure 1.23. a) Molecular structure of **26**, b) TEM images of nanobelts, c) single polymer nanobelt transistor and d) close-up showing the nanobelt bridging the source-drain electrodes. e) Output and f) transfer characteristics of the transistor.

Polymer nanowire based solar cells show better performance due to better charge transport enabled by the nanowire network.[66] Preassembled polymer-semiconductor nanowires of poly(3-butylthiophene) (P3BT) serve as the donor component for fullerene acceptors. Interconnected preassembled polymer network

surrounded by a continuous PCBM phase forming bicontinuous nanoscale morphology whereas in the conventional donor-acceptor blend method spherical domains without extended interconnectivity were observed. P3BT (Nanowires):PCBM showed about 20 fold enhancement in average hole mobility and exhibited 2-fold enhancement in power conversion efficiency than conventional P3BT:PCBM blend.

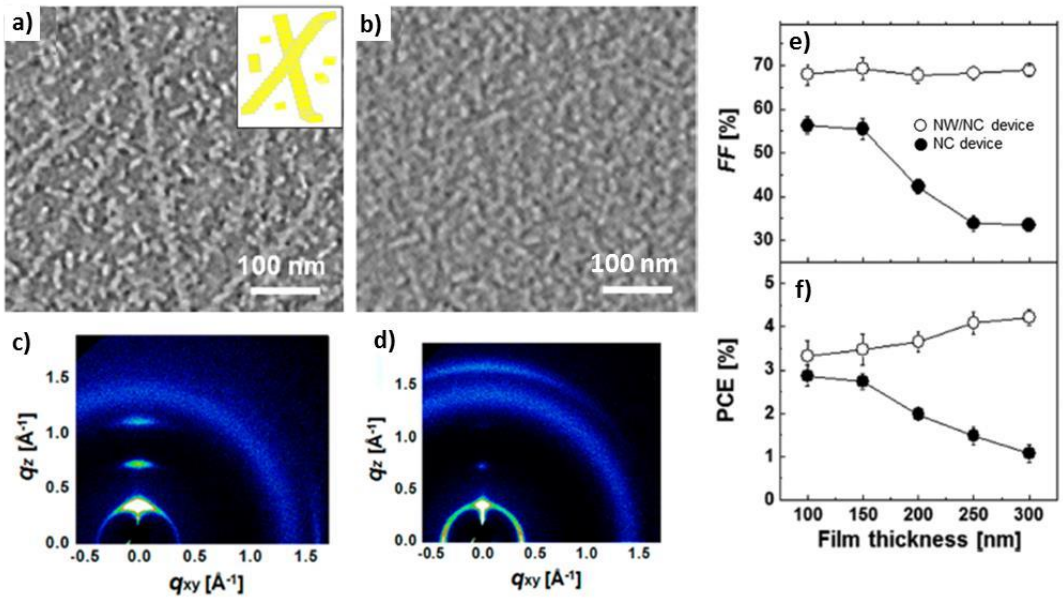

Figure 1.24. Cross-sectional images of blend layers containing a) P3HT NWs (Inset: scheme of molecular assembly) and b) P3HT NCs. 2D-GIXD patterns from the P3HT:PCBM blend films containing, c) P3HT NW/NC layer and d) P3HT NC layer. Effect of film thickness on e) fill factor (FF) and f) power conversion efficiency (PCE).

Compared to small polymer nanocrystals (NC), interpenetrating polymer nanowires (NW) significantly contribute to the charge transport properties of the photoactive layers of photovoltaic devices.[67] Interpenetrating P3HT NWs promoted charge carrier transport due to the enhanced percolation probability and the reduction in bimolecular recombination (Figure 1.24). Whereas the photoactive layer having

NC-only reduced the power conversion efficiency with increase in thickness due to its poorly developed percolation pathways. Final morphologies and hence the functional properties of the π-conjugated systems are determined by the relative strength of the molecule-molecule interactions and the molecule-substrate surface interactions.

1.5. Origin, Objectives and Approach to the Thesis

Study of supramolecular assembly of the donor-acceptor π-conjugated systems due to their potential use as active components in optoelectronic devices is an important topic of current research. The research work described in the present thesis is inspired from the recent progress in the area of functional supramolecular materials based on π-systems and their applications. In this thesis, we aim at exploring the effect of various supramolecular interactions in organizing π-systems with donor-acceptor character and study their resultant properties.

Crystalline supramolecular assembly of electron deficient π-conjugated systems such as C_{60}, perylene bisimide (PBI), etc. has significant importance due to its excellent photovoltaic applications. Molecular assembly of these systems significantly depends on the processing conditions. In order to understand the aggregation behaviour of C_{60} in a supramolecular medium, we planned to carry out the crystallization of C_{60} in a π-gel made of electron rich oligo(*p*-phenylenevinylene) (OPV). In this work, we intended to conduct detailed investigation on the morphological and electrical properties of two-component system with an objective to understand the effect of π-gel medium on the crystallization and hence on the optoelectronic properties of C_{60}.

In the assembly of the donor-acceptor system, it is quite difficult to control self-sorting and co-assembly of individual components. It is more challenging to realize a donor-acceptor system co-assembled with well-defined stacks of donor-acceptor units. In line with this objective, we thought of utilizing an electron rich OPV and an electron deficient PBI, having complementary pyridine-acid motifs. This D-A heteroassembly is expected to possess directional and ordered arrangement of the individual π-conjugated systems in the molecular level, due to the complementary hydrogen bonding. Moreover, distinct thermo-mechanical stability and nanoscopic morphology of the functional co-assembly may facilitate efficient charge carrier transport.

Molecular rigidity and planarity are essential factors for organic semiconductor to have efficient π-electron delocalization and effective charge transportation. π-Conjugated polymers are the most exploited class of organic semiconductors. Hence, in this work we designed a series of D-A π-conjugated polymers based on diketopyrrolopyrrole (DPP) and benzothieno [3,2-*b*][1]-benzothiophene (BTBT), to study the correlation between the molecular assembly and semiconducting property. We also intended to improve the rigidity of these polymers by inserting fused aromatic rings into the polymer backbone and thereby addressing the role of molecular rigidity and crystalline packing on the organic field effect transistor (OFET) performance. The present thesis delivers an in depth and systematic approach towards the afore-mentioned objectives, which are described in this thesis.

1.6. References

1. Babu, S. S., Praveen, V. K., Ajayaghosh, A. *Chem. Rev*. **2014**, *114*, 1973-2129.
2. Cheng, Y.-J., Yang, S. -H., Hsu, C. -S. *Chem. Rev*. **2009,** *109*, 5868-5923.
3. Wang, C., Dong, H., Hu, W., Liu, Y., Zhu, D. *Chem. Rev*. **2012** *112*, 2208-2267.
4. Grimsdale, A. C., Chan, K. L., Martin, R. E., Jokisz, P. G., Holmes, A. B. *Chem. Rev*. **2009**, *109*, 897-1091.
5. Allard, S., Forster, M., Souharce, B., Thiem, H., Scherf, U. *Angew. Chem. Int. Ed.* **2008**, *47*, 4070-4098.
6. Yang, L., Tan, X., Wang, Z., Zhang, X. *Chem. Rev*. **2015**, *115*, 7196-7239.
7. Hoeben, F. J. M., Jonkheijm, P., Meijer, E. W., Schenning, A. P. H. J. *Chem. Rev*., **2005**, *105*, 1491-1546.
8. Rodríguez, D. G., Schenning, A. P. H. J. *Chem. Mater*. **2011**, *23*, 310-325.
9. Schenning, A. P. H. J., Meijer, E. W. *Chem. Commun*., **2005**, 3245-3258.
10. Sathish, M., Miyazawa, K., Hill, J. P., Ariga, K. *J. Am. Chem. Soc*. **2009**, *131*, 6372-6373.
11. Geng, J., Zhou, W., Skelton, P., Yue, W., Kinloch, I. A., Windle, A. H., Johnson, B. F. G. *J. Am. Chem. Soc*. **2008**, *130*, 2527-2534.
12. Park, C., Song, H. J., Choi, H. C. *Chem. Commun*. **2009**, 4803-4805.
13. Liu, T., Li, Y., Yan, Y., Li, Y., Yu, Y., Chen, N., Chen, S., Liu, C., Zhao, Y., Liu, H. *J. Phys. Chem. C* **2012**, *116*, 14134-14138.
14. Yang, B., Xiao, J., Wong, J. I., Guo, J., Wu, Y., Ong, L., Lao, L. L., Boey, F., Zhang, H., Yang, H. Y., Zhang, Q. *J. Phys. Chem. C* **2011**, *115*, 7924-7927.

15. Stone, D. A., Tayi, A. S., Goldberger, J. E., Palmer, L. C., Stupp, S. I. *Chem. Commun*. **2011**, *47*, 5702-5704.
16. Li, H., Tee, B. C. -K., Cha, J. J., Cui, Y., Chung, J. W., Lee, S. Y., Bao, Z. *J. Am. Chem.Soc*. **2012**, *134*, 2760-2765.
17. Kitahara, T., Shirakawa, M., Kawano, S., Beginn, U., Fujita, N., Shinkai, S. *J. Am. Chem. Soc*. **2005**, *127*, 14980-14981.
18. Kitamura, T., Nakaso, S., Mizoshita, N., Tochigi, Y., Shimomura, T., Moriyama, M., Ito, K., Kato, T. *J. Am. Chem. Soc*. **2005**, *127*, 14769-14775.
19. Messmore, B. W., Hulvat, J. F., Sone, E. D., Stupp, S. I. *J. Am. Chem. Soc*. **2004**, *126*, 14452-14458.
20. Yagai, S., Kinoshita, T., Kikkawa, Y., Karatsu, T., Kitamura, A., Honsho, Y., Seki, S. *Chem. Eur. J*. **2009**, *15*, 9320-9324.
21. Seki, T., Maruya, Y., Nakayama, K., Karatsu, T., Kitamuraa, A., Yagai, S. *Chem. Commun*. **2011**, *47*, 12447-12449.
22. Kim, J. H., Jung, Y., Chung, J. W., An, B.-K., Park, S. Y. *Small* **2009**, 5,804-807.
23. Chung, J. W., Yang, H., Singh, B., Moon, H., An, B. -k., Lee, S. Y., Park, S. Y. *J. Mater. Chem*. **2009**, *19*, 5920-5925.
24. Che, Y., Datar, A., Balakrishnan, K., Zang, L. *J. Am. Chem. Soc*. **2007**, *129*, 7234-7235.
25. He, T., Stolte, M., Würthner, F. *Adv. Mater*. **2013**, *25*, 6951-6955.
26. Hong, J.-P., Um, M. -C., Nam, S. -R., Hong, J. -I., Lee, S. *Chem. Commun*. **2009**, 310-312.

27. Tucker, N. M., Briseno, A. L., Acton, O., Yip, H.-L., Ma, H., Jenekhe, S. A., Xia, Y., Jen, A. K. -Y. *ACS Appl. Mater. Interfaces* **2013**, *5*, 2320-2324.

28. Sugiyasu, K., Kawano, S., Fujita, N., Shinkai, S. *Chem. Mater*. **2008**, *20*, 2863-2865.

29. Tevis, I. D., Tsai, W.-W., Palmer, L. C., Aytun, T., Stupp, S. I. *ACS Nano* **2012**, *6*, 2032-2040.

30. Yasuda, T., Shimizu, T., Liu, F., Ungar, G., Kato, T. *J. Am. Chem. Soc*. **2011**, *133*, 13437-13444.

31. Che, Y., Huang, H., Xu, M., Zhang, C., Bunes, B. R., Yang, X., Zang, L. *J. Am. Chem. Soc*. **2011**, *133*, 1087-1091.

32. Che, Y., Yang, X., Liu, G., Yu, C., Ji, H., Zuo, J., Zhao, J., Zang, L. *J. Am. Chem. Soc*. **2010**, *132*, 5743-5750.

33. Isla, H., Perez, E. M., Martin, N. *Angew. Chem. Int. Ed*. **2014**, *53*, 5629-5633.

34. Charvet, R., Yamamoto, Y., Sasaki, T., Kim, J., Kato, K., Takata, M., Saeki, A., Seki, S., Aida, T. *J. Am. Chem. Soc*. **2012**, *134*, 2524-2527.

35. Zhang, W., Jin, W., Fukushima, T., Saeki, A., Seki, S., Aida, T. *Science*, **2011**, *334*, 340-343.

36. Yamamotoa, Y., Zhanga, G., Jin, W., Fukushima, T., Ishii, N., Saeki, A., Seki, S.,. Tagawa, S, Minari, T., Tsukagoshi, K., Aida, T. *PNAS*, **2009**, *106*, 21051-21056.

37. Kartha, K. K., Babu, S. S., Srinivasan, S., Ajayaghosh, A. *J. Am. Chem. Soc*. **2012**, *134*, 4834-4841.

38. Praveen, V. K., George, S. J., Varghese, R., Vijayakumar, C., Ajayaghosh, A. *J. Am. Chem. Soc*. **2006**, *128*, 7542-7550.

39. Jackson, N. E., Savoie, B. M., Kohlstedt, K. L., de la Cruz, M. O., Schatz, G. C., Chen, L. X., Ratner, M. A. *J. Am. Chem. Soc*.**2013**, *135*, 10475-10483.

40. Jackson, N. E., Kohlstedt, K. L., Savoie, B. M., de la Cruz, M. O., Schatz, G. C., Chen, L. X., Ratner, M. A. *J. Am. Chem. Soc*. **2015**, *137*, 6254-6262.

41. Lei, T., Wang, J.-Y., Pei, J. *Chem. Mater*. **2014**, *26*, 594-603.

42. Mei, J., Bao, Z. *Chem. Mater*. **2014**, *26*, 604-615.

43. McCulloch, I., Ashraf, R. S., Biniek, L., Bronstein, H., Combe, C., Donaghey, J. E., James, D. I., Nielsen, C. B., Schroeder, B. C., Zhang, W. M. *Acc. Chem. Res*. **2012**, *45*, 714-722.

44. Lei, T., Dou, J.-H., Pei, J. *Adv. Mater*. **2012**, *24*, 6457-6461.

45. Zhang, F., Hu, Y., Schuettfort, T., Di, C.-a., Gao, X., McNeill, C. R., Thomsen, L., Mannsfeld, S. C. B., Yuan, W., Sirringhaus, H., Zhu, D. *J. Am. Chem. Soc*. **2013**, *135*, 2338-2349.

46. Lee, J., Han, A. R., Yu, H., Shin, T. J., Yang, C., Oh, J. H. *J. Am. Chem. Soc*. **2013**, *135*, 9540-9547.

47. Han, A-. R., Dutta, G. K., Lee, J., Lee, H. R., Lee, S. M., Ahn, H., Shin, T. J., Oh, J. H., Yang, C. *Adv. Funct. Mater*. **2015**, *25*, 247-254.

48. Gadisa, A., Oosterbaan, W. D., Vandewal, K., Bolsée, J.-C., Bertho, S., D'Haen, J., Lutsen, L., Vanderzande, D. and Manca, J. V. *Adv. Funct. Mater*. **2009**, 19, 3300-3306.

49. Kanimozhi, C., Yaacobi-Gross, N., Chou, K. W., Amassian, A., Anthopoulos, T. D., Patil, S. *J. Am. Chem. Soc*. **2012**, *134*, 16532-16535.

50. Chen, M. S., Lee, O. P., Niskala, J. R., Yiu, A. T., Tassone, C. J., Schmidt, K., Beaujuge, P. M., Onishi, S. S., Toney, M. F., Zettl, A., Fréchet, J. M. J. *J. Am. Chem. Soc*. **2013**, *135*, 19229-19236.

51. Gao, J., Chen, W., Dou, L., Chen, C.-C., Chang, W.-H., Liu, Y., Li, G., Yang, Y. *Adv. Mater*. **2014**, *26*, 3142-3147.

52. Ren, G., Ahmed, E., Jenekhe, S. A. *J. Mater. Chem*. **2012**, *22*, 24373-24379.

53. Tumbleston, J. R., Collins, B. A., Yang, L., Stuart, A. C., Gann, E., Ma, W., You, W., Ade, H. *Nat. Photon.* **2014**, *8*, 385-391.

54. Fang, H., Wang, S., Xiao, S., Yang, J., Li, Y., Shi, Z., Li, H., Liu, H., Xiao, S., Zhu, D. *Chem. Mater*. **2003**, *15*, 1593-1597.

55. Yao, J., Yu, C., Liu, Z., Luo, H., Yang, Y., Zhang, G., Zhang, D. *J. Am. Chem. Soc*. **2016**, *138*, 173-185.

56. Li, J., Zhao, Y., Tan, H. S., Guo, Y., Di, C. -A., Yu, G., Liu, Y., Lin, M., Lim, S. H., Zhou, Y., Su, H., Ong, B. S. *Sci. Rep*. **2012**, *2*, 754.

57. Kim, B. -G., Jeong, E. J., Park, H. J., Bilby, D., Guo, L. J., Kim, J. *ACS Appl. Mater. Interfaces* **2011**, *3*, 674-680.

58. Li, W., Hendriks, K. H., Furlan, A., Roelofs, W. S. C., Wienk, M. M., Janssen, R. A. J. *J. Am. Chem. Soc*. **2013**, *135*, 18942-18948.

59. Ashraf, R. S., Meager, I., Nikolka, M., Kirkus, M., Planells, M., Schroeder, B. C., Holliday, S., Hurhangee, M., Nielsen, C. B., Sirringhaus, H., McCulloch, I. *J. Am. Chem. Soc*. **2015**, *137*, 1314-1321.

60. Kim, D. H., Han, J. T., Park, Y. D., Jang, Y., Cho, J. H., Hwang, M., Cho, K. *Adv. Mater*. **2006**, *18*, 719-723.

61. Wu, P.-T., Xin, H., Kim, F. S., Ren, G., Jenekhe, S. A. *Macromolecules* **2009**, *42*, 8817-8826.

62. Ren, G., Wu, P.-T., Jenekhe, S. A. *ACS Nano* **2011**, *5*, 376-384.

63. Xin, H., Reid, O. G., Ren, G., Kim, F. S., Ginger, D. S., Jenekhe, S. A. *ACS Nano* **2010**, *4*, 1861-1872.

64. Briseno, A. L., Mannsfeld, S. C. B., Shamberger, P. J., Ohuchi, F. S., Bao, Z., Jenekhe, S. A., Xia, Y. *Chem. Mater*. **2008**, *20*, 4712-4719.

65. Wang, S., Kapp, M., Liebewirth, I., Müller, M., Kirchhoff, K., Pisula, K., Müllen, K. *Adv. Mater*. **2012**, *24*, 417-420.

66. Xin, H., Kim, F. S., Jenekhe, S. A. *J. Am. Chem. Soc*. **2008**, *130*, 5424-5425.

67. Kim, J. -H., Kim, M., Jinnai, H., Shin, T. J., Kim, H., Park, J. H., Jo, S. B., Cho, K. *ACS Appl. Mater. Interfaces* **2014**, *6*, 5640-5650.

Chapter 2

Crystallization of Fullerene to Photoconducting Supramolecular Rods in an Oligo(*p*-phenylenevinylene) Based Organogel Medium

2.1. Abstract

Non-equilibrium self-assembly of molecules, hold a huge prospect as a tool to obtain new generation materials for future applications. Crystallization of neutral molecules within a supramolecular gel matrix is one such example in which two non-equilibrium processes occur orthogonal to each other. On the other hand, electronically interacting donor-acceptor two-component systems are expected to form phase miscible hybrid systems. Contrary to the expectation, we report the behavior of a π-gel, derived from oligo(p-phenylenevinylene), ***OPVA****, as a scaffold for the phase separation and crystallization of fullerene (C_{60}), to supramolecular rods with increased transient photoconductivity ($\varphi\Sigma\mu_{max}$: 2.4 × 10^{-4} $cm^2V^{-1}s^{-1}$). The C_{60} supramolecular rods in the π-gel medium exhibited high photocurrent in comparison to C_{60} loaded in a non-π-gel medium. This finding provides the opportunity to the large-scale preparation of micrometer sized photoconducting rods of fullerenes for device application.*

2.2. Introduction

Systems produced by equilibrium self-assembly represent a state of energetic minima and persist for a long time due to their thermodynamic stability. These systems are

inert towards working on their surroundings and require an external energy source to undergo a structural transformation.[1,2] On the other hand, self-assembly of molecules under non-equilibrium conditions can lead to complex architectures with fascinatingly dynamic and adaptive properties. Reversibility and directionality of the non-covalent interactions among molecular subunits can achieve high degrees of internal order that are not known in conventional polymers. The state and nature of the self-assembled nanostructures determined by the changes in lifetime of non-covalent bonds as a result of changes in the external stimuli such as temperature, pressure etc.[3,4] Even though supramolecular chemistry started with the study of systems under thermodynamic control, currently seeing a shift towards kinetically controlled and far-from-equilibrium systems, where the richest functions can be harnessed. The outcome of the latter types of molecular assembly process is dictated by the assembly pathway rather than the free energy of the final assembled state.

Both crystallization and gelation of organic molecules are known to occur under conditions that are far from equilibrium.[1,2] Specifically, gelation follows a nucleation growth mechanism driven by the kinetically controlled supersaturation gradient reasonably similar to the crystallization process.[1,5] The nucleation process leads to the formation of 1D structures with high aspect ratio which further assemble into a 3D network, better known as self-assembled fibrillar networks (SAFINs) encapsulating the solvent in which they form, resulting in gelation.[6,7] Gel phase crystallization has therefore drawn incredible attention in recent times to gain essential understanding of two simultaneously occurring orthogonal self-assembly processes.[1,8] Supramolecular gel fibers can even act as active nucleation substrates for crystallization of organic

molecules. Crystallization inside the gel medium is a well-known example of multicomponent self-assembly.[9,10] Gel assisted crystallization has been originated from the well-known work of periodic precipitation in gels known as 'Liesegang rings'. [1,11] Slow diffusion of soluble precursors such as silver nitrate to the hydrogel containing potassium chromate leads to the periodic precipitation of weakly soluble silver chromate inside the gel matrix (Figure 2.1a).

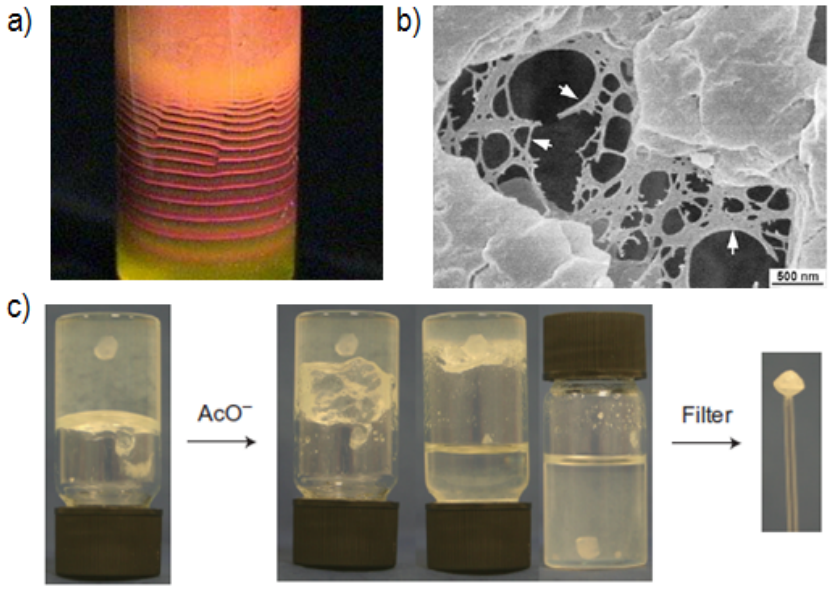

Figure 2.1. a) Liesegang rings generated from the diffusion of silver nitrate through potassium chromate in silica gel. b) FESEM images of α-glycine crystal grown inside agarose hydrogel (White arrows show incorporated gel fibers). c) Carbamazepine crystal is grown in the supramolecular gel. Recovery of the crystals by the acetate anion triggered gel dissolution.

The viscous gel medium suppresses the rate of convection current, sedimentation and nucleation which in turn improves physical characteristics of the resulting crystals. The crystals grown from the gel medium exhibit improved optical quality, larger size and fewer defects. Gel medium can act as an inert matrix within which crystal growth occurs; however, in some cases, the gel structure has proven to

influence the polymorphism, enantiomorphism and habit of crystals.[12] Gel mediated multicomponent assembly occasionally leads towards the incorporation of the gel fibers into the crystal, giving rise to composite materials. Calcium tartrate tetrahydrate and α-glycine single crystal growth has been demonstrated in agarose hydrogels, resulting in polymer/single-crystal composites (Figure 2.1b).[13]

Anion switchable supramolecular gels have been used as an effective medium for the controlled growth of pharmaceutical crystal growth (Figure 2.1c).[9] Gel phase crystallization results in different polymorphic forms of crystals when compared to the parallel solution-phase crystallization. Slow crystallization and fast supramolecular gelation ensures effective phase separation which prevent the formation of gelator-substrate co-crystal. Crystals can be recovered conveniently without any damage to the crystals by acetate ion triggered gel dissolution. Weak and flexible behavior of supramolecular assembly especially in low molecular weight gelators (LMWG) helps easy recovery of crystals from the gel matrix. Depending upon the degree of interaction between the gelator and crystallizing unit, mesoscopic compartmentalization via self-sorting or intimately mixed nanoscale phase segregated hetero-assembly may occur in these multicomponent systems.[14] In systems having a weak interaction between the two principle components, these non-equilibrium processes influence or modify the outcome of the assemblies to undergo nano to mesoscale compartmentalization without losing the identity of individual components. If such a hybrid assembly is composed of an electron donor and acceptor, it can give rise to bulk heterojunctions at varied length (nano to meso)

scales, important for efficient exciton migration towards respective electrodes in an organic optoelectronic device.[15,16]

Among various electron rich LMWGs, oligo(*p*-phenylenevinylene)s (OPVs) occupy a unique position due to their excellent optoelectronic properties.[17-19] Proper functionalization of OPV molecules results in splendid supramolecular nanostructures that can function as scaffolds for exciton diffusion and energy transfer.[18]

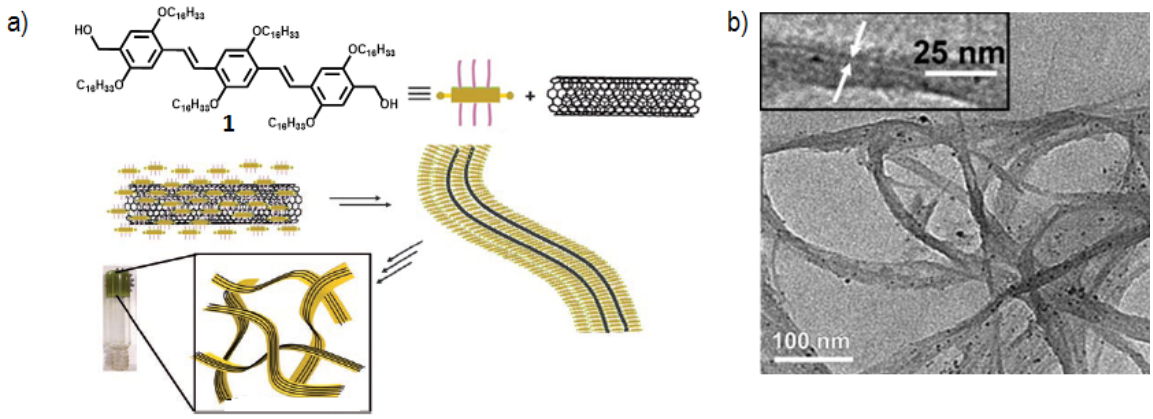

Figure 2.2. a) Chemical structures of gelator **1** and schematic representation of **1**-**CNT** composite gel formation. b) TEM image **1**-**CNT** nano composite.

Quest for new molecules and materials has also drawn considerable attention of material chemists towards interaction of electron deficient molecules such as fullerenes (C_{60}, C_{70} etc.) carbon nanotubes and graphene with OPVs.[18-22] Ajayaghosh et al. have demonstrated the molecular level physical interaction planar OPV based gelator (**1**) and carbon naotubes (CNTs) due to strong propensity for π-stacking.[23] Dispersed CNTs embedded within the gel matrix cross link the supramolecular tapes and enhance the stability of the gel (Figure 2.2). Presence of CNTs accelerate self-assembly and gelation of **1** below its critical gelation concentration. CNTs in hybrid

supramolecular assembly retain their long aspect ratio as well as their inherent electronic properties. Nanocomposites of OPV based systems and carbon nanomaterials (CNMs) show interesting electrical and thermo-mechanical properties.[24] Synergistic effect of the various supramolecular interactions in the aromatic π-conjugated gel matrix significantly changes the nanoscale morphological features without much loss in the optoelectronic nature of CNMs.

Hybrid materials of nanoscale to mesoscale morphologies having donor-acceptor heterojunctions can play a major role in the development of a variety of organic electronic devices.[25-28] In this context, fullerenes have been playing a major role as electron accepting materials. Depending upon the donor medium and experimental conditions, fullerenes tend to aggregate differently to generate nanostructures of diverse shape and dimensions.[29-33] C_{60} can self-assemble to form various nanostructures such as disks, wires and dots depending upon the nature of the solvent used for the processing. Choi and group have demonstrated the critical correlation between the geometry of the solvent and the final geometry of the self-assembled C_{60} structure.[34] C_{60} forms pseudo zero dimensional (*p*0D) spherical C_{60} dot structures in solvents like *n*-hexane. Evaporation of solvents from a solution of C_{60} in aromatic solvents results *p*1D structures. Theses *p*1D nanostructures are formed regardless of the polarity, size and number of the functional groups. Solvents having tetrahedral geometry such as $SiCl_4$, $SnCl_4$, CCl_4 etc. induce the self-assembly of C_{60} into pseudo two dimensional (*p*2D) hexagonal disk structures.[34] Ariga et al. have demonstrated structural transformation of 2D fullerene nanosheets to 1D nanorods by the interfacial precipitation using appropriate solvents.[35] The thermodynamic origin of these self-

assembled structures is the balance between the hydrophilic and hydrophobic environment. As a matter of fact, all these fullerene nanostructures retain their inherent optoelectronic properties, hence having significant fundamental applications as solar cell, field effect transistors and superconducting materials.[30,33-37] Therefore, in the search for new hybrid materials, fullerenes and π-conjugated systems remain as an attractive choice for scientists.[38-42]

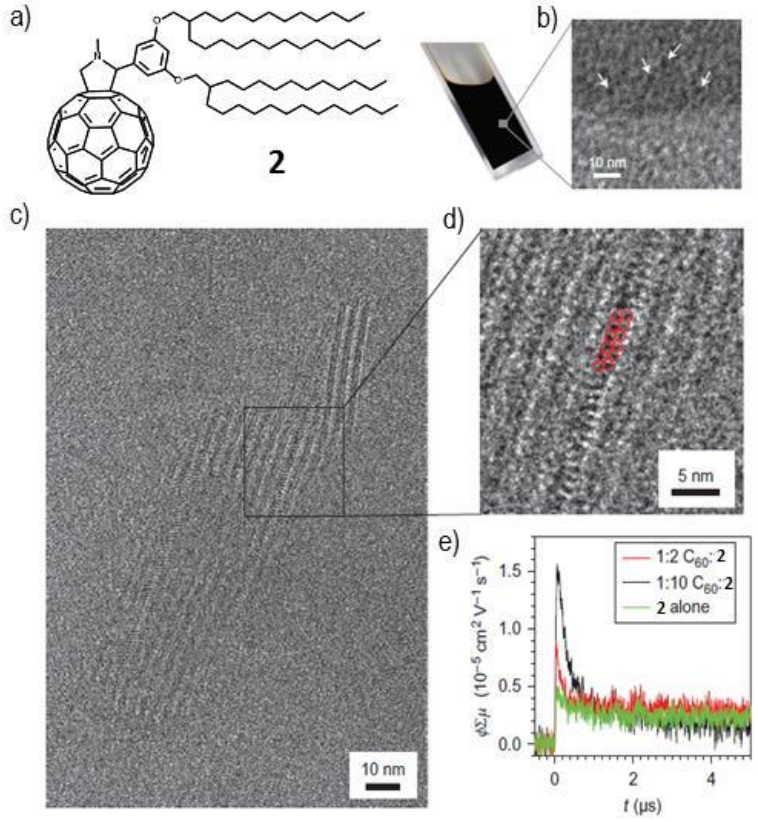

Figure 2.3. a) Chemical structure of molecule **2** and photograph of a solution in *n*-decane. b) Cryo-TEM image of micelles of **2** (White arrows indicate C_{60}-rich cores of the micelles). c) TEM image of lamellar mesophase formed by a 1:10 molar ratio of C_{60} and **2** at room temperature. d) Magnified area showing the interdigitated C_{60} units e) FP-TRMC data for pure **2** and mixtures of **2** and C_{60} in the solvent-free condensed phase.

Nakanishi and group showed a generalized approach to use solvophobic and solvophilic concept to construct nanostructures of different micro- and macroscopic properties.[40] Molecular level organization of hydrophobic fullerene derivative (**2**) is changed by tuning the balance of alkyl and *π*-conjugated content using selective solvents or additives (Figure 2.3). Addition of *n*-alkanes results in the micelles and hexagonally packed gel-fibers which can be ascribed due to the antipathy of C_{60} towards *n*-alkanes. The addition of pristine C_{60} increases the proportion of *π*-conjugated material which directs the assembly into lamellar mesophases containing a large fraction of optoelectronically active material and exhibit comparably high photoconductivity. *π*-Conjugated systems, particularly *π*-gels have a strong tendency to interact with C_{60}.[17] Interaction of C_{60} and C_{60} derivatives with gels and other media are known in the literature.[26,43-49] Martin et al. have demonstrated guided crystallization of fullerenes inside electroactive tetrathiafulvalene (exTTF) (**3**) based gel matrix.[26] Nucleation of C_{60}/PCBM crystals on the surface of exTTF-nanofibers, leading to the formation of 1D *n*/*p*-nanohybrids (Figure 2.4a). Donor and acceptor units are nanostructured at the same length scale guiding the crystallization of C_{60}/PCBM on top of exTTF-nanofibers. Efficient interfacing of exTTF-fibers with C_{60}/PCBM promotes electronic interactions between the electroactive species which in turn facilitate fast charge separation and slow charge recombination in 1D *n*/*p*-nanohybrids afforded with long lived charge carriers.

Gel phase crystallization of C_{60} in bis-urea based gel (**4**) is known to form C_{60} rods.[46] Zhang et al. have reported the supramolecular gel assisted self-assembly of fullerene leading to the formation of 1D nanorods better crystallinity (Figure 2.4b).

Supramolecular rod formation is driven by specific van der Waals interactions like hydrophobic, hydrophilic, and non-covalent interactions provided by the strong hydrogen bonding and π-π interactions between gelators. It should be noted that functionalized C_{60} is inferior with respect to electronic properties. In contrast crystallization of pristine C_{60} has more relevance and continues to be a challenge. Therefore, preparation of hybrid materials comprising of pristine C_{60} with π-systems, insights on their mode of interaction, morphological features of the resulting composites and their electronic properties are of great interest.

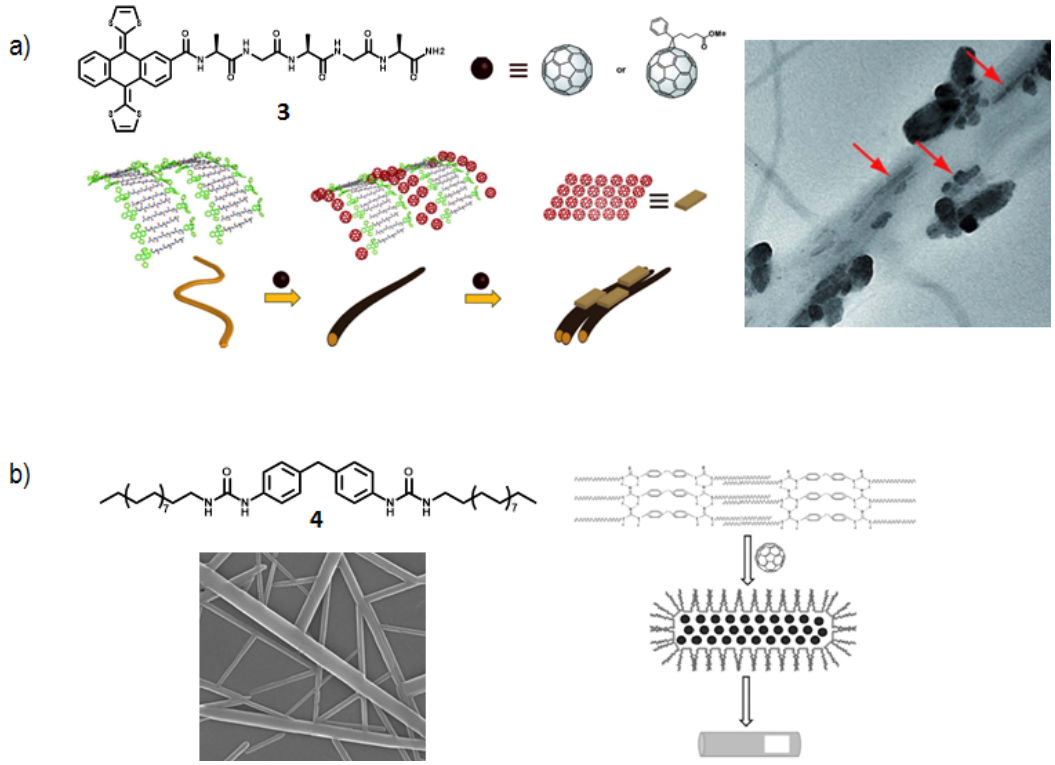

Figure 2.4. a) Chemical structure of **3** and schematic representation of guided crystal nucleation of C_{60} and on the exTTF fibers. TEM image of the nanohybrid (Right). (Red arrows show the C_{60} domains). b) Chemical structures of gelator **4** and SEM image of the xerogel prepared from gelator **4**/C_{60} (1:1) in toluene. Schematic representation of gel assisted crystallization of C_{60} (Right).

Organic gel medium has already been reported as a useful scaffold for the crystallization of polymorphic pharmaceutical molecules.[7,49,50] Encouraged by these studies, we attempted to understand the behavior of C_{60} in an OPV based π-gel matrix. Outcome of this study reveals parallel gelation and crystallization process of OPVs and C_{60}, respectively, leading to phase separation and crystallization of C_{60} as supramolecular rods with high photoconductivity.

2.3. Results and Discussion

2.3.1. The Design Strategy

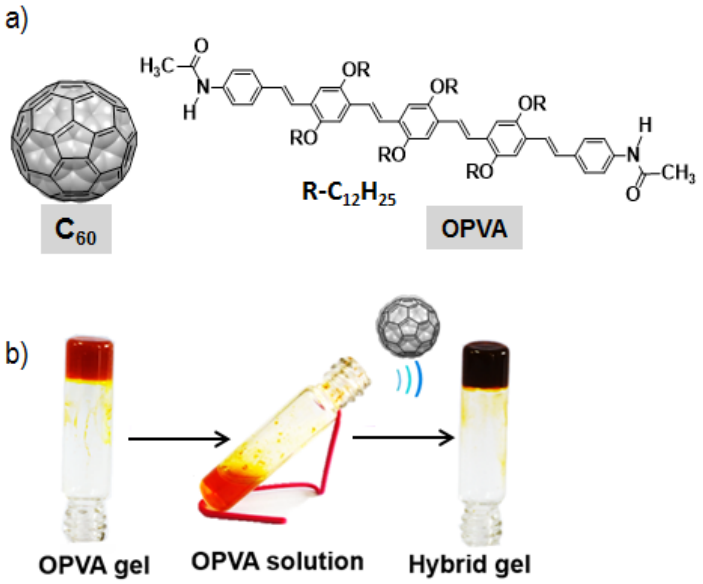

Figure 2.5. a) The structures of molecules (**OPVA** and C_{60}) used in this study. b) Thermo reversible gelation of **OPVA** with and without fullerene (C_{60}).

π-Gelators have strong affinity towards carbon allotropes such as C_{60}, carbon nanotubes and graphene.[49,23] Gelators of extended π-systems such as OPVs are

expected to interact with C_{60} in aliphatic and aromatic hydrocarbon solvents.[26,45,49] We have designed an OPV derivative (**OPVA**) having two terminal amide groups which determine the mode and extent of the intermolecular hydrogen bonding (Figure 2.5). π-π stacking and weak van der Waals interactions assist the self-assembly property of the molecule. Co-operative interactions of all these weak non-covalent forces eventually lead the molecules to form entangled nanoscopic structures which can hold large amount of appropriate solvent molecules within the self-assembled nanostructures to form thermo-reversible gel.

2.3.2. Synthesis of OPVA

The synthesis of **OPVA** was carried out as per the procedure shown in Scheme 2.1. Phosphonate ester of *p*-nitrobenzylbromide (**6**) on Wittig-Horner reaction with the OPV bisaldehyde **5**, which is prepared in several steps using known chemical reactions, achieved OPV nitro compound (**7**) in 85 % yield.[51]

The OPV amine was obtained after stannous chloride reduction of the compound **7** on refluxing under acidic condition, in 70% yield. **OPVA** was achieved with **8** and glacial acetic acid using 1-[bis(dimethylamino)methylene]-1H-1,2,3-triazolo[4,5-*b*]pyridinium3-oxide hexafluoro phosphate (**HATU**) in the presence of diisopropylethylamine in dichloromethane in 55% yield.

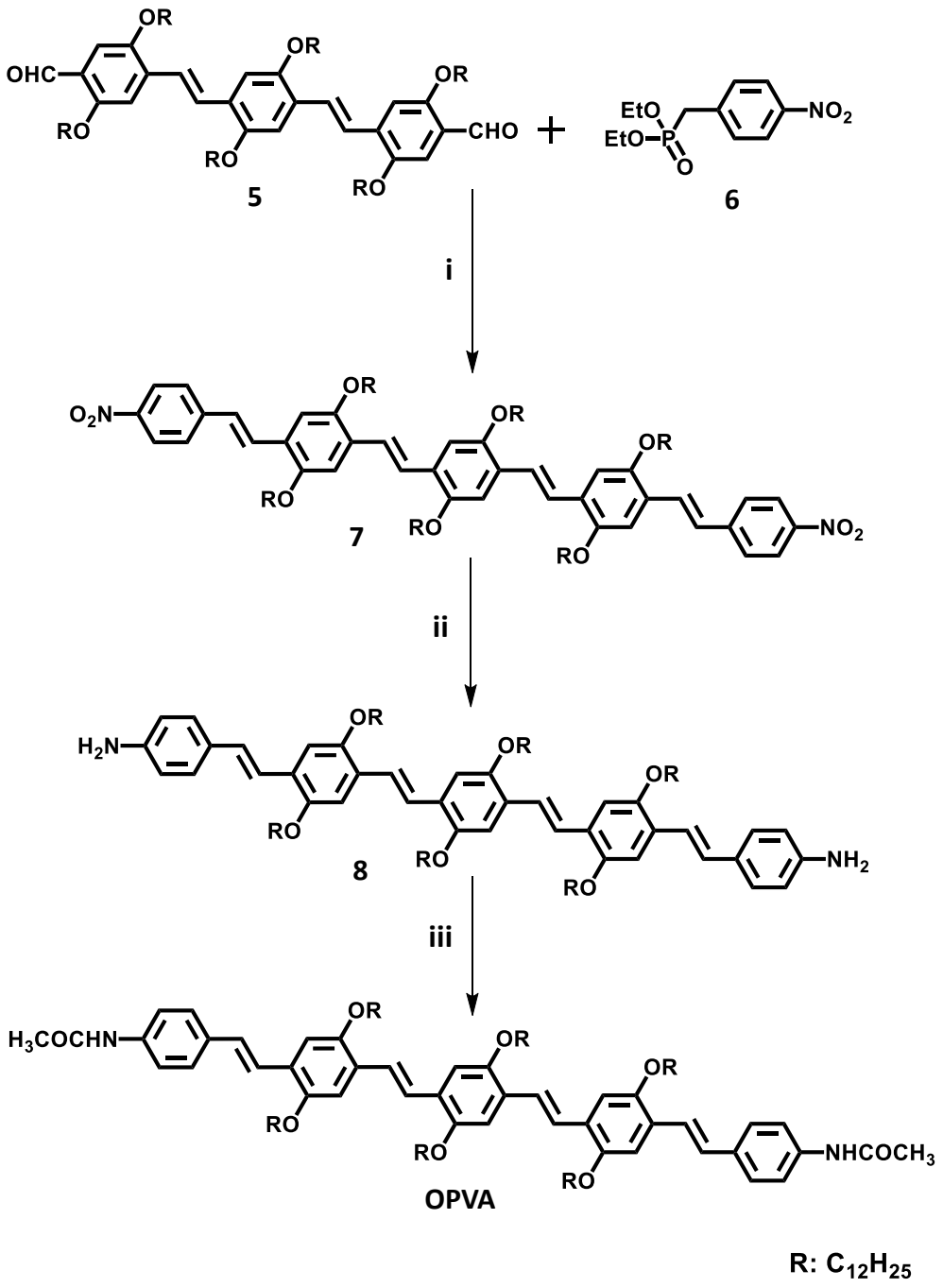

Scheme 2.1. Reagents and conditions: i) NaH, THF, 60 ^{o}C, 6 h, ii) $SnCl_2.2H_2O$, THF, HCl, 5 h, iii) HATU, diisopropylethylamine, dichloromethane, glacial acetic acid, 0 ^{o}C - rt, 24 h.

2.3.3. Interaction of OPVA with C_{60}

With the objective of preparing hybrid π-gels with improved electronic properties, we studied the interaction of C_{60} with **OPVA** in different ratios in toluene (Figure 2.5). It is observed that the gel melting temperature (T_{gel}), which is a direct measure of the gel stability, increases with the addition of each fullerene equivalent (Figure 2.6). Enhancement in the T_{gel} values indicates that the colloidal assemblies in the hybrid gels are sufficiently stronger than the bare **OPVA** gelator. In fact, it was observed that the rate of increase of gel strength was much faster up to 2 equivalent of C_{60} where the gel strength increases with a steeper slope (1.25). From 2-6 equivalents of C_{60} addition, the rate of increase in gel melting temperature is almost reduced to half (slope: 0.625) before getting saturated (Figure 2.6).

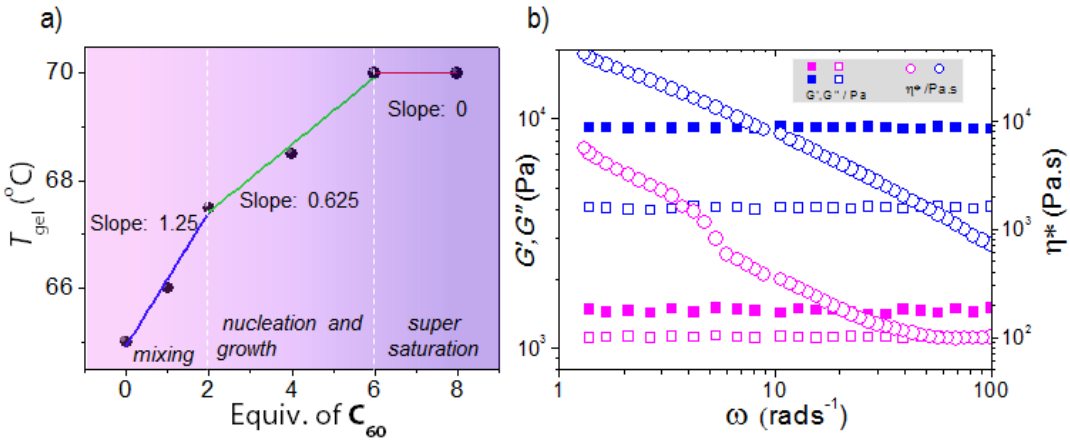

Figure 2.6. a) T_{gel} as a function of fullerene concentration. b) Rheological data of **OPVA** (5×10^{-4} M) and **OPVA**/C_{60} (1:6) showing a change in the complex viscosity (η^*), storage modulus (G'), and loss modulus (G'') with angular frequency (ω).

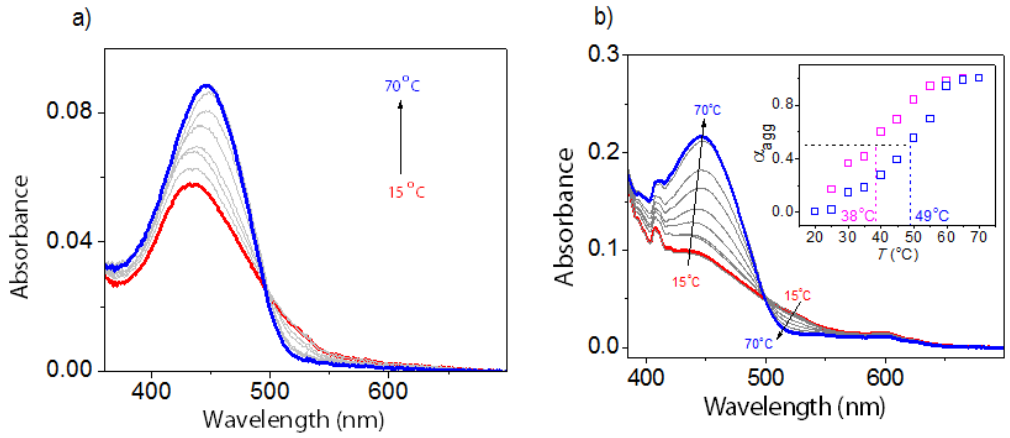

Figure 2.7. Variable temperature absorption spectra of a) **OPVA** and b) **OPVA**/C_{60} (1:6) in toluene (Concentration of **OPVA**, 1 × 10^{-5} M). Inset shows variation of fraction of aggregates (α_{agg}) with temperature (T).

In order to compare the mechanical strength of the **OPVA** and the **OPVA**/C_{60} (1:6) hybrid gel, rheological measurements were performed. Figure 2.6 illustrates the rheological response as a function of the angular frequency at a fixed strain for **OPVA** gels with and without C_{60}. Both gels showed a plateau region when the angular frequency was varied from 100 to 1 $rads^{-1}$. Both gels show substantial elastic response and G' values are larger than the G'' values over the entire range of frequencies. By the addition of fullerene, the value of G' is found to increase by an order of magnitude in comparison to **OPVA**. The ratio of G' and G'' is higher for the hybrid gel than that of the **OPVA** gel, indicating the better robustness of the former. Quasi-solid nature of the composite gel is higher (tan $\delta = G''/G' = 0.43$-0.45) than that of **OPVA** gel (tan $\delta = 0.75$-0.77).[52] The complex viscosity (η^*) of the hybrid gel was also found to be more when compared to that of the **OPVA** gel.

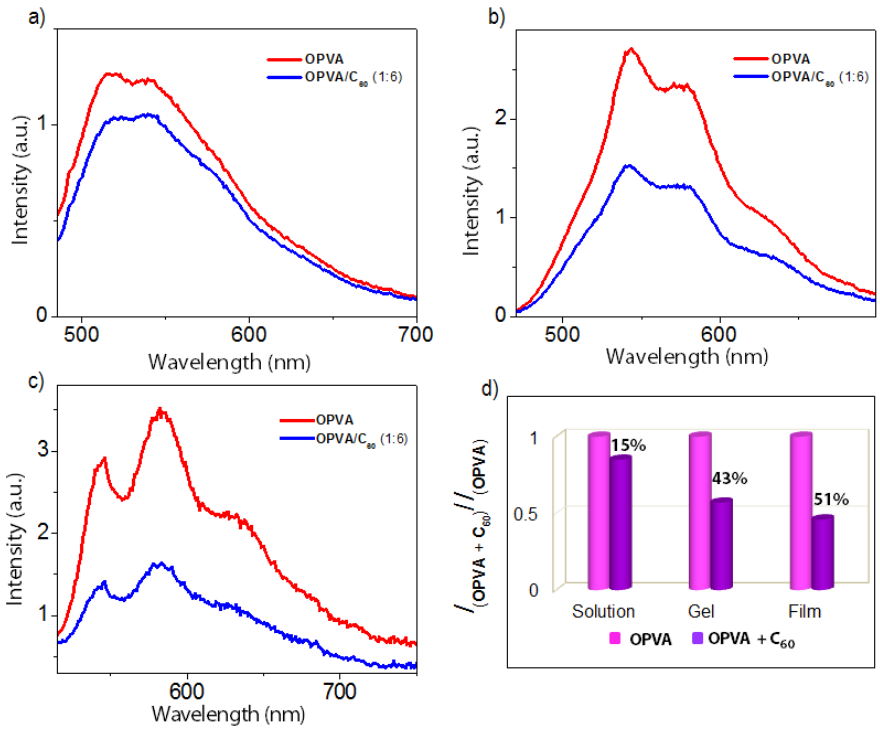

Figure 2.8. Emission spectra of **OPVA** and **OPVA**/C_{60} (1:6) in a) solution state, b) gel state and c) film state. d) Extent of emission quenching in **OPVA**/C_{60} hybrid in different states (All emission spectra were obtained by exciting at 440 nm and normalized for comparison).

Variable temperature absorption studies in the solution state (1×10^{-5} M in toluene) gave evidence for the influence of C_{60} on the supramolecular assembly of **OPVA** (Figure 2.7). Upon aggregation, absorbance at λ_{max} (440 nm) decreases with a notable blue shift for **OPVA** as well as **OPVA**/C_{60} (1:6). Even though this observation indicates the formation of *H*-type aggregates in both cases, there is considerable difference in the thermal stability of the aggregates (Figure 2.7 inset).[53] Melting transition temperature (T_m, temperature at which α_{agg} = 0.50) for hybrid aggregates (T_m = 49 °C) is found to be higher than that of the self-assembled

aggregates of **OPVA** (T_m = 38 ºC). Greater thermal stability of the hybrid aggregates is attributed to the close packing of the molecules.

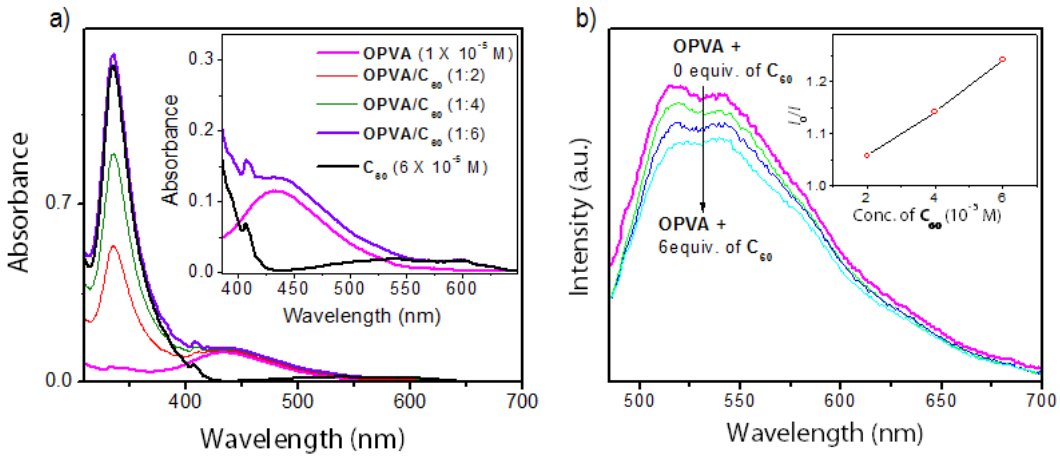

Figure 2.9. a) Absorption spectra of **OPVA** with different equivalents of C_{60} (Inset: Zoomed region of 400 - 650 nm shows the negligible absorption of C_{60} at 440 nm). b) Emission spectra of **OPVA** upon addition of different amount of C_{60}. (Inset shows Stern-Volmer plot). All emission spectra were recorded upon excitation at 440 nm.

This is further reciprocated in quenching of **OPVA** fluorescence due to excited state interactions with C_{60}.[54] These interactions are found to be more prominent as we move from the solution to the film state (Figure 2.8). In order to rule out the quenching of emission due to light partitioning in the solution state, the emission spectra of all samples were recorded by exciting at 440 nm at which C_{60} has negligible absorption (Figure 2.9a). Moreover a linear Stern-Volmer plot (Figure 2.9b inset) from solution state emission quenching studies (maximum acceptor concentration: 6×10^{-5} M) reveals the dynamic nature of quenching process.

2.3.4. Morphological Analysis

Transmission electron microscopic (TEM) analysis of **OPVA** xerogel revealed micrometer long supramolecular tapes of width varying from 50 - 100 nm. TEM images of C_{60} showed formation of clusters having size in the range of 100 - 200 nm (Figure 2.10). Interestingly, TEM analysis of the hybrid gels with different compositions of **OPVA**/C_{60} revealed the formation of C_{60} clusters and rods on the supramolecular tapes of **OPVA** at varying concentrations of C_{60} (Figure 2.10c,d).

This observation fairly matches with the atomic force microscopic (AFM) and scanning electron microscopic (SEM) analyses of both the samples (Figure 2.11). At the low molar ratio of C_{60} (1:1 to 1:2) fullerene clusters were formed which gradually spread out to nucleate the growth of fullerene rods (Figure 2.12a,b). Upon increasing the concentration of fullerene (**OPVA**/C_{60} = 1:4), the growth of 1D fullerene domains was observed (Figure 2.10c). Above 1:6 molar ratio of C_{60}, micrometer-sized crystalline fullerene rods were exclusively formed along with phase separated **OPVA** nanofibers (Figure 2.10d). However, the substantial increase in the viscosity of **OPVA** gel with the addition of C_{60} indicates the interaction of the gelator and the solvent molecules with the C_{60} microstructures at a macroscopic level. This is clear from the Figure 2.12c which reveals the entanglement of fullerene rods with the supramolecular tapes of **OPVA**. Average dimensions of these supramolecular rods are 1-2 μm in length and 125 nm in width (Figure 2.13).

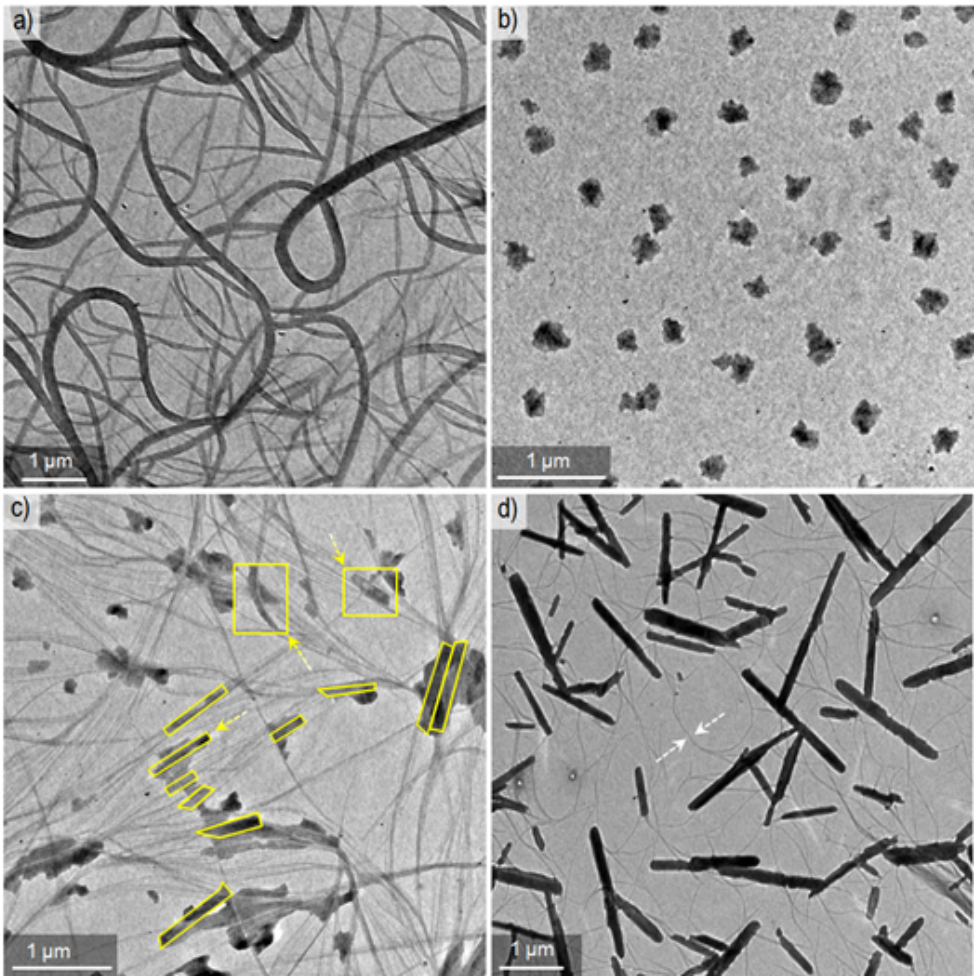

Figure 2.10. TEM image of a) **OPVA** tapes, b) C_{60} clusters, and c) **OPVA**/C_{60} composite in 1:4 ratio. Fullerene domains in the **OPVA** matrix (Yellow boxes) and yellow arrows show the growth direction of domains. d) **OPVA**/C_{60} composite in 1:6 ratio. White arrows show supramolecular tapes of **OPVA** (Concentration of **OPVA** = 1×10^{-5} M in toluene).

The restricted mobility of the solvent within the gel medium and the enhanced local concentration of C_{60} between the interstitial spaces of **OPVA** assemblies facilitate the nucleation of C_{60} supramolecular rods. The amide H-bond interaction and the strong π-π interactions between the **OPVA** molecules prevent the interaction of **OPVA** with C_{60}, which facilitates a phase separation between the two systems.

With the gradual increase in the local supersaturation gradient of C_{60} near the supramolecular gel fibers, mesoscopic linear domains of C_{60} start to grow along the interstitial space of the bundled **OPVA** nanofibers. Crystallization started at this stage will be followed by elongation process in a non-equilibrium manner to form nanorods until the local supersaturation gradient is depleted and complete mesoscale phase segregation is achieved.

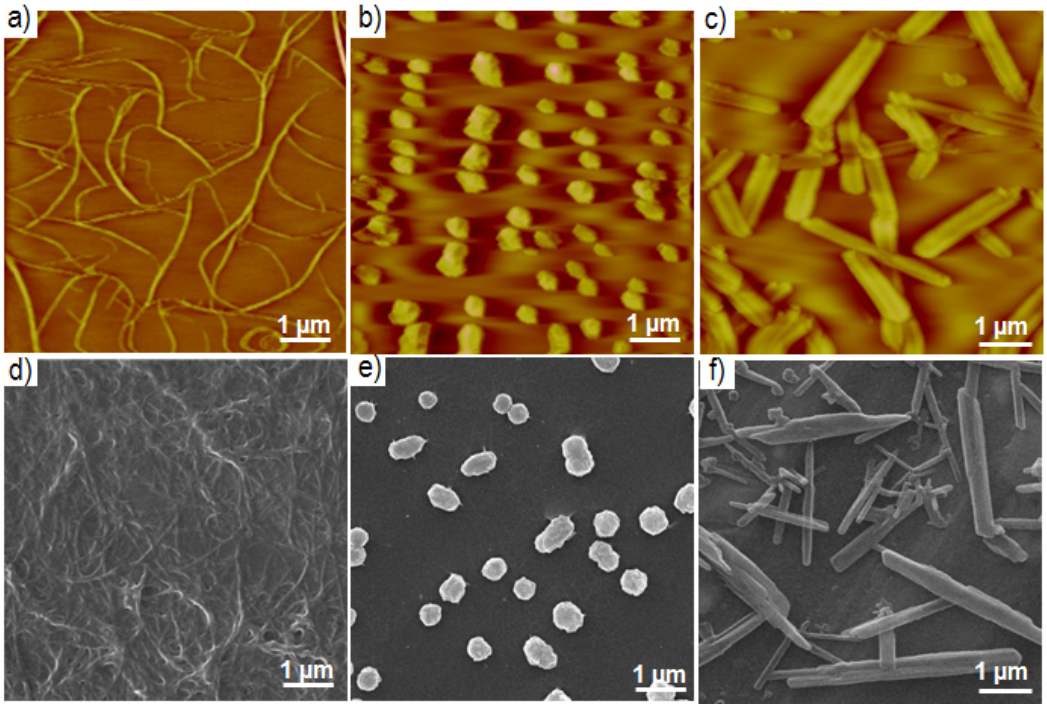

Figure 2.11. a-c) AFM and d-f) SEM images of a, d) **OPVA**, b, e) C_{60} and c, f) **OPVA**/C_{60} (1:6) (Concentration of **OPVA** = 1×10^{-5} M in toluene).

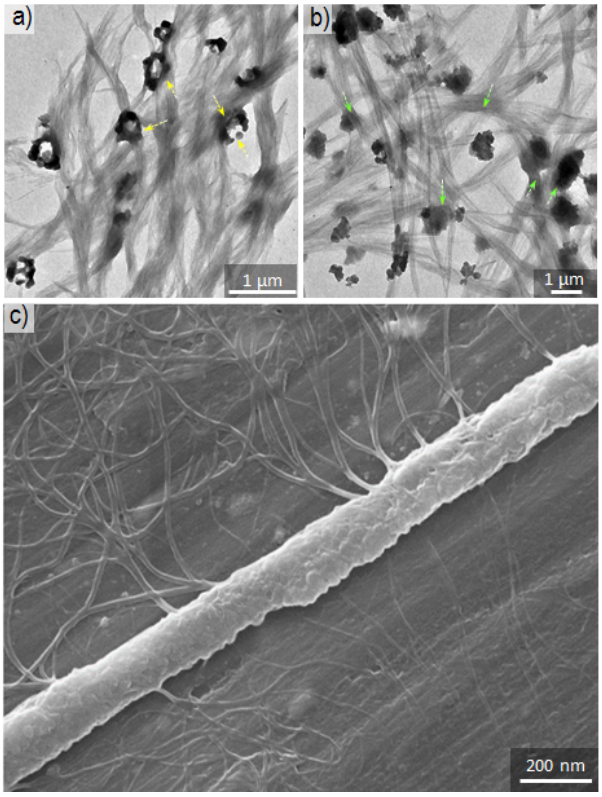

Figure 2.12. TEM image of a) **OPVA**/C_{60} in 1:1 and b) 1: 2 ratios (Concentration of **OPVA** = 1 × 10^{-5} M in toluene). Yellow and green arrows represent the gradual breaking down and mixing of C_{60} clusters with **OPVA** tapes. c) SEM image of C_{60} rod wrapped by **OPVA** fibers.

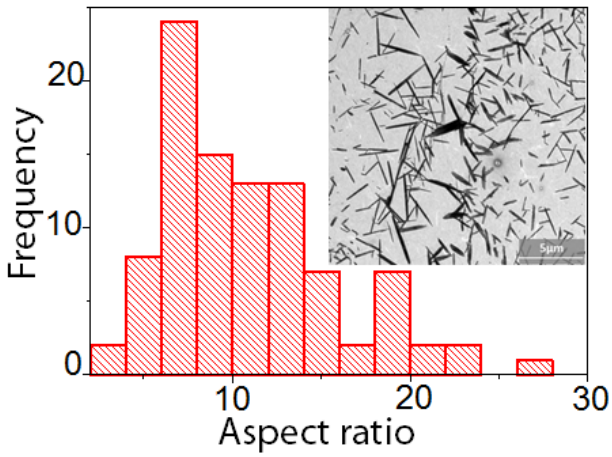

Figure 2.13. Histogram of C_{60} rods grown inside the **OPVA** gel matrix (Inset shows corresponding TEM image).

Fullerene nanorods grown inside the gel medium, showed molecular level arrangement with well-ordered lattice fringes. Polycrystalline nature of the bulk fullerene is clear from the high-resolution TEM studies and the fast fourier transformation (FFT) pattern (Figure 2.14). Careful examination of the high-resolution images and FFT patterns further proves the improved crystallization behaviour of fullerene inside the supramolecular gel medium. These fullerene rods formed in the gel medium exhibited better crystalline nature (Figure 2.14) than the fullerene crystals grown from toluene under ambient conditions. Reconstructed high-resolution TEM (HRTEM) image of the fullerene rods clearly shows crystallized C_{60} domains (Figure 2.15).

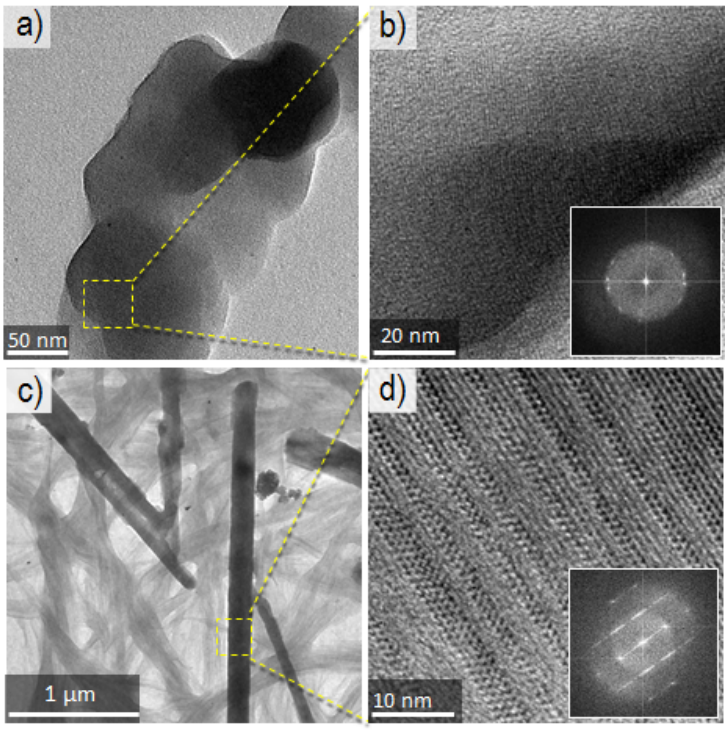

Figure 2.14. HRTEM images of a) and b) bulk C_{60} and c) and d) C_{60} rods grown inside the gel medium. Insets show respective FFT patterns of the images.

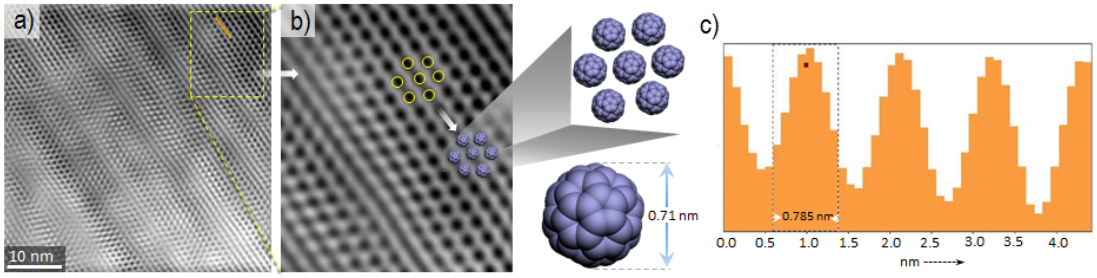

Figure 2.15. a) Processed TEM image of C_{60} rods grown inside gel using the Gatan Microscopy Suite software. b) Magnified image of the area in yellow box of a) showing closely packed fullerenes in yellow circles. Molecular dimension of C_{60} is represented. c) Line profile corresponding to the orange line drawn in image a).

The line profile in Figure 2.15a showed a distance of 0.79 nm, which was repeatedly observed between regions of same contrast (Figure 2.15c). This value fairly matches with the diameter (0.71 nm) of a C_{60} molecule and HRTEM image of C_{60} reported in the literature.[55]

2.3.5. Structural Elucidation from X-ray Diffraction Experiments

Wide-angle X-ray scattering (WAXS) measurement was conducted on bulk C_{60}, **OPVA** xerogel and the hybrid xerogel (Figure 2.16). The diffraction peaks obtained in bulk C_{60} matched well with the standard face-centered cubic (fcc) crystal phase (JCPDS card no. 00-043-0995).[56] The results also confirmed the complete absence of hexagonal close-packed (hcp) structure (Figure 2.17).[57] Diffraction peaks with *d*-spacing of 8.4, 4.4, 3.5 and 3.4 Å are indexed as (111), (311), (222) and (331) planes from the fcc lattice. These peaks were unaltered in the hybrid xerogel, justifying a

retained fcc packing of the fullerene rods important for better charge transport due to close packing of the C_{60} molecules.[58]

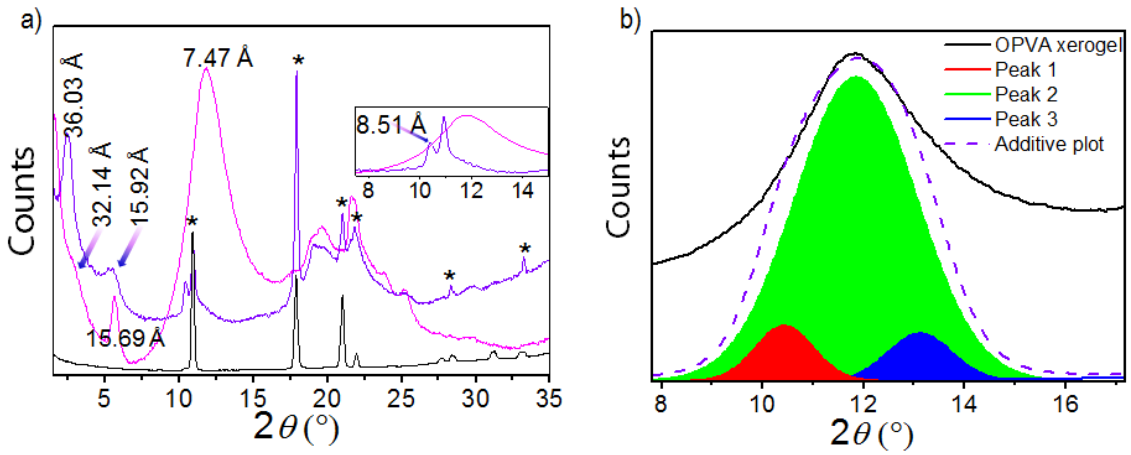

Figure 2.16. a) WAXS pattern of **OPVA** (Pink), **OPVA**/C_{60} (1:6) (Violet), and C_{60} (Black). b) Deconvoluted spectra of the X-ray diffraction (XRD) peak of **OPVA** at 7.47 Å.

The noticeable diffraction peaks observed in the case of **OPVA** xerogel includes a broad shoulder corresponding to a *d*-spacing of 32.1 Å, a sharp peak corresponding to 15.7 Å and a broad, intense peak corresponding to an average *d*-spacing value of 7.47 Å. Deconvolution of the third peak gives us access to three diffraction peaks contributing towards its broadness. Deconvoluted peaks 1, 2 and 3 correspond to a *d*-spacing value of 8.48, 7.47 and 6.74 Å, respectively (Figure 2.16b). These peaks can be assigned to a mixture of *syn*- and *anti*-oriented catemers of **OPVA** and matches well with the distance between the molecular stacks, i.e. 32.1 and 15.3 Å along the width and length of the tape justifying short (broad shoulder) and long range (sharp peak) order, respectively.[53]

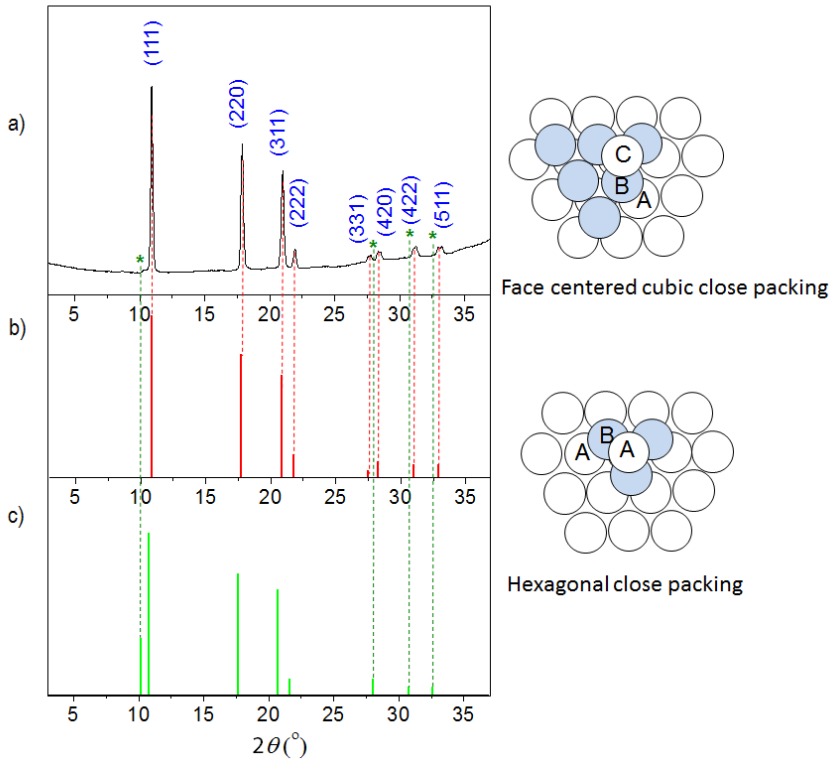

Figure 2.17. Comparative XRD patterns of a) C_{60}. b) fcc packed C_{60} and c) hcp packed C_{60}. Peaks shown with asterisks differentiate hcp and fcc packing of C_{60}. Schematic illustration of fcc and hcp packing are also shown. The letters indicate the type of layers. In fcc packing all the three layers are different, whereas in hcp stack alternate layer are packed in same fashion.

Presence of both *syn* and *anti*-oriented catemers in **OPVA** tapes results in the variation of the distance between the planes, containing the amide functionality in the alternately stacked **OPVA** molecules. This observation explains the broadening of the peak at 7.47 Å. In the hybrid gel, the first peak corresponds to a *d*-spacing of 36 Å, followed by a hump at 15.9 Å and the third peak corresponds to a *d*-spacing of 8.51 Å. From our morphological investigations, we observed that on addition of C_{60}, the **OPVA** tapes are chopped down into thinner fibers.

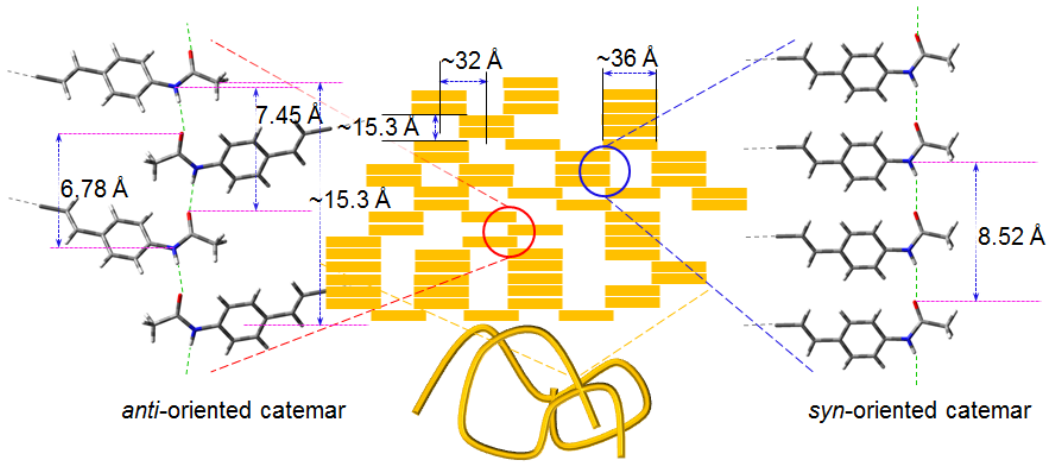

Scheme 2.2. Schematic representation of *anti*- and *syn*-oriented catemer formation in **OPVA** assembly, leading to the formation of tapes.

A probable explanation of this observation may be that in the hybrid gel, compartmentalization of C_{60} occurs within *syn*-oriented **OPVA** catemer domains, the width of which corresponds to the molecular length of **OPVA** (36 Å). The reduction in the number of *anti*-oriented catemers joining the *syn*-oriented catemer stacks in the hybrid gel, results in the thinning of the **OPVA** tapes (Scheme 2.2). The abundance of *syn*-oriented **OPVA** catemers in the thin hybrid gel fibers results in a uniform distance between the planes containing the amide functionality (8.52 Å) between alternately stacked **OPVA** molecules. This probably explains the gradual shifting and sharpening of the peak (corresponding to a *d*-spacing of 8.51 Å) in the hybrid gel (Scheme 2.3). The molecular distances have been calculated based on the crystal structure of acetanilide and benzanilide, which crystallizes in the *anti*- and *syn*-oriented catemer, respectively.[59-61]

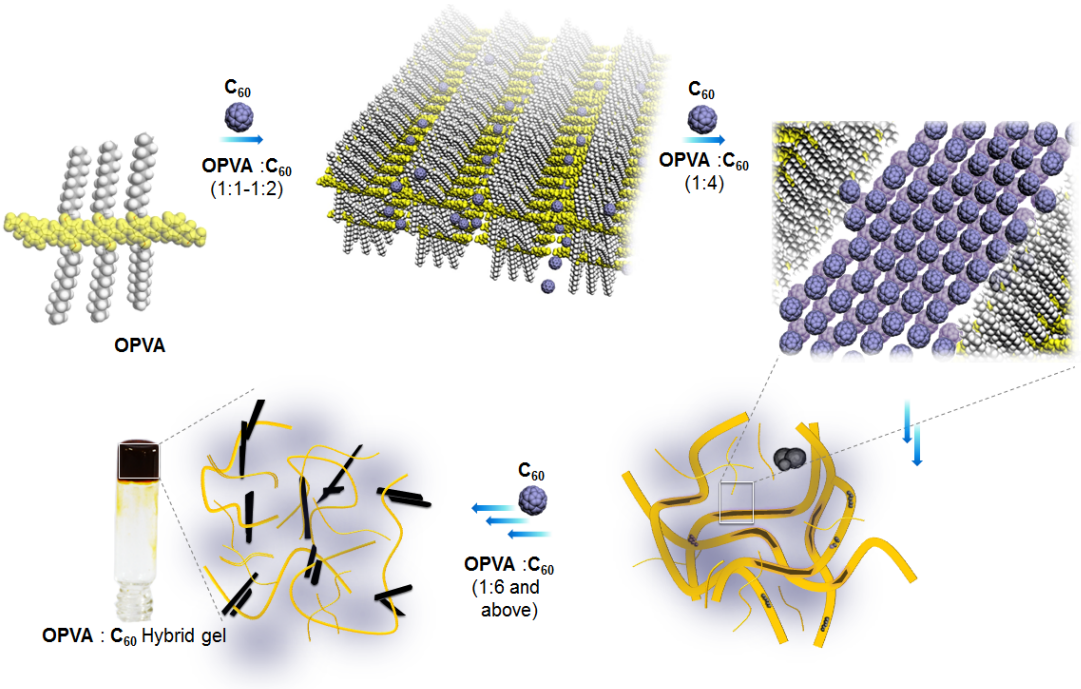

Scheme 2.3. Plausible scheme of formation of C_{60} rods in **OPVA**/C_{60} composites.

2.3.6. Charge Transport Properties

Since the fullerene supramolecular rods are expected to be photoconducting, flash-photolysis time resolved microwave conductivity (FP-TRMC) measurements were conducted, which is an electrodeless technique to evaluate intrinsic photoconductivity of the material with minimum trapping effects.[62,63]

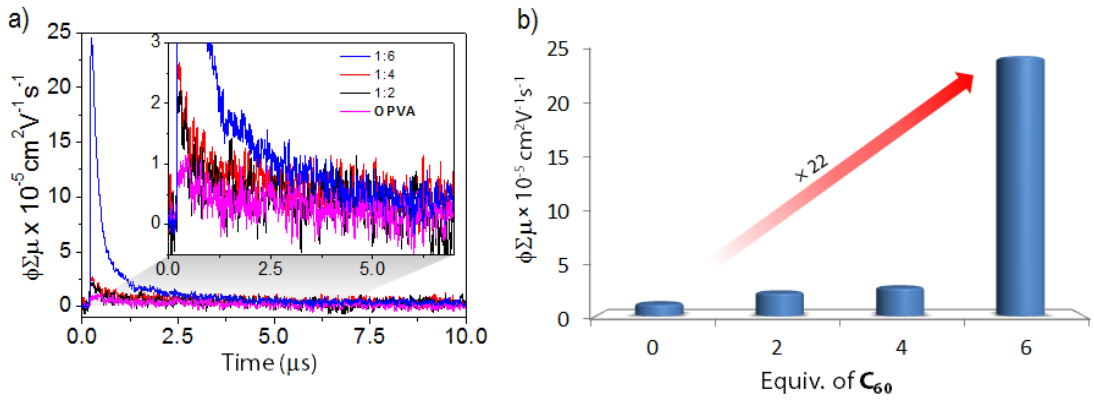

Figure 2.18. a) FP-TRMC data for **OPVA** with different ratio of C_{60}. Graph is zoomed to show the variation of conductivity in the lower ratio of C_{60}. b) Secondary plot showing the variation of the φΣμ value for **OPVA** with different ratios of C_{60}. The value increases 22-fold in the case of **OPVA**/C_{60} (1:6) blend.

Figure 2.18 quantifies intrinsic photoconductivity in terms of φΣμ values, where φ is the charge-carrier generation quantum yield upon photoexcitation and Σμ represent the sum of charge-carrier mobilities. The maximum value ($\varphi\Sigma\mu_{max}$) usually signifies the intrinsic short-range charge-carrier mobility. The measurements showed a $\varphi\Sigma\mu_{max}$ value of 2.0×10^{-5} and 2.5×10^{-5} $cm^2V^{-1}s^{-1}$ for **OPVA**/C_{60} blends of molar ratio 1:2 and 1:4, respectively. The $\varphi\Sigma\mu_{max}$ increases by ~ 22 fold to a value of 2.4×10^{-4} $cm^2V^{-1}s^{-1}$ (Figure 2.18b) for a 1:6 blend ratio of **OPVA**/C_{60} compared to that of **OPVA** xerogel ($\varphi\Sigma\mu_{max} = 1.1 \times 10^{-5}$ $cm^2V^{-1}s^{-1}$). The sudden increase found between **OPVA**/C_{60} = 1:6 and **OPVA**/C_{60} = 1:4 is probably due to the increase in Σμ because of better electron percolation pathways in the extended fullerene nanorod.[64]

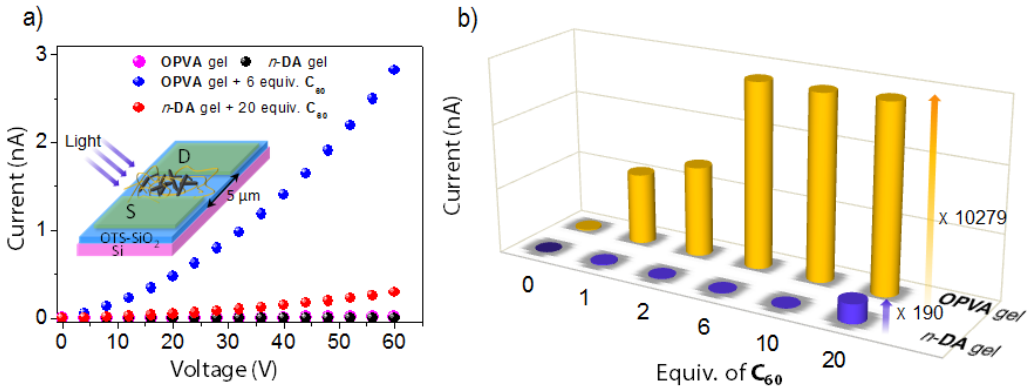

Figure 2.19. a) I-V characteristics of gelators and their respective hybrid samples (at the bias voltage of 20 V). Inset shows the device configuration. b) Comparison of photocurrent generation from C_{60} in two different gel media (Concentration of gelator = 1×10^{-5} M in toluene). Upon addition of 20 eq of C_{60}, the photocurrent generated is ~ 10^4 times in **OPVA**, whereas a 190 - fold increase is found in the non-*π*-gelator [*n*-decanamide (*n*-**DA**)].

Further, the electrical transport in the fullerene rods is studied by photocurrent measurement of spin coated xerogel samples on organic field effect transistor platform (Figure 2.19).[58,65,66] Current-Voltage (I-V) characteristics illustrate considerable enhancement in the photocurrent with increase in C_{60} content in **OPVA**/C_{60} blends. Random aggregates formed at the low concentration of C_{60} do not conduct well due to nanoscale discontinuity combined with the dimensional limitations, which is already demonstrated in morphological studies. As the ratio of fullerene increases, photoresponse of the composite enhances hinting towards the importance of nano to mesoscale phase segregation and formation of heterojunctions in the transport properties. Advantages of long-range mesoscale phase segregation and molecular space confinement in the fullerene rods facilitates the efficient charge transport at 6 equivalents of fullerene and above.

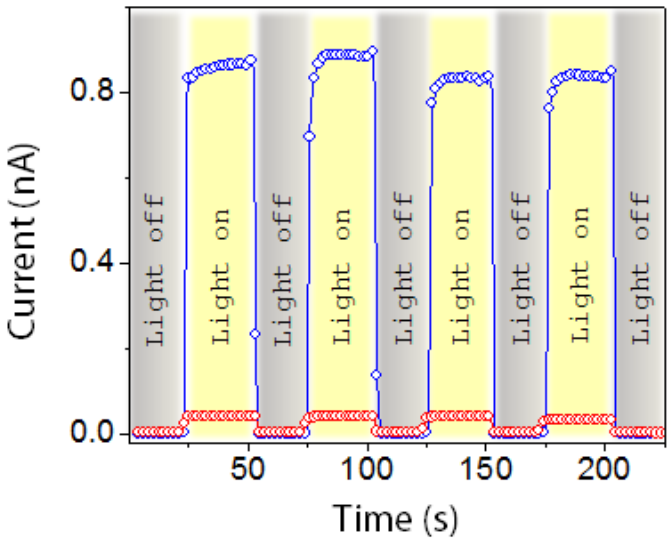

Figure 2.20. Photoresponse characteristics of the devices (at the bias voltage 20 V) constructed from (Blue) **OPVA**/C_{60} and (Red) *n*-**DA**/C_{60}. (Gelator/C_{60} ratio is 1:20).

Supramolecular gel-assisted growth of fullerene rods is an interesting example of gel phase crystallization. Gelation and crystallization are two orthogonal processes, which occur at different rates. Outcome and properties of the resultant nanostructures from these orthogonal assemblies depend on effective phase separation, which in turn depends on the weak and slow interaction between gelator and crystallizing substrate in this multicomponent assembly. Therefore, in order to justify the effect of π-gel medium, **OPVA** was replaced by *n*-decanamide (*n*-**DA**) which is a non-π-conjugated gelator. When compared to the **OPVA**/C_{60} system, the hybrid gel obtained from *n*-**DA**/C_{60} showed low photoconductivity although the formation of nanoscale C_{60} rods is reported in case of gelators without a π-backbone (Figure 2.19).[45]

Reversible photoresponse of the fullerene nanostructures from both gels is illustrated in the photocurrent time profile (Figure 2.20). Interestingly, it is observed that excess loading of C_{60} is required in the gel matrix of *n*-**DA** to generate a substantial photoresponse. Therefore, it can be said that more than acting as a medium for crystallization, supramolecular gel matrix of **OPVA** play the role of an active material which connect nanorods with each other having continuous charge carrier pathway in micrometer dimensions. In contrast to the *π*-gel medium, *n*-**DA** provides a rather insulating environment that reduces electrical transportability.

2.4. Conclusions

The supramolecular tapes of the **OPVA** *π*-gelator are found to be an excellent scaffold for the crystallization of C_{60} as supramolecular rods. Phase separation and orthogonal self-assembly of **OPVA** and C_{60} occurs within the gel medium resulting in hybrid gels comprising of crystalline fullerene rods. The strong *π*-*π* interaction and H-bonding between the **OPVA** molecules prevents **OPVA**-C_{60} interaction, thus facilitating the phase separation between the two. Morphological studies established the concentration dependency of the supramolecular rod formation. The supramolecular gel medium slows down the rate of crystallization of C_{60} molecules. Crystallization at slower rate results in molecular level ordering leading to higher crystallinity of the supramolecular fullerene rods. Interestingly, the C_{60} rods formed in the *π*-gel medium exhibited relatively high photocurrent generation when compared to C_{60} dispersed in a non-*π*-gel medium. Formation of donor-acceptor heterojunctions in nanoscale level is proved by transient photoconductivity

measurements. Transient conductivity depends on the composition ratio of fullerene, which in turn also affect the nano to mesoscale morphology of this orthogonal self-assembling system. This study opens up the possibility of exploring a variety of π-gels as scaffolds for the assembly of carbon allotropes and their use in optoelectronic applications.

2.5. Experimental Section

2.5.1. Synthesis and Characterization

Unless otherwise stated, all organic starting materials and reagents were purchased from commercial suppliers and used without further purification. Amide functionalized oligo(*p*-phenylenevinylene) based gelator (**OPVA**) was synthesized according to the reported procedure and characterized by standard methods.[53]

Synthesis of Compound 7: To a solution of the bisaldehyde **5** (100 mg, 0.20 mmol) and the phosphonate ester **6** (50 mg, 0.46 mmol), in 35 mL THF, NaH (30 mg, 1.24 mmol) was carefully added under argon atmosphere. The reaction mixture was refluxed for 6 h, and the solvent was removed under reduced pressure. The resultant residue was extracted with chloroform and washed several times with saturated brine and water. Concentration of the organic layer followed by column chromatography (hexane/chloroform, 3:1) over silica gel (100-200 mesh) gave **7** as a dark red solid in 85% yield. m.p.: 245 ± 2 °C; FT-IR (KBr) ν_{max}: 668, 860, 964, 1206, 1421, 1466, 1514, 1600, 1661, 2850, 2922, 3447 cm^{-1}; ^1H NMR (500 MHz, $CDCl_3$, TMS) δ (ppm): 0.86-0.89 (t, 18H, $-CH_3$), 1.24-1.36 (m, 120H, $-CH_2-$), 4.03-4.07 (t, 12H, $-OCH_2-$), 7.10-7.14 (d, 2H, vinylic), 7.15-7.21 (d, 2H, vinylic), 7.15-7.18 (t, 4H,

vinylic), 7.39 (s, 2H, aromatic), 7.44 (s, 2H, aromatic), 7.48-7.51 (d, 4H, aromatic), 7.06-7.1 (d, 4H, aromatic); ^{13}C NMR (125 MHz, $CDCl_3$) δ (ppm): 14.12, 14.36, 22.69, 26.21, 26.30, 29.38, 29.47, 29.53, 29.67, 29.72,31.92, 60.28, 69.20, 69.39, 110.09, 110.60, 112.31, 117.86, 123.19, 124.93, 127.38, 130.52, 139.74, 150.62, 151.17, 152.49, 167.58; MALDI-TOF MS: Calculated *m*/*z* for $C_{110}H_{172}N_2O_{10}$: 1681.13, found: 1682.28.

Synthesis of Compound 8: Compound **7** (100 mg, 0.18 mmol) and $SnCl_2$. $2H_2O$ (550 mg, 6.75 mmol), were added to tetrahydrofuran (15 mL), followed by 4 drops of 37% HCl. The reaction mixture was stirred and refluxed for 5 h. After cooling, dichloromethane (50 mL) was added and washed once with 0.1 M sodium bicarbonate and two times with water. The solvent was removed from the organic layer on a rotary evaporator and the crude product was passed through a silica pad using dichloromethane as the eluent to afford **8** with 70% yield. m.p.: 251 ± 2 °C; FT-IR (KBr) ν_{max}: 668, 717, 804, 858, 963, 1072, 1205, 128, 1350, 1422, 1465, 1506, 1607, 1661, 2849, 2921, 2954, 3436 cm^{-1}; ^{1}H NMR (500 MHz, $CDCl_3$, TMS) δ (ppm): 0.86-0.89 (t, 18H, -CH_3-), 1.24- 1.36 (m, 120H, -CH_2-), 4.03-4.07 (t, 12H, -OCH_2-), 6.3 (m, 4H, -NH_2-), 6.67-6.70 (d, 4H, aromatic), 7.02-7.15 (m, 8H, aromatic), 7.32- 7.37 (m, 4H, aromatic), 7.43-7.48 (m, 6H, aromatic); ^{13}C NMR (125 MHz, $CDCl_3$) δ (ppm): 14.10, 22.68, 26. 25, 26.32, 29.56, 31.92, 69.53, 110.59, 115.22, 119.97, 123.28, 127.38, 128.65, 128.82, 145.91, 150.85, 151.06; MALDI-TOF MS: Calculated *m*/*z* for $C_{110}H_{176}N_2O_6$: 1622.63, found: 1622.58.

Synthesis of OPVA: To a dry dichloromethane solution of the OPV amine **8** (100 mg, 0.06 mmol) and glacial acetic acid (10 mg, 0.15 mmol) kept at 0 ^{o}C, was added

diisopropylethylamine (20 mg, 0.15 mmol) and **HATU** (60 mg, 0.15 mmol). The reaction mixture was stirred for 24 h at room temperature, filtered and washed several times with water. The filtrate was dried over anhydrous sodium sulphate and the solvent was evaporated under reduced pressure. The crude product was purified by eluting through a neutral alumina column using hexane/chloroform (3:7) mixture. Yield: 55%; m.p.: 245 ± 2 °C; FT-IR (KBr) ν_{max}: 721, 850, 964, 1034, 1071, 1205, 1257, 1316, 1350, 1387, 1421, 1466, 1513, 1595, 1663, 2851, 2922, 3049, 3296, 3412 cm^{-1}; ^{1}H NMR (500 MHz, $CDCl_3$, TMS) δ (ppm): 0.86-0.89 (t, 18H, $-CH_3-$), 1.24-1.36 (m, 120H, $-CH_2-$), 4.03-4.07 (t, 12H, $-OCH_2-$), 7.02-7. 15 (m, 6H, aromatic), 7.32-7.37 (m, 6H, aromatic), 7.44- 7.5 (m, 10H, aromatic), 8.3 (s, 2H, -NH-); ^{13}C NMR (125 MHz, $CDCl_3$) δ (ppm): 14.12, 14.36, 22.69, 25.90, 29.38, 29.6, 29.72, 31.92, 69.20, 114.31, 117.86, 123.19, 124.93, 127.38, 130.52, 139.74, 145.62, 167.58; MALDI-TOF MS: Calculated *m*/*z* for $C_{114}H_{180}N_2O_8$: 1705.70, found: 1705.16.

2.5.2. Electronic Spectral Measurements

A Shimadzu UV-3101 PC NIR scanning spectrophotometer was used to record the electronic absorption spectra. The emission spectra were recorded on a SPEXFluorolog FL-1039 spectrofluorimeter. All optical measurements were carried out using 1 mm cuvettes with a thermistor directly attached to the wall of the cuvette holder for controlling the temperature.

2.5.3. Gelation Studies

The compound to be studied was taken in a sealed glass vial with known volume of solvent. The glass vial was heated until the compound was dissolved. Gel formation occurred when the hot solution was allowed to cool and was confirmed by the incapability of the content to flow by inverting the glass vial. Repeated heating and cooling of the solution confirmed the thermal reversibility of the supramolecular gel. Gel melting temperature (T_{gel}) was determined by the dropping ball method.[53]

2.5.4. Rheology Measurements

The rheological properties of the **OPVA** and the hybrid gels with C_{60} were measured using a Physica Modular Compact (MCR 150) stress controlled rheometer from Anton Paar with a Cone-and-plate geometry (CP 50-1). A Parallel plate sensor having a 50 mm diameter was used maintaining a gap size of 0.1 mm. Gels in toluene were transferred to the peltier and plate was covered properly to avoid the solvent evaporation. Dynamic oscillatory mode was used for the measurements keeping constant strain amplitude (γ) of 1% and the angular frequency was varied from 1-100 $rads^{-1}$.

2.5.5. Morphological Analysis

AFM images were recoded under ambient conditions using a NTEGRA (NT-MDT) operating with a tapping mode regime. Micro-fabricated TiN cantilever tips (NSG10) with a resonance frequency of 299 kHz and a spring constant of 20 - 80 Nm^{-1} were used. AFM section analysis was done offline. Samples for the imaging were prepared

by drop casting toluene solution of **OPVA**, C_{60} and **OPVA**/C_{60} on to a freshly cleaved mica sheet at the required concentrations at ambient conditions and dried under vacuum. TEM measurements were carried out using FEI (TECNAI G2 30 S-TWIN) with an accelerating voltage of 100 kV. Samples were prepared by drop casting toluene solutions of **OPVA**, C_{60} and **OPVA**/C_{60} on to carbon coated copper grids at the required concentrations at ambient conditions. The samples were dried under vacuum. TEM images were obtained without staining. Inverse FFT reconstruction of the HR-TEM images was done using a software program, Digital MicrographTM (GATAN Inc.) following a reported procedure.[67] FFT of the experimentally obtained image was initially taken followed by appropriate mask filtering to remove the spatial frequency of the diffractogram. Finally, the Inverse FFT gave rise to a reconstructed HR-TEM image. SEM images were obtained from a Zeiss EVO 18 cryo-SEM Special Edn with variable pressure detector working at 20-30 kV. Samples were prepared from toluene solutions of appropriate concentration by drop casting onto freshly cleaved mica surface.

2.5.6. X-ray Diffraction (XRD) Analysis

Samples for the XRD studies were prepared by transferring respective gels onto aluminum foil and dried slowly to evaporate the solvent. Finally, all samples were kept under vacuum to ensure complete removal of solvent. X-ray diffractogram of the dried films were recorded on XEUSS SAXS/WAXS system using a Genix microsource from Xenocs operated at 50 kV and 0.6 mA. The Cu Kα radiation (λ = 1.54 Å) was collimated with FOX2D mirror and two pairs of scatter less slits from

Xenocs. The two-dimensional patterns were recorded on a Mar345 image plate and processed using Fit2D software. All the measurements were made in the transmission mode. The sample to detector distance was calibrated with silver behenate standard and it was found to be 214.5 mm. Deconvolution of XRD data was performed using Fityk 0.9.8 software.[68]

2.5.7. Flash-Photolysis Time Resolved Microwave Conductivity (FP-TRMC) Studies

Third harmonic generation (355 nm) of a Nd:YAG laser (5-8 ns pulse duration, Spectra Physics GCR-130, incident photon density to a sample was set to 9.1×10^{15} cm^{-2}) was used as an excitation source for TRMC. The transient photoconductivity ($\Delta\sigma$) was measured by TRMC using 3 mW X-band (~ 9.1 GHz) microwave. The obtained transient photoconductivity ($\Delta\sigma$) was converted to the product of the quantum yield (φ) and the sum of charge carrier mobilities: ($\Sigma\mu = \mu_+ + \mu_-$), by $\varphi\Sigma\mu = \Delta\sigma\ (eI_0F_{light})^{-1}$, where e, I_0, and F_{light} are the unit charge of a single electron, incident photon density of excitation laser (in m^{-2}), a correction (or filling) factor (in m^{-1}), respectively. The F_{light} was calculated by taking into consideration the geometry and optical properties of the sample such as the size, laser cross-section, and absorption of the excitation laser. The details of the system were reported previously.[63]All experiments were carried out at room temperature. Samples were prepared by drop casting toluene solutions of **OPVA** and **OPVA**/C_{60} on a quartz plates and thereby drying under vacuum.

2.5.8. Photocurrent Measurements

Devices for photocurrent measurement were fabricated on OFET platform with Bottom gate/bottom contact (BG/BC) configuration. For gate electrode and gate dielectric layer a heavily doped *n*-type Si wafer and dry oxidized SiO_2 were used, respectively (capacitance of 11 $nFcm^{-2}$).[69] Thickness of the dielectric was 300 nm with surface roughness less than 0.1 nm. Gold electrodes were used as both source and drain. Photolithography technique has been used to deposit gold electrodes. After sequential washing with water, deionized water and ethanol, substrates were rinsed with acetone. Surface modification of all substrates was done with *n*-trichloro(octadecyl)silane followed by cleaning with *n*-hexane, $CHCl_3$ and acetone. The system was kept in vacuum for 60 min and the substrates were washed with ethanol. **OPVA**, **OPVA**/C_{60}, *n*-**DA** and *n*-**DA**/C_{60} were dissolved in toluene, heated and cooled to obtain a gel in individual cases. The gels were further diluted with toluene and spin-coated over the above mentioned modified silicon substrate at 2000 rpm for 30 s. Samples were kept at vacuum for overnight at room temperature to ensure complete removal of the solvent. Photocurrent measurement of the devices was carried in ambient conditions, using a Keithley Model 4200 SCS semiconductor parameter analyzer.

2.6. References

1. Kumar, D. K., Steed, J. W. *Chem. Soc. Rev*. **2014**, *43*, 2080-2088.
2. Mattia, E., Otto, S. *Nature Nanotech*. **2015**, *10*, 111-119.

3. Korevaar, P. A., George, S. J., Markvoort, A. J., Smulders, M. M. J., Hilbers, P. A. J., Schenning, A. P. H. J., De Greef, T. F. A., Meijer, E. W. *Nature* **2012**, *481*, 492-496.
4. Aida, T., Meijer, E. W., Stupp, S. I. *Science* **2012**, *335*, 813-817.
5. Li, J.-L., Liu, X.-Y. *Adv. Funct. Mater*. **2010**, *20*, 3196-3216.
6. Li, J. L., Liu, X. Y. Soft Fibrillar Materials: Fabrication and Applications (Wiley-VCH, Weinheim, Germany, **2013**), pp. 1961-2007.
7. Garti, N., Yuli, I. A. Nanotechnologies for Solubilization and Delivery in Foods, Cosmetics and Pharmaceuticals (DEStech Publications, Inc, Pennsylvania, U.S. A., **2012**), pp. 284-287.
8. Mukhopadhyay, R. D., Praveen, V. K., Hazra, A., Maji, T. K., Ajayaghosh, A. *Chem. Sci*. **2015**, *6*, 6583-6591.
9. Foster, J. A., Piepenbrock, M.-O. M., Lloyd, G. O., Clarke, N., Howard, J. A. K., Steed, J. W. *Nat. Chem*. **2010**, *2*, 1037-1043.
10. Yaghi, O. M., Li, G., Li, H. *Chem. Mater*. **1997**, *9*, 1074-1076.
11. Liesegang, R. E., Naturwiss. Wochenschr., **1896**, *11*, 353-362.
12. Petrova, R. I., Patel, R., Swift, J. A. *Cryst. Growth Des*. **2006**, *6*, 2709-2715.
13. Li, H., Fujiki, Y., Sada, K., Estroff, L. A. *CrystEngComm* **2011**, *13*, 1060-1062.
14. Safont-Sempere, M. M., Fernández, G., Würthner, F. *Chem. Rev*. **2011**, *111*, 5784-5814.
15. Charvet, R., Yamamoto, Y., Sasaki, T., Kim, J., Kato, K., Takata, M., Saeki, A., Seki, S., Aida, T. *J. Am. Chem. Soc*. **2012**, *134*, 2524-2527.
16. Tevis, I. D., Tsai, W.-W., Palmer, L. C., Aytun, T., Stupp, S. I. *ACS Nano* **2012**, *6*, 2032-2040.

17. Babu, S. S., Praveen, V. K., Ajayaghosh, A. *Chem. Rev*. **2014**, *114*, 1973-2129.

18. Praveen, V. K., Ranjith, C., Bandini, E., Ajayaghosh, A., Armaroli, N. *Chem. Soc. Rev*. **2014**, *43*, 4222-4242.

19. Yagai, S., Okamura, S., Nakano, Y., Yamauchi, M., Kishikawa, K., Karatsu, T., Kitamura, A., Ueno, A., Kuzuhara, D., Yamada, H., Seki, T., Ito, H. *Nat. Commun*. **2014**, *5*, 4013.

20. Li, Z., Liu, Z., Sun, H., Gao, C. *Chem. Rev*. **2015**, *115*, 7046-7117.

21. Accorsi, G., Armaroli, N. *J. Phys. Chem. C* **2010**, *114*, 1385-1403.

22. Guldi, D. M., Illescas, B. M., Atienza, C. M., Wielopolski, M., Martín, N. *Chem. Soc. Rev*. **2009**, *38*, 1587-1597.

23. Srinivasan, S., Babu, S. S., Praveen, V. K., Ajayaghosh, A. *Angew. Chem. Int. Ed*. **2008**, *47*, 5746-5749.

24. Samanta, S. K., Subrahmanyam, K. S., Bhattacharya, S., Rao, C. N. *Chem. Eur. J*. **2012**, *18*, 2890-2901.

25. Charvet, R., Acharya, S., Hill, J.P., Akada, M., Liao, M., Seki, S., Honsho, Y., Saeki, A., Ariga, K. *J. Am. Chem. Soc*. **2009**, *131*, 18030-18031.

26. Insuasty, A., Atienza, C., López, J. L., Martínez, J. M., Casado, S., Saha, A., Guldi, D. M., Martín, N. *Sci. Rep*. **2015**, *5*, 14154.

27. Li, W.-S., Yamamoto, Y., Fukushima, T., Saeki, A., Seki, S., Tagawa, S., Masunaga, H., Sasaki, S., Takata, M., Aida, T. *J. Am. Chem. Soc*. **2008**, *130*, 8886-8887.

28. López-Andarias, J., López, J. L., Atienza, C., Brunetti, F. G., Romero-Nieto, C., Guldi, D. M., Martín, N. *Nat. Commun*. **2014**, *5*, 3763.

29. Sathish, M., Miyazawa, K., Hill, J. P., Ariga, K. *J. Am. Chem. Soc*. **2009**, *131*, 6372-6373.

30. Babu, S. S., Möhwald, H., Nakanishi, T. *Chem. Soc. Rev*. **2010**, *39*, 4021-4035.

31. Michinobu, T., Nakanishi, T., Hill, J. P., Funahashi, M., Ariga, K. *J. Am. Chem. Soc*. **2006**, *128*, 10384-10385.

32. Shrestha, L. K., Ji, Q., Mori, T., Miyazawa, K., Yamauchi, Y., Hill, J. P., Ariga, K. *Chem. Asian J*. **2013**, *8*, 1662-1679.

33. Bonifazi, D., Enger, O., Diederich, F. *Chem. Soc. Rev*. **2007**, *36*, 390-414.

34. Park, C., Song, H. J., Choi. H. C. *Chem. Commun*. **2009**, 4803-4805.

35. Lebedeva, M. A., Chamberlain, T. W., Khlobystov, A. N. *Chem. Rev*. **2015**, *115*, 11301-11351.

36. Iwasa, Y. *Nature* **2010**, *466*, 191-192.

37. Barnes, J. C., Dale, E. J., Prokofjevs, A., Narayanan, A., Gibbs-Hall, I. C., Juríček, M., Stern, C. L., Sarjeant, A. A., Botros, Y.Y., Stupp, S. I., Stoddart, J. F. *J. Am. Chem. Soc*. **2015**, *137*, 2392-2399.

38. Yamamoto, Y., Zhang, G., Jin, W., Fukushima, T., Ishii, N., Saeki, A., Seki, S., Tagawa, S., Minari, T., Tsukagoshi, K., Aida, T. *Proc. Natl. Acad. Sci. USA* **2009**, *106*, 21051-21056.

39. Nurmawati, M. H., Ajikumar, P. K., Renu, R., Sow, C. H., Valiyaveettil, S. *ACS Nano* **2008**, *2*, 1429-1436.

40. Hollamby, M. J., Karny, M., Bomans, P. H. H., Sommerdjik, N. A. J. M., Saeki, A., Seki, S., Minamikawa, H., Grillo, I., Pauw, B. R., Brown, P., Eastoe, J., Möhwald, H., Nakanishi, T. *Nat. Chem*. **2014**, *6*, 690-696.

41. Nair, V. S., Pareek, Y., Karunakaran, V., Ravikanth, M., Ajayaghosh, A. *Phys. Chem. Chem. Phys*. **2014**, *16*, 10149-10156.

42. Segura, J. L., Martín, N., Guldi, D. M. *Chem. Soc. Rev*. **2005**, *34*, 31-47.

43. Xue, P., Wang, P., Yao, B., Sun, J., Gong, P., Zhang, Z., Qian, C., Lu, R. *ACS Appl. Mater. Interfaces* **2014**, *6*, 21426-21434.

44. Xue, P., Wang, P., Yao, B., Sun, J., Gong, P., Zhang, Z., Lu, R. *RSC Adv*. **2015**, *5*, 75425-75433.

45. Zhang, C., Wang, J., Wang, J.-J., Li, M., Yang, X.-L., Xu, H.-B. *Chem. Eur. J*. **2012**, *18*, 14954-14956.

46. Hasobe, T., Sandanayaka, A. S. D., Wada T., Araki, Y. *Chem. Commun*. **2008**, 3372-3374.

47. Xue, P., Lu, R., Zhao, L., Xu, D., Zhang, X., Li, K., Song, Z., Yang, X., Takafuji, M., Ihara, H. *Langmuir* **2010**, *26*, 6669-6675.

48. Yang, X., Zhang, G., Zhang, D., Zhu, D. *Langmuir* **2010**, *26*, 11720-11725.

49. Daiguebonne, C., Deluzet, A., Camara, M., Boubekeur, K., Audebrand, N., Gérault, Y., Baux, C., Guillou, O. *Cryst. Growth Des*. **2003**, *3*, 1015-1020.

50. Buendía, J., Matesanz, E., Smith, D. K., Sánchez, L. *CrystEngComm* **2015**, *17*, 8146-8152.

51. George, S. J., Ajayaghosh, A. *J. Am. Chem. Soc.* **2001**, *123*, 5148-5149.

52. Piepenbrock, M.-O. M., Lloyd, G. O., Clarke, N., Steed, J. W. *Chem. Rev*. **2010**, *110*, 1960-2004.

53. Babu, S. S., Praveen, V. K., Kartha, K. K., Mahesh, S., Ajayaghosh, A. *Chem. Asian J*. **2014**, *9*, 1830-1840.

54. Eckert, J.-F., Nicoud, J.-F., Nierengarten, J.-F., Liu, S.-G., Echegoyen, L., Barigelletti, F., Armaroli, N., Ouali, L., Krasnikov, V., Hadziioannou, G. *J. Am. Chem. Soc*. **2000**, *122*, 7467-7479.

55. Goel, A., Howard, J. B., Sande, J. B. V. *Carbon* **2004**, *42*, 1907-1915.

56. Stephens, P. W., Mihaly, L., Lee, P. L., Whetten, R. L., Huang, S.-M., Kaner, R., Deiderich, F., Holczer, K. *Nature* **1991**, *351*, 632-634.

57. Krätschmer, W., Lamb, L. D., Fostiropoulos, K., Huffman, D. R. *Nature* **1990**, *347*, 354-358.

58. Ji, H. X., Hu, J. S., Wan, L. J., Tang, Q. X., Hu, W.-P. *J. Mater. Chem*. **2008**, *18*, 328-332.

59. Kuduva, S. S., Blaser, D., Boese, R., Desiraju, G. R. *J. Org. Chem*. **2001**, *66*, 1621-1626.

60. Chopra, D., Row, T. N. G. *CrystEngComm* **2008**, *10*, 54-67.

61. Wasserman, H. J., Ryan, R. R., Layne, S. P. *Acta Cryst*. **1985**, C41, 783-785.

62. Saeki, A., Koizumi, Y., Aida, T., Seki, S. *Acc. Chem. Res*. **2012**, *45*, 1193-1202.

63. Seki, S., Saeki, A., Sakurai, T., Sakamaki, D. *Phys. Chem. Chem. Phys*. **2014**, *16*, 11093-11113.

64. Prasanthkumar, S., Ghosh, S., Nair, V. C., Saeki, A., Seki, S., Ajayaghosh, A. *Angew. Chem. Int. Ed*. **2015**, *54*, 946-950.

65. Zhang, Y., Liu, W., Jiang, L., Fan, L., Wang, C., Hu, W., Zhong, H., Li, Y., Yang, S. *J. Mater. Chem*. **2010**, *20*, 953-956.

66. Meshot, E. R., Patel, K. D., Tawfick, S., Juggernauth, K. A., Bedewy, M., Verploegen, E. A., De Volder, M. F. L., Hart, A. J. *Adv. Funct. Mater*. **2012**, *22*, 577-584.

67. Kim, Y.-M., Jeong, J.-M., Kim, J.-G., Kim, Y.-J. *J. Korean Phys. Soc*. **2006**, *48*, 250-255.

68. Wojdyr, M. *J. Appl. Cryst*. **2010**, 43, 1126-1128.

69. Cai, Z., Luo, H., Qi, P., Wang, J., Zhang, G., Liu, Z., Zhang, D. *Macromolecules* **2014**, *47*, 2899-2906.

Chapter 3

Role of Pyridine-Carboxylic Acid Interaction on Morphology and Charge Carrier Properties of a Two-Component π-Gel System

3.1. Abstract

*Multicomponent supramolecular gels can show mixed or self-sorted molecular assemblies depending on the nature of the binding motifs in the assembling units. In this chapter, we describe mixed assembly (co-assembly) of a pyridine functionalized oligo(p-phenylenevinylene) (**OPV-P**) and an acid functionalized perylenebisimide (**PBI-A**) system. The key role of hydrogen bonding between carboxylic acid and pyridine functionalities on the molecular co-assembly and its functional properties has been studied in detail. The two-component gel of **OPV-P** and **PBI-A** showed better thermal and mechanical stability, when compared to the bare **OPV-P** gel. Temperature dependent spectral studies highlight the difference in the supramolecular polymerization mechanism of the described two-component system. Morphological investigations revealed that co-assembly of **OPV-P** and **PBI-A** leads to distinct nanoscopic features, which is quite different from the self-assembled structures obtained from the individual components. Charge carrier transport properties of the co-assembled nanostructures are studied using four-probe conductivity method and conductive atomic force microscopic (C-AFM) technique. Two model derivatives, oligo(p-phenylenevinylene)(**OPV-B**) and perylenebisimide*

(PBI-B) *were used to study the role of the end functionalities in the co-assembly process and the properties of the obtained structures.*

3.2. Introduction

Functional properties of the supramolecular assembly can be controlled by integrating various non-covalent interactions in the assembling medium. Mixing of more than one supramolecular component is one of the facile ways and may be the mostly adapted method in this regard.[1,2] In a multicomponent system, molecules with mutually interacting binding motifs prefer to form mixed assembly or co-assembly to attain interesting properties which cannot be obtained from individual components.[3-10] Molecules with non-interacting binding motifs tend to self-sort, where each components independently form self-assembled nanostructures (Scheme 3.1).[11,12, 13-17]

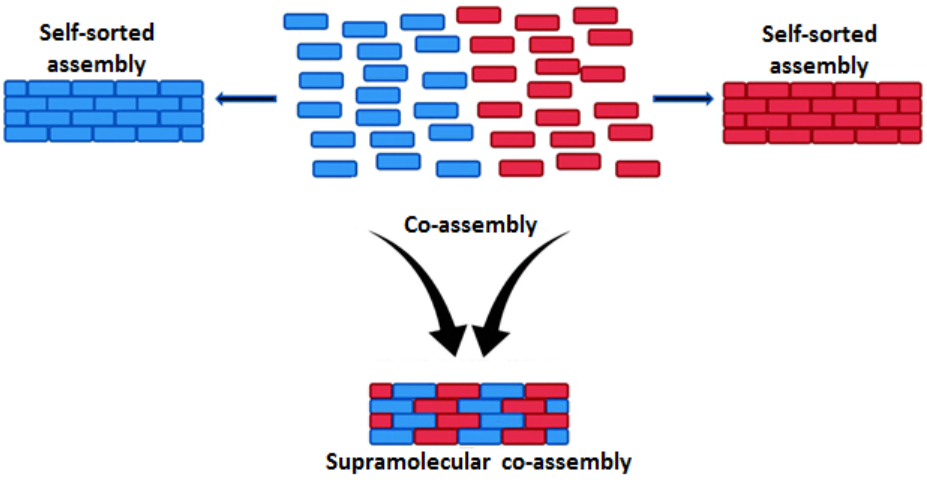

Scheme 3.1. Schematic representation of different types of multicomponent molecular assembly.

However, for most of the multicomponent π-conjugated systems, it is difficult to predict and control the outcome of the molecular assembly since it is affected by various external as well as internal factors.[12,18] Supramolecular forces such as hydrogen bonding,[19-21] metal-ligand interactions,[22-24] electrostatic interactions,[11] π-π-stacking[25] and solvophobic effects[26,27] can influence the aggregation behaviour of multicomponent systems. Therefore, proper manipulation of these intermolecular forces can determine the nature and outcome of the aggregation processes in the multicomponent supramolecular systems.

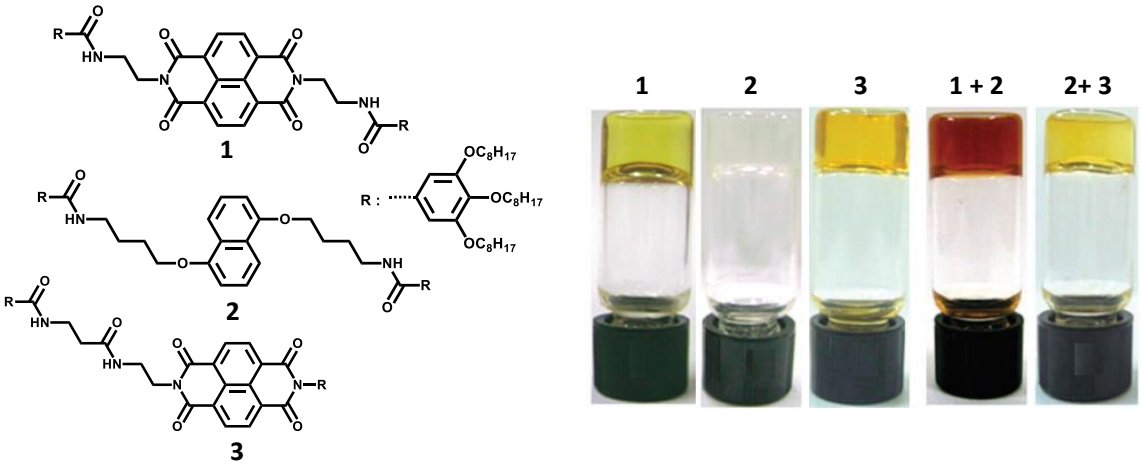

Figure 3.1. Structure of a few amide-functionalized chromophores and photographs of individual and composite gels in methyl cyclohexane.

Symmetry of the hydrogen bonding functionalities on the π-conjugated chromophores has a vital role in determining the molecular aggregation mechanism in the multicomponent system.[28] Naphthalene diimide acceptor (**1**) forms hydrogen bond mediated co-assembly with anthracene based donor (**2**) whereas its structural isomer (**3**) prefers self-sorted molecular assembly with **2**. Two amide functionalities placed symmetrically on the molecule **1** facilitates charge transfer (CT) complex formation

with **2,** due to the geometrically favoured hydrogen bonding. However, in the case of **3**, hydrogen bonding moieties are placed only on one side of the chromophore which leads to the self-sorted assembly in the mixture of **2** and **3** (Figure 3.1).

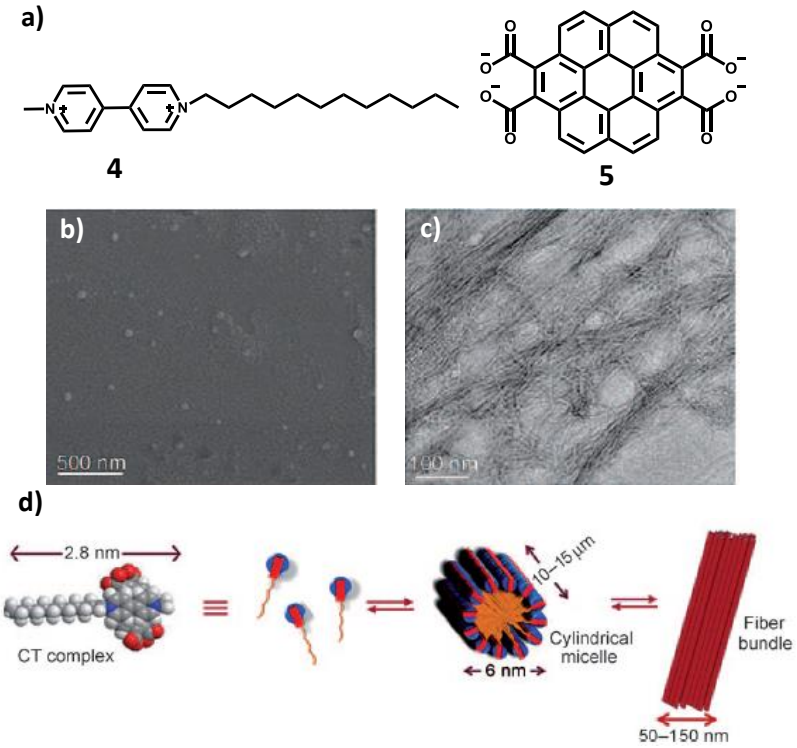

Figure 3.2. a) Molecular structures of **4** and **5**, b) spherical objects formed from **4** in water, c) 1D nanofibers from **4**:**5** complex (1:1) and d) schematic representation of the hierarchical self-assembly of the **4**:**5** CT amphiphile into cylindrical micelles and fiber bundles.

George et al. have reported donor-acceptor co-assembly using a combination of *π*-*π* stacking, charge-transfer and electrostatic interactions.[29] The alkylated methyl viologen (**4**) self-assembles in water to form spherical nanostructures. However, this molecular assembly is quite dynamic in nature to reorganize upon addition of the coronene salt (**5**). Co-assembly of both components leads to the formation of CT complexes having one dimensional (1D) bilayer-type packing of donor-acceptor units

along the π-π stacking direction of the chromophores. Hence, the formed long cylindrical micelles further aggregate to form larger fiber bundles and eventually result in the hydrogel formation (Figure 3.2).

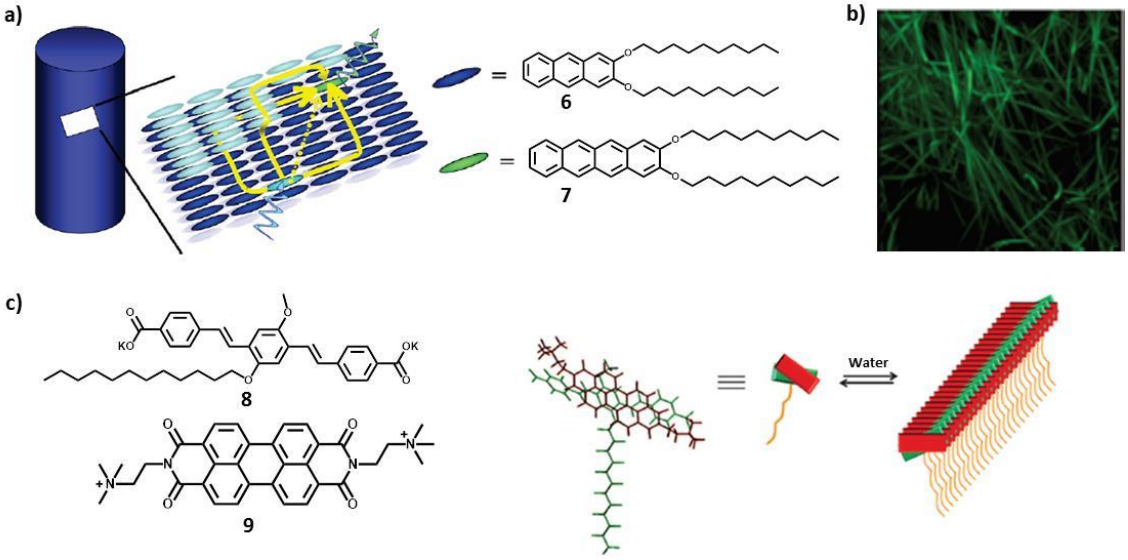

Figure 3.3. a) Schematic representation of co-assembly and energy transfer processes between **6** and **7**. b) Fluorescence confocal microscopy image of co-assembled gel from **6** and **7** in DMSO. c) Molecular structures of amphiphilic chromophores (**8** and **9**) and schematic representation of the mixed assembly.

Foster et al. have demonstrated the effect of spacer length on the multicomponent assembly of bisurea based gelators.[30] Gelators with same alkyl chain length form mixed assembly leading to distinct fiber morphology, which is quite different from the nanoscopic morphology of the individual components. Structural similarities of the aromatic cores can leads to the mixed assembly of π-conjugated chromophores, which can be used as an active medium for the efficient energy transfer process (Figure 3.3).[31] Gel fibers of dialkoxy anthracene (**6**) is incorporated

with tetracene derivative (**7**) due to the strong π-π stacking interactions between the planar aromatic cores. Rigid supramolecular packing in the mixed molecular assembly provides multiple pathways for the exciton migration, which favorably influence the energy migration process from anthracene to tetracene upon photoexcitation. George et al. have reported a conducting supramolecular co-assembly from extended π-conjugated donor and acceptor molecules.[32] Dynamic aggregation of individual donor (**8**) and acceptor (**9**) molecules is agitated by the mutual non-covalent amphiphilic interactions, which eventually leads to co-facial organization of **8** and **9** (Figure 3.3). The formed nanotubes laterally interact through coulombic interaction to form fiber bundles which exhibited conductivity even without external doping.

Synthon approach involving acid-pyridine interaction has extensively used in the engineering of multicomponent supramolecular systems.[33,34] Shinkai et al. have demonstrated the formation of size tunable supramolecular aggregates using the complementary hydrogen bonding between carboxylic acid and pyridine functionalities.[35] The block copolymer (**10**) having pyridine groups co-assemble with fullerene carboxylic acid (**11**) (Figure 3.4). Relative ratio of the pyridine content in the block copolymer influences the extent of acid-pyridine interaction and hence the size of the co-assembled supramolecular nanostructures. Liu et al. have extensively used acid-pyridine interaction to construct multicomponent donor-acceptor gel. These hydrogen bonded donor-acceptor complex assemble into 1D nanofibers with closely connected *p*- and *n*- channels having excellent photocurrent generation properties.[36-38]

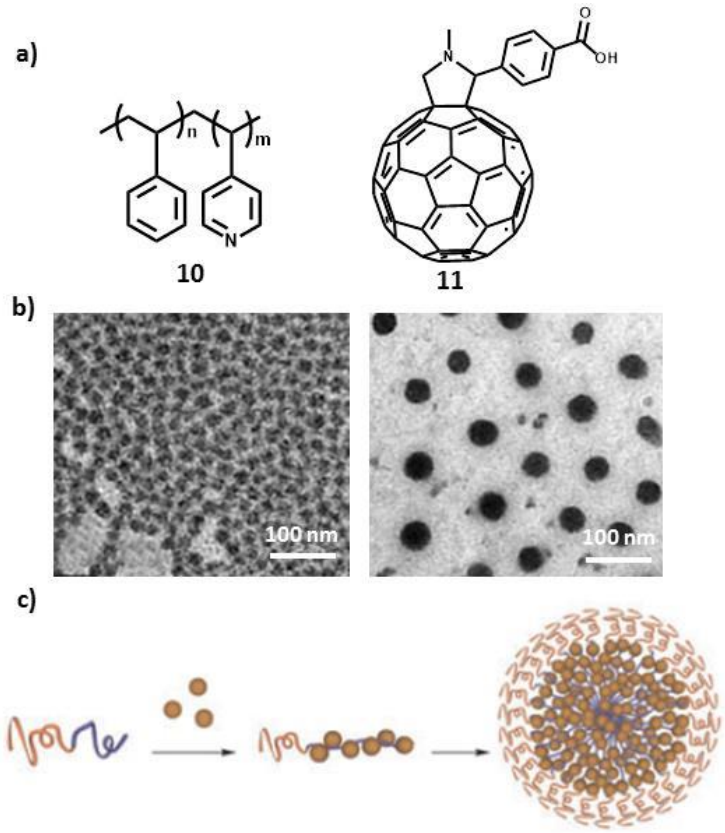

Figure 3.4. a) Molecular structures of a block copolymer **10** and a fullerene adduct **11**. b) TEM images of composites showing nanoparticles of different sizes. c) Schematic representation of the formation of spherical nanoparticles.

Multicomponent molecular assembly based on π-conjugated donor-acceptor systems are well studied, especially chromophores based on oligo(*p*-phenylenevinylene) (OPV) and perylenebisimide (PBI).[39-41] In order to gain control over the functional properties of these multicomponent systems, it is important to unravel the aggregation behaviour of the individual molecules and the reasons that lead these molecules to select a specific partner from the multicomponent mixture. Functional group engineering is one of the commonly used strategy to control the

nature of the multicomponent assemby.[29,42,43] Complementary nature of carboxylic acid and pyridine functional groups is well exploited in crystal engineering but its impact on the gel chemistry of π-conjugated chromophores is yet to be studied in depth.

In this chapter, we discuss the role of acid-pyridine interaction in the bicomponent assembly of pyridine functionalized oligo(*p*-phenylenevinylene) (**OPV-P**) and carboxylic acid functionalized perylenebisimide (**PBI-A**) (Scheme 3.2). In order to compromise the solubility of the **PBI-A**, we have used toluene/THF (in 9:1 v/v) mixture as solvent. **OPV-P** is a good organogelator and retains its gelation ability after mixing with **PBI-A** (Figure 3.5). The benzene functionalized oligo(*p*-phenylenevinylene) (**OPV-B**) and perylenebisimide (**PBI-B**) are used for comparative studies.

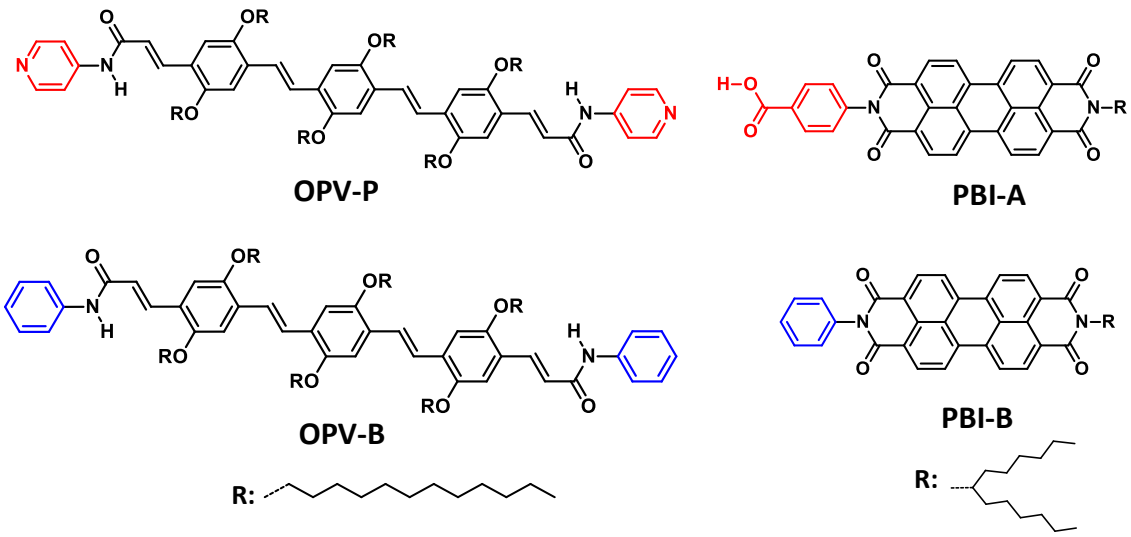

Scheme 3.2. Chemical structures of molecules used in this work.

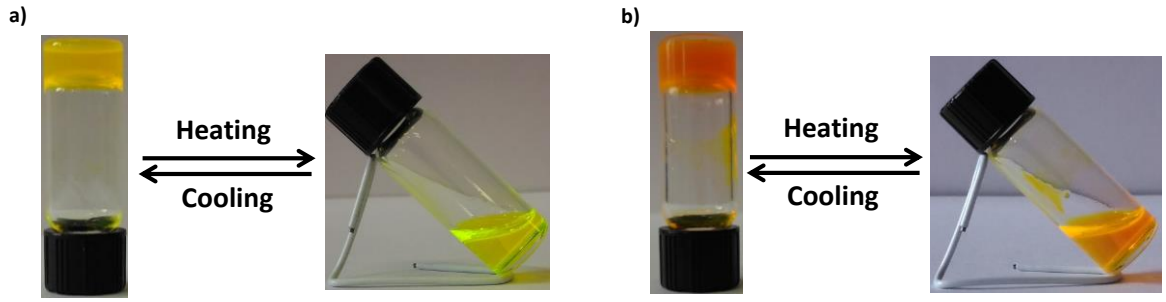

Figure 3.5. Photographs a) **OPV-P** gel and b) composite gel of **OPV-P** and **PBI-A** at a ratio of 1:2 in toluene/THF (1:9), during heating and cooling.

3.3. Results and Discussion

3.3.1. The Design Strategy

OPV-P and **OPV-B** were synthesized from the OPV bisacid (**OPV-3**) as shown in Scheme 3.3. The OPV bisester (**OPV-2**) was synthesized from OPV aldehyde (**OPV-1**) as per a reported procedure.[44] Alkaline hydrolysis of **OPV-2** produced OPV bisacid (**OPV-3**). 4-Amino pyridine and aniline were used in the final coupling reaction with **OPV-3** for the preparation of **OPV-P** and **OPV-B**, respectively.

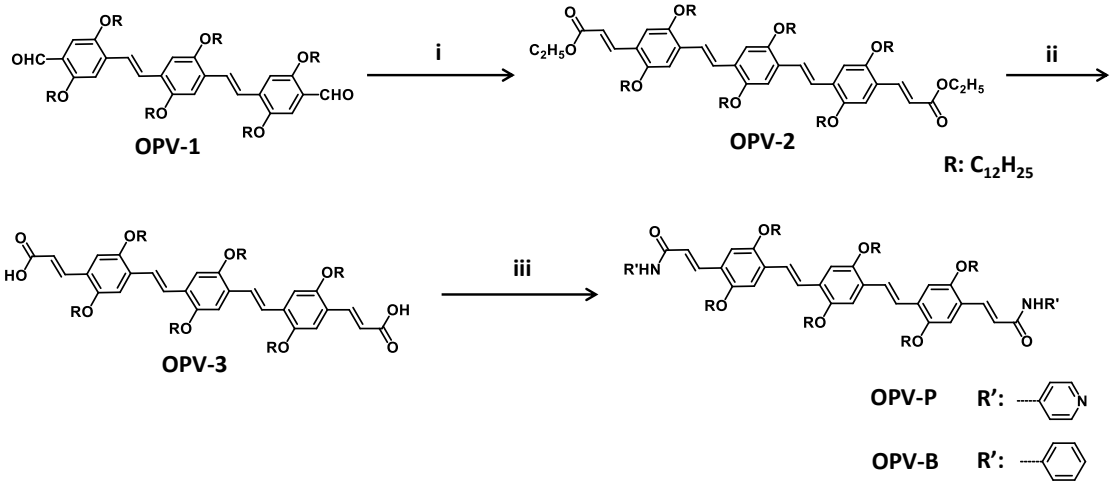

Scheme 3.3. Reagents and conditions: (i) **12**, NaH, dry THF, 60 °C, 5 h; (ii) KOH, methanol/THF, 60 °C, 4 h; (iii) $R'NH_2$, HATU, DiPEA, dry CH_2Cl_2, 0 - 25 °C, 8 h.

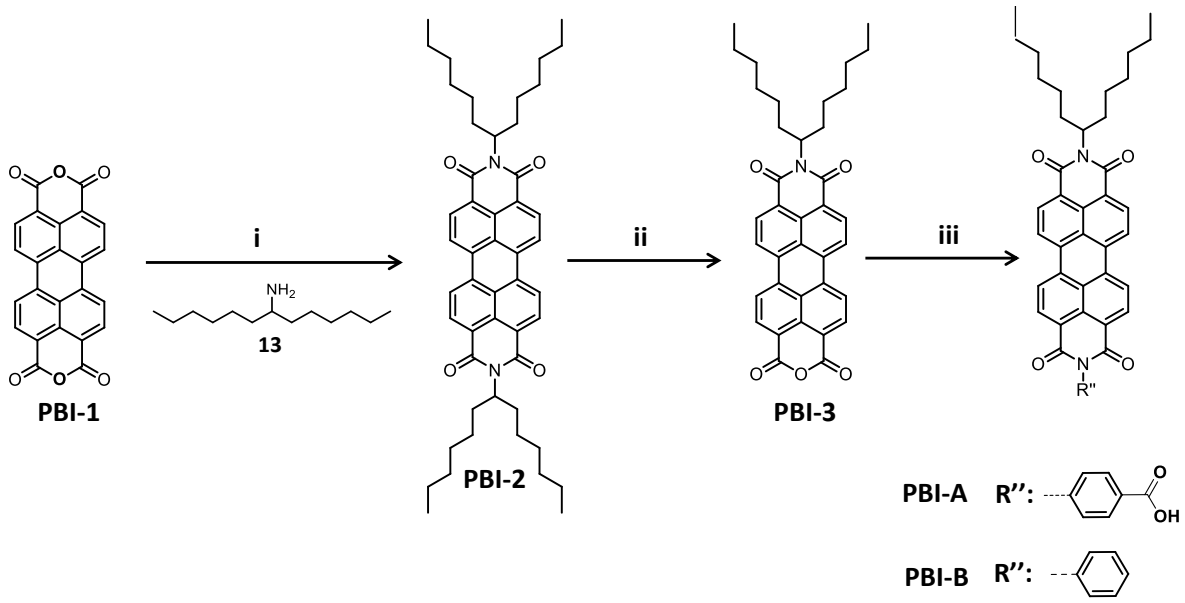

Scheme 3.4. Reagents and conditions: (i) 1-hexylheptylamine, $Zn(OAc)_2$, imidazole, 110 °C; (ii) KOH, *tert*-butanol;(iii) $R'NH_2$, imidazole, 110 °C.

Synthesis of PBI derivatives was started from the perylene dianhydride (**PBI-1**) (Scheme 3.4). 1-Hexylheptyl amine (**13**) was treated with **PBI-1** to get the symmetrically substituted perylene diimide (**PBI-2**), which after partial hydrolysis with potassium hydroxide in *tert*-butanol yielded the perylene monoanhydride (**PBI-3**). **PBI-3** is further treated with 4-amino benzoic acid and aniline to get the **PBI-A** and **PBI-B** respectively.[45-47]

3.3.2. Photophysical Studies

OPV-P showed an absorption band around 450 nm corresponding to π-π* transition. The emission spectrum was broad with maximum around 514 nm. Absorption spectra of **PBI-A** exhibited absorption maxima in the visible region at λ_{max} = 492 and 527

nm. **PBI-A** exhibited a structured emission spectrum with three bands at 537, 580 and 633 nm (Figure 3.6).

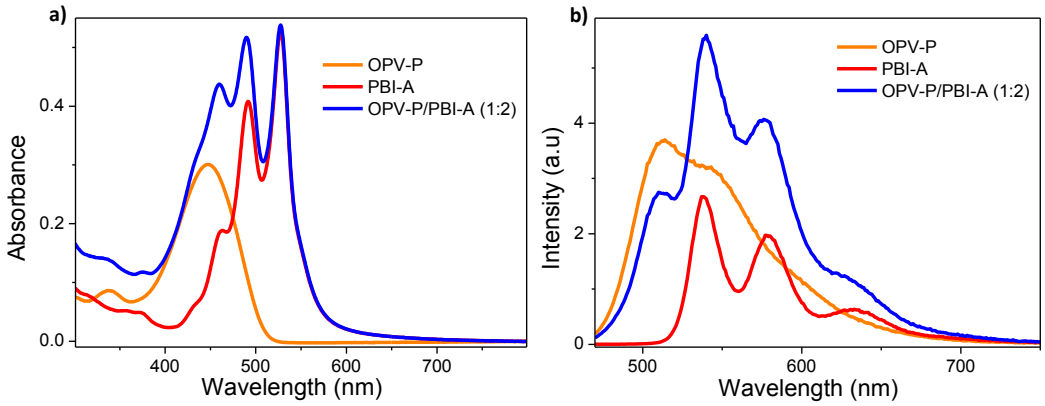

Figure 3.6. a) Absorption and b) emission spectra of **OPV-P**, **PBI-A** and mixture **OPV-P** and **PBI-A** in toluene/THF (1:9) (Concentration of **OPV-P** = 1×10^{-5} M).

Photophysical interaction between the individual components has been studied by mixing **OPV-P** and **PBI-A** at a 1:2 ratio. Absorption spectrum of the mixture was found to be the sum of the spectral features of the individual constituents. Absence of a charge transfer band indicates the absence of ground state donor-acceptor interaction between the chromophores. Emission spectrum of the mixture showed spectral features of both components showing insignificant excited state interaction between the chromophores.

The aggregation behaviour of molecules has been investigated by temperature-dependent UV-vis spectroscopic studies. Absorption spectra showed slight hypochromic effect upon cooling the **OPV-P** solution from 65 °C (Figure 3.7). From the cooling process, temperature dependent degree of aggregation (α_{agg}) is estimated using the absorption coefficient at to $\lambda = 450$ nm.[48]

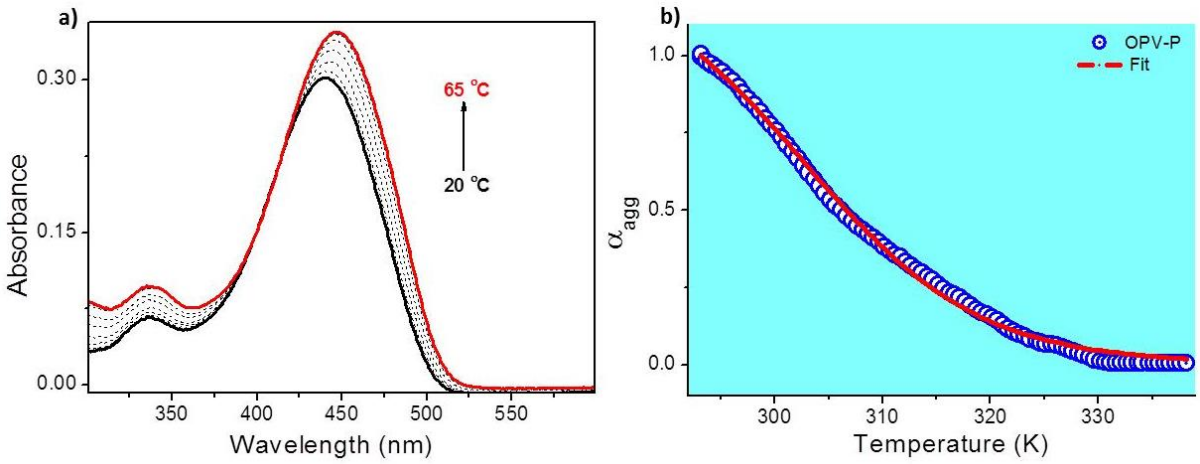

Figure 3.7. a) Temperature dependent absorption spectra of **OPV-P** in toluene/THF (1:9) between 20 - 65 °C. b) Fitting of the fraction of aggregated species (α_{agg}) against temperature (λ = 450 nm) to the isodesmic model.

It is observed that supramolecular aggregation of **OPV-P** follows a sigmoidal or isodesmic pathway in which the binding constant for each addition of monomer to the growing assembly is the same (Figure 3.7b). Thermodynamic parameters are calculated by using standard isodesmic model.[49] Molar fraction of aggregated species, α_{agg} (T) is given by the equation (1).

$$\alpha_{agg}(T) \cong \frac{1}{1+\exp\left(-0.908\Delta H\frac{T-Tm}{RTm^2}\right)} \qquad (1)$$

In the above equation, T_m is the melting temperature defined as the temperature for which α_{agg} = 0.5 and ΔH is the molar enthalpy release related to the formation of noncovalent intermolecular interactions.

Using the equation (1), molar enthalpy and entropy changes associated with the aggregation of **OPV-P** were calculated as -105.91 $kJmol^{-1}K^{-1}$ and -260 $Jmol^{-1}K^{-1}$

respectively. The number-averaged degree of polymerization (DP_N) for **OPV-P** was estimated as 2.2 which was calculated from $\alpha_{agg}(T)$ using the equation (2)

$$DP_N = \frac{1}{\sqrt{1-\alpha_{agg}(T)}} \qquad (2)$$

Equilibrium constant (K) for each addition of monomer to the supramolecular polymer is related to DP_N as shown in (3) and for **OPV-P** the value of K was found to be 1.28×10^5 M^{-1}.

$$DP_N = \frac{1}{\sqrt{1-\alpha_{agg}(T)}} = \frac{1}{2} + \frac{1}{2}\sqrt{4K_e(T)C_T + 1} \qquad (3)$$

where C_T is the total concentration of molecules.

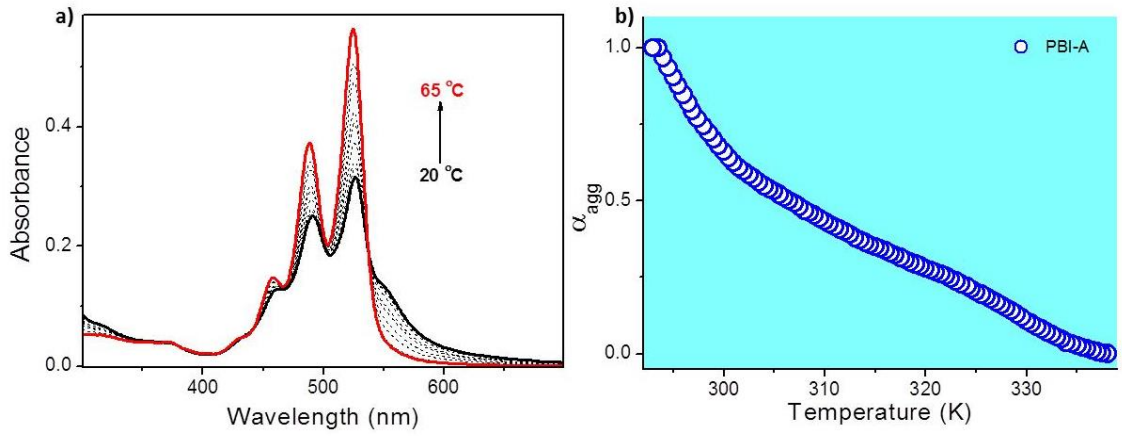

Figure 3.8. Temperature dependent absorption spectra of **PBI-A** in toluene/THF (1:9) between 20 - 65 °C. Temperature-dependent degree of aggregation **PBI-A** (α_{Agg}) calculated from the apparent absorption coefficients in the cooling processes.

Self-assembly pathway of **PBI-A** was followed by monitoring the absorption coefficient corresponding to λ = 450 nm (Figure 3.8). It is observed that the

supramolecular aggregation pathway could not be fit well with the isodesmic model as that of **OPV-P**.

Mixture of these two components exhibited a different pathway of aggregation under similar experimental conditions (Figure 3.9). It is observed that the hybrid solution followed a non-sigmoidal transition which is properly fitted using cooperative or nucleation-elongation model proposed by Meijer and co-workers.[50,51]

In the elongation regime, the fraction of aggregated molecules (α_{agg}) is defined by the following equation:

$$\alpha_{\mathrm{agg}} = \alpha_{\mathrm{SAT}}\left(1 - \exp\left[\frac{-\Delta H_e}{RT_e^2}(T - T_e)\right]\right) \qquad (4)$$

where, ΔH_e is molar enthalpy corresponding to the elongation process, T the absolute temperature, T_e the elongation temperature, R the ideal gas constant. α_{SAT} is an arbitrary parameter to ensure that $\alpha_{agg}/\alpha_{SAT}$ does not exceed unity.

From equation (4), it is found that molar enthalpy and entropy change for the elongation process are -65.92 $kJmol^{-1}K^{-1}$ and -100.2 $Jmol^{-1}K^{-1}$ respectively. By fitting the data to this model, the elongation temperature (T_e) is estimated as 334.11K.

In the nucleation regime, the fraction of aggregates (α_{agg}) is related to the dimensionless equilibrium constant (K_a) as shown in equation (5)

$$\alpha_{\mathrm{agg}} = K_a^{1/3}\exp\left[\left(2/3\,K_a^{-1/3} - 1\right)\frac{\Delta H_e}{RT_e^2}(T - T_e)\right] \qquad (5)$$

From equation (5) the value of K_a is estimated as 1.1×10^{-5}.

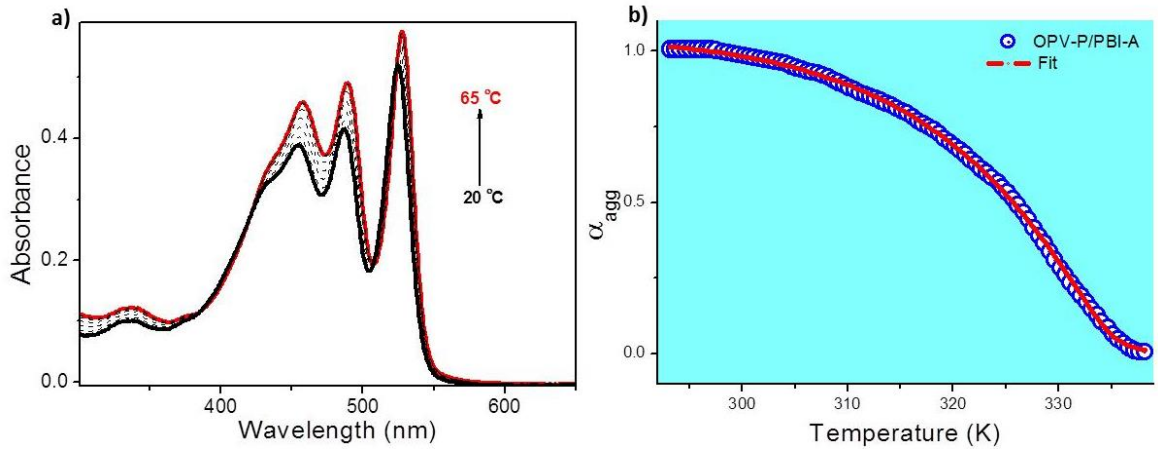

Figure 3.9. Temperature dependent absorption spectra of composite of **OPV-P** and **PBI-A** in toluene/THF (1:9) from 20 - 65 °C. Fitting of the fraction of aggregated species (α_{agg}) against temperature (λ = 450 nm) to the cooperative model.

The role of the acid-pyridine interaction in the temperature dependent supramolecular polymerization is further studied by mixing **OPV-P** with PBI benzene derivative (**PBI-B**) in 1:2 ratio. Interestingly, it is observed that aggregation mechanism of **OPV-P** does not change due to the presence of **PBI-B** (Figure 3.10). The influence of complementary acid-pyridine interaction is confirmed by comparing with a mixture of benzene functionalized oligo(*p*-phenylenevinylene) (**OPV-B**) and **PBI-A**. In contrast to **OPV-P**, **OPV-B** exhibits a co-operative model of aggregation mechanism. Nucleation-elongation mechanism of **OPV-B** was retained in the hybrid solution too (Figure 3.10). Hence, these temperature dependent absorption studies revealed the crucial role of acid-pyridine interaction in the dynamic molecular co-assembly.

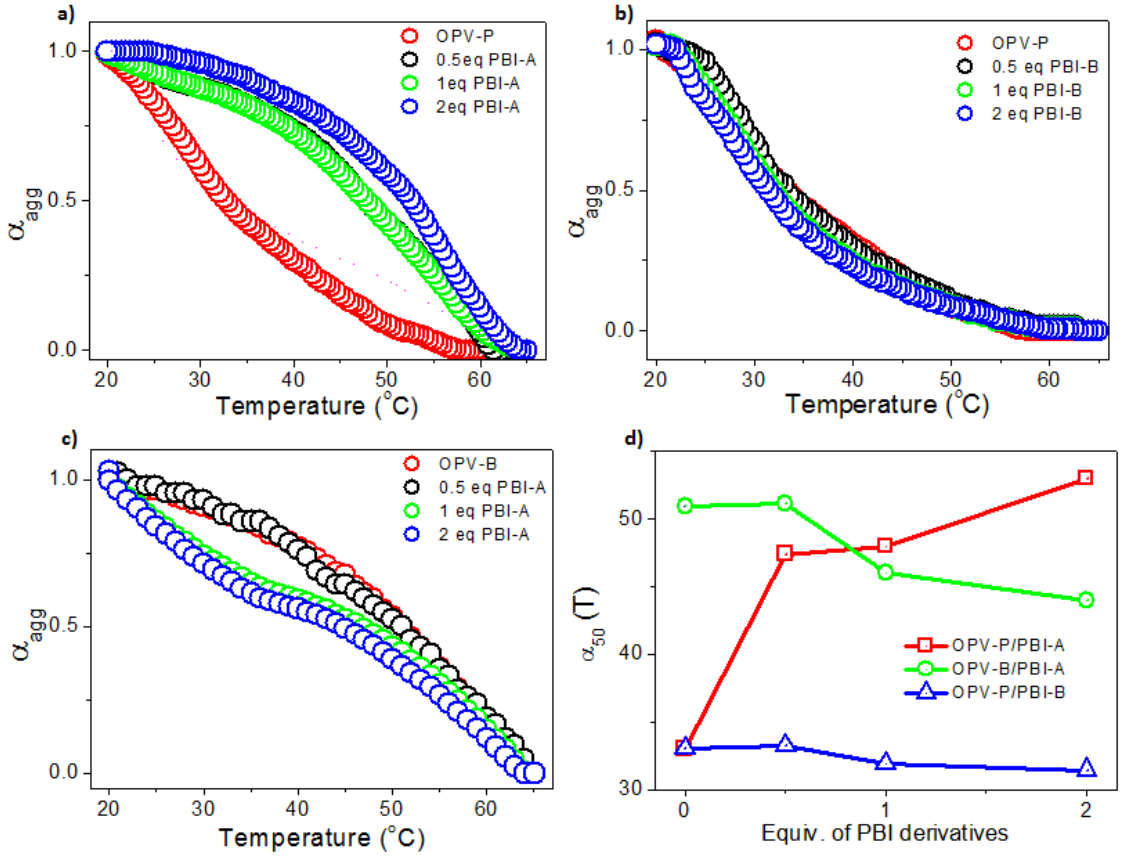

Figure 3.10. Temperature-dependent degree of aggregation, α_{agg}, calculated from the UV/Vis absorption at 450 nm for composite of a) **OPV-P**/**PBI-A**, b) **OPV-P**/**PBI-B** and c) **OPV-B**/**PBI-A**. d) Dependence of α_{50} (T) with the concentration of PBI derivatives.

Thermal stability of the supramolecular polymers can be correlated to T_m.[52-54] Temperature dependent studies proved that T_m of **OPV-P** is significantly enhanced with the addition of **PBI-A** (Figure 3.10). Neat **OPV-P** aggregates in solution exhibited T_m value of 33 °C and with gradual increase in the concentration of **PBI-A** in the composite solution, T_m rises up to 53 °C. Enhancement in the thermal stability associated with the additive concentration was absent in other mixtures where the acid-pyridine interactions are absent. **OPV-B** showed a slight decrease in the thermal

stability with respect to concentration of **PBI-A**, whereas **OPV-P** hardly showed any change in the T_m value with concentration of **PBI-B**.

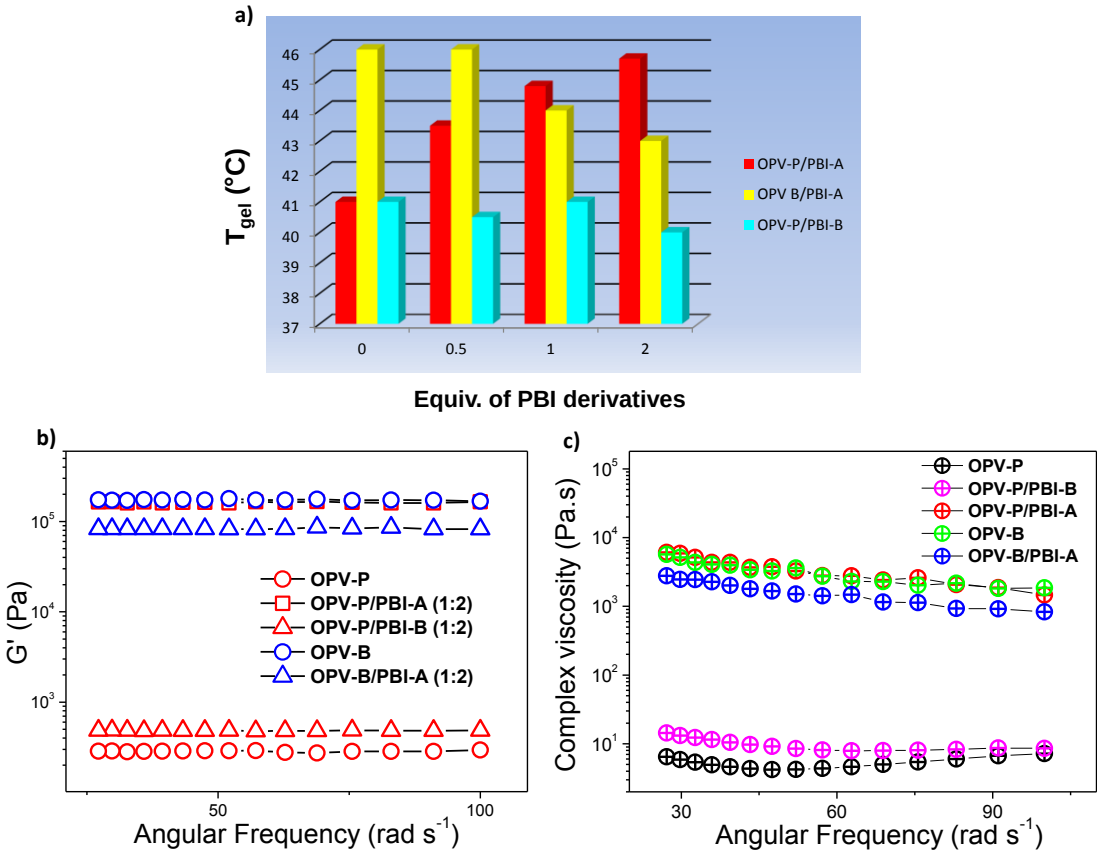

Figure 3.11. a) Plot of T_{gel} of the composite gel (0.5 mL) with increasing concentrations of PBI derivatives. Angular frequency (ω) dependencies of b) storage modulus (*G'*) and c) complex viscosity (η*) at 20 °C with strain amplitude at 0.01.

Neat and bicomponent gels have been made from respective gelator (**OPV-P** or **OPV-B**) and PBI derivatives (**PBI-A** or **PBI-B**). Concentration of the gelator was kept to 1 × 10^{-3} M in toluene/THF (v/v: 9:1). Thermo-mechanical stability of the supramolecular gel can be directly correlated with the gel melting temperature (T_{gel}).

T_{gel} is measured using the dropping ball method and it is observed that thermal stability of **OPV-P** increases with **PBI-A** concentration in the gel (Figure 3.11a). Variation of the T_{gel} values with concentration of **PBI-A** showed almost similar trend as that of T_m. Additive induced physical reinforcement was absent in other mixtures where the crucial acid-pyridine interactions were absent. So it is quite clear from these studies that acid-pyridine complementary interactions play a vital role in enhancing the thermal stability of the aggregates, which can be correlated to the efficient co-assembly in the two component system.

3.3.3. Rheological Studies

Viscoelastic nature of the molecular aggregates in the gel state is further studied using rheological experiments. It is observed that storage modulus (G'), which indicates solid like behaviour of the gel, is almost independent of the oscillation frequency. One of the other parameters extracted from the rheological studies is the complex viscosity (η*) which gives an estimate of the viscous nature or mechanical stability of the gel material. Neat **OPV-P** forms a weak gel. Storage modulus of the composite gel (**OPV-P**/**PBI-A**) was high when compared to that of **OPV-P** gel, which indicates the enhancement in the viscous nature and mechanical stability of the hybrid gel (Figure 3.11b). This was confirmed by the observation of several orders of magnitude increase in the complex viscosity of the hybrid gel when compared to the **OPV-P** gel.

Addition of **PBI-B** does not change storage modulus as well as complex viscosity of **OPV-P**, which point out the role of acid-pyridine interaction on the mechanical stability of the hybrid assembly. This is further proved by rheological

studies of the composite gel made from **OPV-B** and **PBI-A**. In contrast to **OPV-P**, **OPV-B** forms strong gel, which is clear from the viscoelastic parameters (*G′* and η*). The difference between the gelation nature of **OPV-P** and **OPV-B** may be due to the interference of the pyridine on the amide hydrogen bonding in the former gelator.[44] It is observed that the presence of **PBI-A** does not make any significant changes in the viscoelastic nature of **OPV-B** (Figure 3.11b,c). This observation indicates, the independent nature of the individual constituents in the two-component gel due to the lack of complementary interactions.

3.3.4. FT-IR Studies

The FT-IR spectra of the **OPV-P** xerogel exhibited narrow N-H stretching band at 3336 cm^{-1} indicating the presence of hydrogen bonding. **PBI-A** and composite xerogels showed broad N-H stretching bands around 3250 - 3500 cm^{-1} (Figure 3.12). Broad nature of the N-H stretching bands indicates the extensive hydrogen bonding in these samples.

Carbonyl (C=O) stretching frequency of **OPV-P** was observed at 1704 cm^{-1}. **PBI-A** and the composite xerogel showed carbonyl stretching frequency at 1711 cm^{-1} and 1728 cm^{-1} respectively. The amide H-bonding in **OPV-P** is disrupted by the pyridine moiety since pyridine-N is a strong hydrogen-bonding acceptor than carbonyl-O.[55,56] Hydrogen bonding in the **PBI-A** xerogel is due to the strong association of the carboxylic acid functional groups. In the hybrid xerogel instead of acid-acid hydrogen bonding, pyridine-acid interaction plays a predominant role, since the latter interaction is comparatively stronger. Hydrogen is shared between two

oxygen atoms (C=O…H-O) in the hydrogen bonded carboxylic acid groups. However, in the composite of **OPV-P** and **PBI-A**, carbonyl oxygen involves in hydrogen bonding with aromatic hydrogen. Due to the weak hydrogen bonding between aromatic carbon and carbonyl oxygen, carbonyl stretching frequency is higher in the composite xerogel.

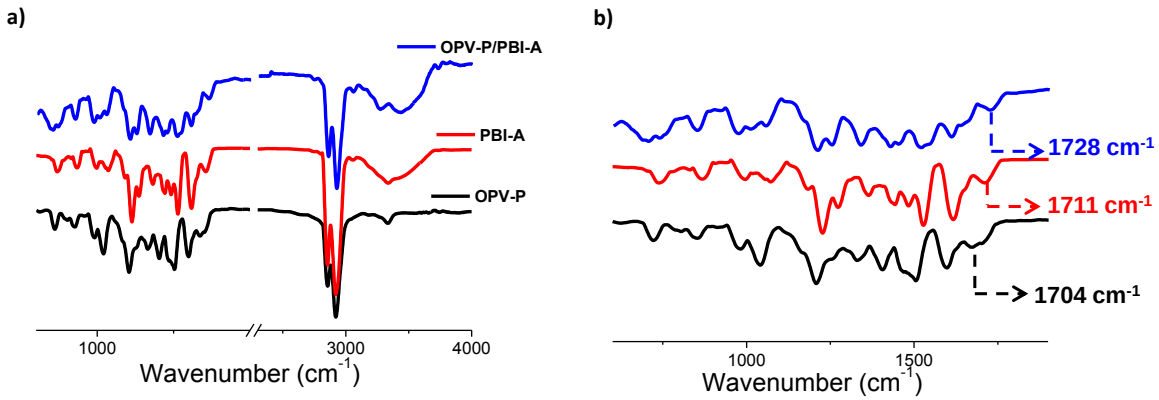

Figure 3.12. a) FT-IR spectra of **OPV-P**, **PBI-A** and the composite xerogel films. b) Zoomed spectra of the xerogels in the short wavenumber region.

3.3.5. X-ray Diffraction Studies

Molecular packing in the two component assembly was further investigated using X-ray diffraction (XRD) technique. **PBI-A** exhibited a long range ordering of molecules when compared to **OPV-P** (Figure 3.13). This can be ascribed to the strong π-π stacking between the rigid aromatic cores and directional hydrogen bonding between the carboxylic acid groups present in **PBI-A**. Supramolecular assembly depends on the molecular structure and various intra- as well as intermolecular interactions driven by the functional groups in the chromophores. Amide functionalities on the aromatic π-conjugated core play a vital role in determining the nature of the molecular

aggregation in **OPV-P** assembly. Amorphous XRD pattern of **OPV-P** indicates less defined molecular assembly which can be expected due to the interference of pyridine-N with amide hydrogen bonding, which limit the extent of the molecular assembly.

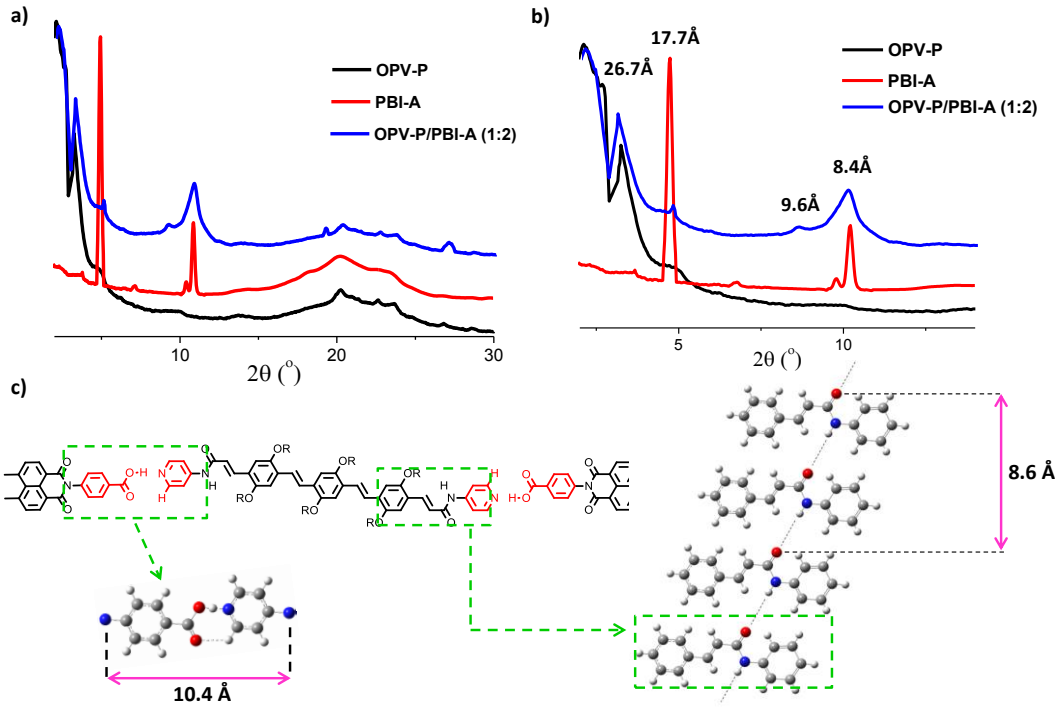

Figure 3.13. a) XRD pattern of **OPV-P**, **PBI-A** and their composite, b) zoomed region of a) from 2° to 15° and c) schematic representation of molecular interaction in the multicomponent assembly along with intermolecular spacing.

Xerogel made from the mixture of **OPV-P** and **PBI-A** was more crystalline in nature when compared to that of the individual constituents. This observation can be explained by the formation of ordered supramolecular nanostructures generated in the multicomponent assembly. XRD pattern of the hybrid sample shows two distinct peaks at 26.7 Å and 17.7 Å, which approximately matches with the length of the *π*-

conjugated core of **OPV-P** and **PBI-A**, respectively. Strong acid-pyridine interaction present in the hybrid films causes the mixed assembly of **OPV-P** and **PBI-A**. Since the pyridine-N is involved in complementary hydrogen bonding with carboxyl group, amide H-bonding in **OPV-P** is not disrupted. This will assist the ordered molecular assembly of π-chromophores. Hence, in the co-assembled film, the extent of π-π stacking will be comparatively higher than that of the individual samples, which facilitates more ordered molecular packing.

In order to solve the XRD pattern of the hybrid xerogel, we took crystal structure of cinnamylbenzanilide as standard since the cinnamide units are the crucial molecular part in the molecular assembly of **OPV-P**.[57] Distance between the hydrogen bonding moieties of two alternate π-stacks in cinnamylbenzanilide crystal packing (d ~ 8.6 Å) matches quite well with diffraction peak of the composite xerogel at 8.4 Å. Crystalline packing of pyridine carboxylic acid is used to get a detailed understanding of the acid-pyridine interactions in the composite of **OPV-P** and **PBI-A**.[58-60] It is demonstrated that the distance between the two synthons (acid and pyridine) is almost 10.4 Å, which was close enough with our experimental result (d ~ 9.6 Å) (Figure 3.13). These observations prove the extended molecular assembly in the multicomponent system which is driven by directional non-covalent interactions between the components.

The hybrid assembly of **OPV-P** and **PBI-B** did not show any characteristic peak to prove the mutual interaction between the components. Hybrid xerogel retains almost all peaks of the individual constituents. XRD analysis of the composite of **OPV-B** and **PBI-A** also discards the possibility of mutual interaction between the

constituents in the mixture. These observations confirm the crucial role of complementary interaction between the pyridine and carboxylic acid functionalities in the co-assembly of **OPV-P** and **PBI-A**.

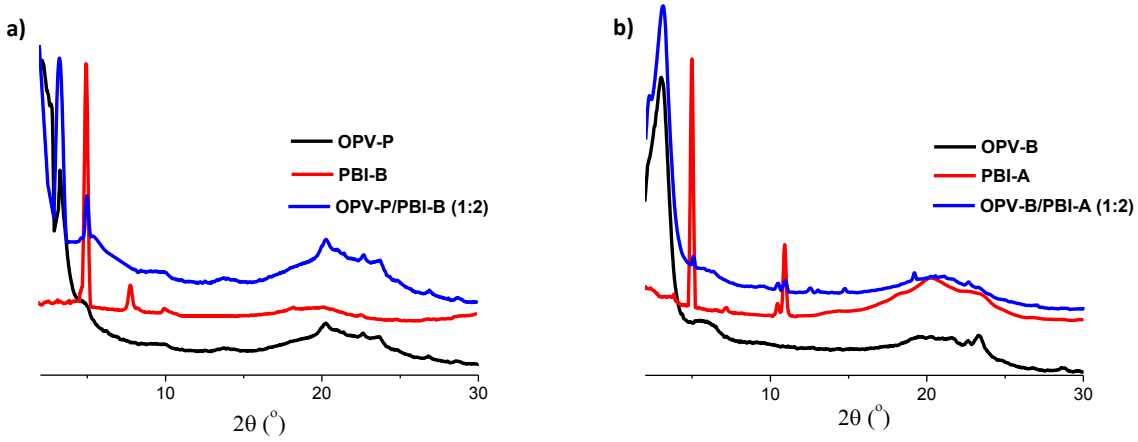

Figure 3.14. XRD pattern of a) **OPV-P**, **PBI-B** and their composite, b) **OPV-B**, **PBI-A** and their composite.

3.3.6. Morphological Studies

Morphological studies using atomic force microscopy and transmission electron microscopy showed short fibers of **OPV-P**. This feature justifies its inability to form strong gel (Figure 3.15). This observation can be ascribed due to the interference of the pyridine moiety on the extended amide hydrogen bonding as reported earlier.[44] **PBI-A** forms agglomerates and thin entangled fibers which can be attributed to the hydrogen bonded and π-stacked assembly between the carboxylic acid functional groups (Figure 3.15).

Microscopic studies of the composite of **OPV-P** and **PBI-A** at a ratio of 1:2 showed long nanofibers of 50 - 150 nm in width and several micrometers in length,

thus indicating extended co-assembly of the molecules (Figure 3.16). Due to the preferential acid-pyridine complementary interaction, interference of pyridine-N on the amide hydrogen bonding is reduced. This feature in the mixed assembly facilitates characteristic directional hydrogen bonding of the amide groups and hence the formed two-component supramolecular assembly is further stabilized by the concomitant π-π stacking between the aggregating molecules.

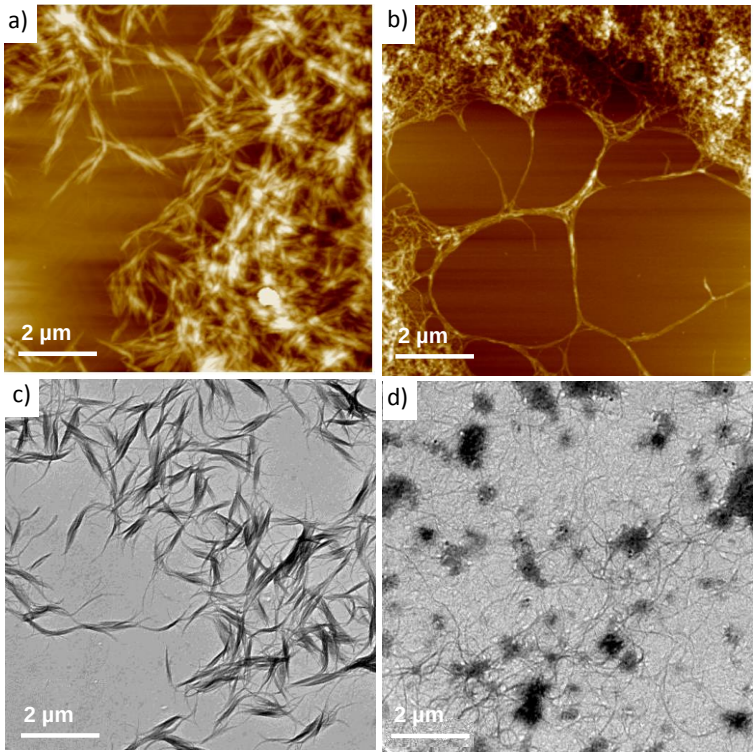

Figure 3.15. AFM images of a) **OPV-P** and b) **PBI-A**. TEM images of c) **OPV-P** and d) **PBI-A** [Concentration: **OPV-P** = 1× 10^{-5} M, **PBI-A** = 2 × 10^{-5} M in toluene/THF (9:1 v/v)].

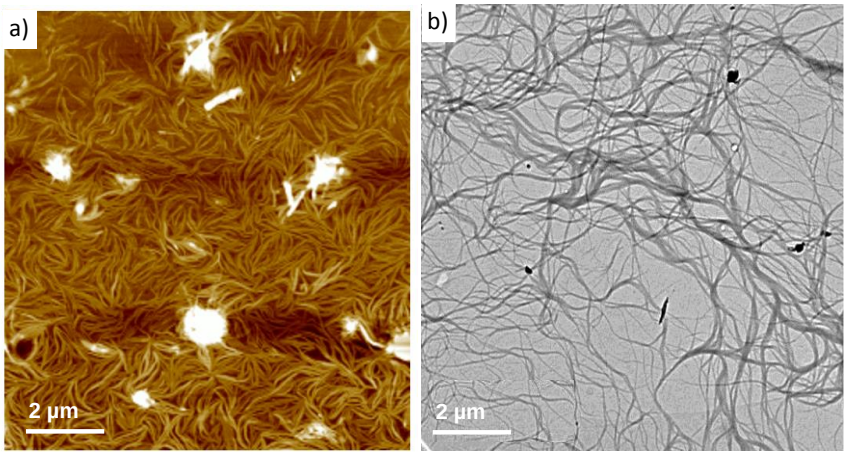

Figure 3.16. a) AFM and b) TEM images of **OPV-P**/**PBI-A** (1:2) mixture [Concentration of **OPV-P** = 1 × 10^{-5} M in toluene/THF (9:1 v/v)].

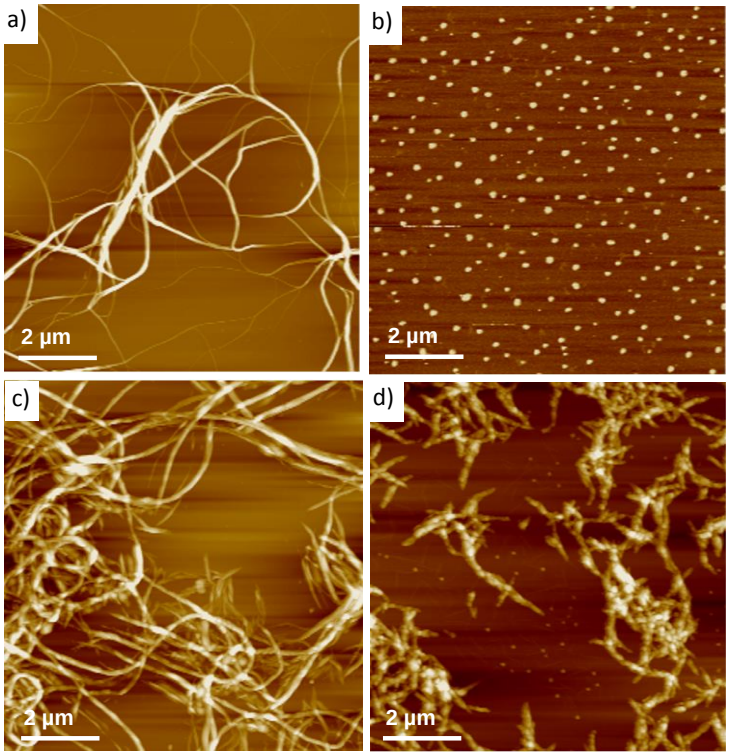

Figure 3.17. AFM images of a) **OPV-B**, b) **PBI-B**, c) **OPV-B**/**PBI-A** (1:2) and d) **OPV-P**/**PBI-B** (1:2) [Concentration: **OPV-P**, **OPV-B** = 1× 10^{-5} M, **PBI-A**, **PBI-B** = 2 × 10^{-5} M in toluene/THF (9:1 v/v)].

In contrast to the behavior of **OPV-P**, **OPV-B** forms extended nanofibers which clearly support our speculation of the interference of pyridine-N with the extended amide hydrogen bonding in the case of the former (Figure 3.17a). Morphological studies of a mixture of **OPV-B** and **PBI-A** revealed that the nanoscopic fibers of **OPV-B** does not change much with the addition of **PBI-A**. However, the cluster like features of **PBI-A** was absent indicating that **PBI-A** co-assemble with **OPV-B**. On the other hand **PBI-B** showed cluster like morphology due to the absence of extended directional supramolecular interactions and the composite of **OPV-P** and **PBI-B** did not show any extended supramolecular assembly (Figure 3.17d).

3.3.7. Conductivity Studies

Ordered molecular arrangement of π-conjugated molecules is a key factor for the optimal optoelectronic properties. We have performed four-probe conductivity measurements in order to understand the effect of co-assembly on the conducting properties. Due to the rigid π-conjugated core and its crystalline packing, the PBI derivatives (**PBI-A** and **PBI-B**) showed fairly good conductivity when compared to **OPV-P** and **OPV-B**. However it has been observed that the average electrical conductivity of the composite of **OPV-P** and **PBI-A** is better (11.93 Scm^{-1}) than that of the individual components (Figure 3.18a).

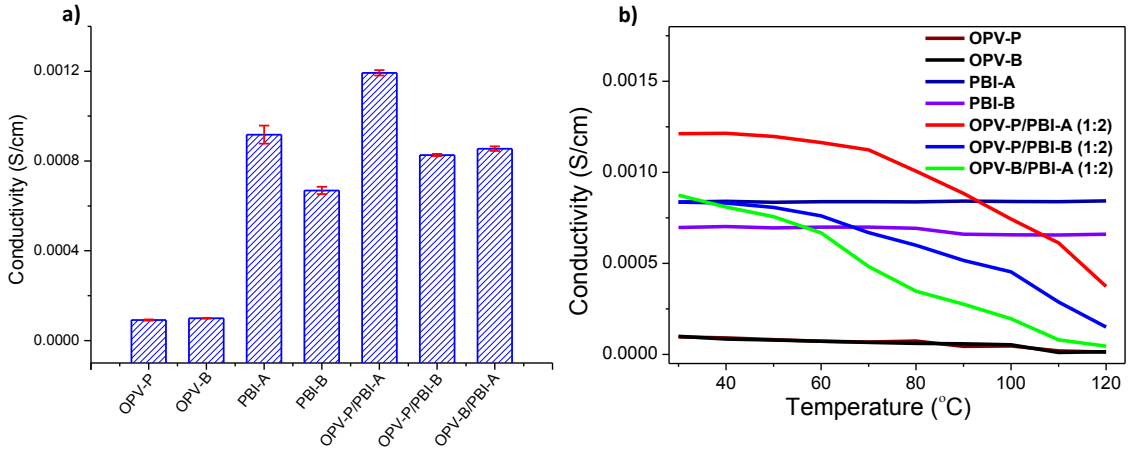

Figure 3.18. a) Four-probe (electrical) conductivity (S/cm) measurements of individual *π*-conjugated systems and mixtures. b) Temperature dependency of the conductivity.

However, conductivity measurements of other composites (**OPV-P**/**PBI-B** and **OPV-B**/**PBI-A**) under identical conditions did not show significant enhancement when compared to that of **OPV-P**/**PBI-A** mixture. These observations clearly indicate the role of ordered molecular arrangement of the *π*-conjugated cores in the enhanced conductivity of the mixture of **OPV-P** and **PBI-A**. Temperature-dependent measurement of electrical conductivity demonstrated the influence of the supramolecular co-assembly on the electrical properties of the films. It has been observed that electrical conductivity of PBI derivatives does not change much up to 120 °C. However, for the two component films, the conductivity decreases continuously with temperature. This observation indicates that molecular assembly gets disrupted with temperature and the slight collapse in the molecular arrangement leads to significant decrease in the conductivity (Figure 3.18b).

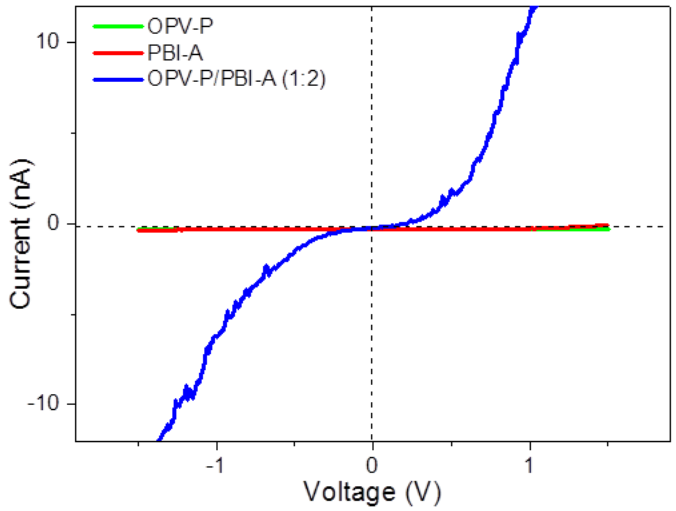

Figure 3.19. C-AFM measurements of xerogels obtained from Toluene/THF (9:1) solution drop-cast on HOPG substrate (Concentration: **OPV-P** = 1 × 10^{-5} M, **PBI-A** = 2 × 10^{-5} M).

Complementary interaction between the individual constituents in the composite of the **OPV-P** and **PBI-A**, facilitates ordered molecular arrangement of the π-conjugated chromophores in the nanofibers. The electrical transport characteristics of these fibers were further measured using the conducting probe atomic force microscopy (C-AFM) (Figure 3.19). Short fibers of **OPV-P** showed low conductivity of about 7.1×10^{-6} Scm^{-1} and the thin fibers of **PBI-A** showed comparatively higher conductivity about 6.3×10^{-5} Scm^{-1}.

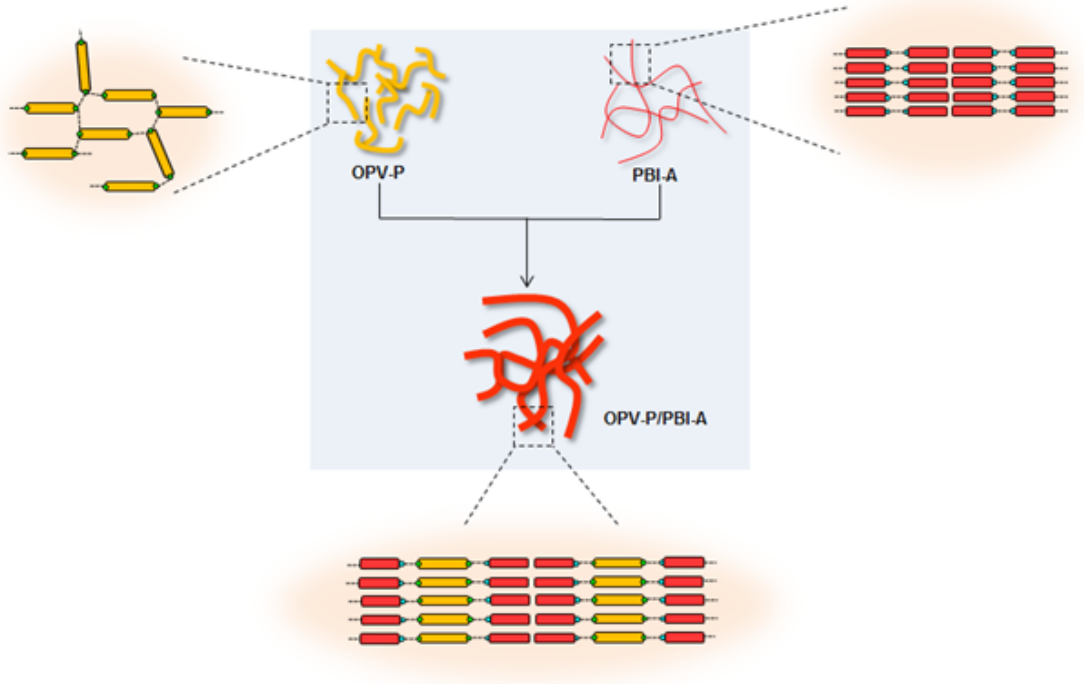

Scheme 3.5. Schematic representation of the bicomponent assembly of **OPV-P** and **PBI-A**.

The low conductivity of these individual film samples indicates less extended π-conjugation and inefficient charge carrier transport along the nanostructures in the self-assembled state. Under similar experimental conditions, the composite of **OPV-P** and **PBI-A** showed a moderately higher conductivity of about 9.4×10^{-4} Scm^{-1}. Measurements of other composite showed negligible conducting property as expected. This observation can be attributed to the availability of the better percolation pathways for the charge carrier transport in the co-assembled films. The hybrid nanostructures showed better charge carrier transport due to the well-ordered π-core arrangement in the co-assembly (Scheme 3.5).

3.4. Conclusions

We demonstrated the use of acid-pyridine complementary interaction in constructing co-assembly from oligo(*p*-phenylenevinylene) and perylenebisimide based systems. Composite gels of **OPV-P** and **PBI-A** showed enhanced thermal and mechanical stability than that of the neat **OPV-P** gel. Temperature dependent spectral studies revealed the difference in the mechanism of supramolecular polymerization of individual constituents and the composite. Extended supramolecular assemblies were formed by the composite of **OPV-P** and **PBI-A**, when compared to the individual constituents. Conducting atomic force microscopy (C-AFM) study revealed that the electrical conductivity of the mixed assembly of **OPV-P** and **PBI-A** is far better than that of the individual components. Poor conductivity of the two component systems without the acid-pyridine functionalities, established the crucial role of the complementary interaction on the supramolecular assembly and its electronic properties. Therefore, this work highlights the need for the detailed understanding on the engineering of the functional supramolecular assembly of π-systems and their optoelectronic applications.

3.5. Experimental Section

3.5.1. Synthesis and Characterizations

Synthesis of ethyl 2-(diethoxyphosphoryl)acetate (**12**): Ethyl 2-(diethoxy phosphoryl) acetate (**12**) was prepared by reacting ethyl 2-bromoacetate (1.5 g, 8.98 mmol) with 2 mL of triethyl phosphite at 110 ^{o}C for 10 h. Removal of the unreacted triethyl phosphite under reduced pressure gave the phosphonate ester as a colorless

liquid in 95% yield. FT-IR (KBr): ν_{max} = 661, 744, 975, 1055, 1116, 1163, 1211, 1255, 1369, 1392, 1442, 1477, 1510, 1734, 2872, 2908, 2937, 3018 cm^{-1}; ^{1}H NMR (500 MHz, $CDCl_3$, TMS): δ (ppm): 1.27-1.38 (m, 9H), 2.93-3.00 (d, 2H), 4.13-4.24 (m, 6H); ^{13}C NMR (125 MHz, $CDCl_3$): δ (ppm): 14.10, 16.20, 35.10, 61.92, 167.10; HRMS-FAB: Calculated [M^+] for $C_8H_{17}O_5P$: 224.19, found: 224.17.

Synthesis of OPV-Bisester (**OPV2**): To a solution of the bisaldehyde, **OPV1** (290 mg, 0.20 mmol) and the phosphonate ester **12** (105 mg, 0.46 mmol), in 35 mL THF, NaH (30 mg, 1.24 mmol) was carefully added under argon atmosphere. The reaction mixture was refluxed for 5 h, and the solvent was removed under reduced pressure. The resultant residue was extracted with chloroform and washed several times with saturated brine and water. The organic layer was concentrated and the crude product was purified by column chromatography (hexane/chloroform, 3:1) over silica gel to afford **OPV2** as a dark red solid in 90% yield. m.p.: 143 ± 2 °C; FT-IR (KBr): ν_{max} = 717, 802, 854, 962, 1022, 1105, 1207, 1261, 1423, 1506, 1595, 1618, 1781, 2850, 2922 cm^{-1}; ^{1}H NMR (500 MHz, $CDCl_3$, TMS): δ (ppm): 0.85-0.89 (m, 18H), 1.24-1.86 (m, 120H), 3.97-4.07 (m, 12H), 4.23-4.3 (q, 4H), 6.42-6.46 (d, 2H), 6.96-7.01 (d, 2H), 7.05-7.07 (m, 4H) 7.38- 7.48 (m, 2H), 7.99 (d, 2H); ^{13}C NMR (125 MHz, $CDCl_3$): δ (ppm): 14.12, 14.21, 26.21, 26.30, 29.38, 29.53, 231.92, 61.38, 69.39, 110.09, 110.60, 112.31, 115.89, 117.86, 123.19, 124.93, 127.38, 130.52, 138.74, 150.62, 151.17, 152.49, 166.58; MALDI-TOF MS: Calculated *m*/*z* for $C_{104}H_{174}O_{10}$: 1584.53, found: 1585.71.

Synthesis of the OPV-Bisacid (**OPV3**): KOH (50 mg, 0.85 mmol) in methanol (20 mL) was added to a solution of **OPV2** (270 mg, 0.17 mmol) in distilled THF (20 mL). The reaction mixture was then refluxed for 4 h. After checking the completion of reaction by TLC, the solvent was evaporated under reduced pressure. The resulting suspension was poured into water, extracted with $CHCl_3$ and trifluoroacetic acid was added to adjust the pH around 2. The $CHCl_3$ layer was washed with water several times. Removal of the solvent gave **OPV3** as a dark red solid in 95 % yield. m.p.: 120 ± 2 °C; FT-IR (KBr): ν_{max} = 801, 856, 1031, 1097, 1203, 1261, 1420, 1466, 1500,1593, 1619, 1757, 2849, 2924, 3423 cm^{-1}; ^1H NMR (500 MHz, $CDCl_3$, TMS): δ (ppm): 0.86-0.90 (m, 18H), 1.26-1.89 (m, 120H), 4.01-4.09 (m, 12H), 6.52-6.56 (d, 2H), 7.05-7.06 (d, 2H), 7.16-7.17 (m, 4H) 7.47-7.58 (m, 2H), 7.99 (d, 2H); ^{13}C NMR (125 MHz, $CDCl_3$): δ (ppm): 14.10, 14.20, 22.70, 25.90, 29.30, 29.60, 31.80, 61.40, 69.10, 81.40, 114.80, 116.00, 116.20, 125.60, 141.60, 145.70, 166.40, 171.20; MALDI-TOF MS: Calculated *m*/*z* for $C_{100}H_{166}O_{10}$: 1528.42, found: 1528.77.

General procedure for the synthesis of OPV-P and OPV-B: To a dry dichloromethane (50 mL) solution of **OPV3** (140 mg, 0.09 mmol) and **HATU** in the presence of *N*,*N*′- diisopropylethylamine (70 µL, 0.4 mmol), kept at 0 °C, required amine (0.39 mmol) for example 4-aminopyridine (40 mg) for **OPV-P** and aniline (40 µL) for **OPV-B** were added. Reaction mixture was stirred for 8 h at room temperature. The reaction mixture was extracted with dichloromethane and washed several times with water, dried over anhydrous sodium sulfate and the solvent was removed under reduced pressure. Purification was done by column chromatography (hexane/$CHCl_3$, 1:9) over neutral alumina.

OPV-P: Yield-60 %; m.p.: 163 ± 2 °C; FT-IR (KBr): ν_{max} = 535, 718, 790, 846, 975, 1031, 1169, 1207, 1240, 1281, 1314, 1345, 1410, 1465, 1510, 1585, 1665, 2854, 2927, 3313 cm^{-1}; ^{1}H NMR (500 MHz, $CDCl_3$, TMS): δ (ppm): 0.85-0.87 (m, 18H, -CH_3), 1.16-1.28 (m, 120 H, -CH_2-), 3.90-4.10 (m, 12H, -OCH_2-), 6.57-6.62 (d, 2H, vinylic), 6.95-7.00 (d, 2H), 7.09-7.10 (m, 4H), 7.28-7.31 (m, 2H), 7.37-7.43 (d, 4H), 7.43-7.45 (d, 2H), 7.91-7.96 (d, 2H), 8.45-8.47 (d, 4H); ^{13}C NMR (125 MHz, $CDCl_3$): δ (ppm): 14.20, 22.70, 25.90, 29.30, 29.60, 31.60, 69.00, 109.20, 114.80, 116.10, 118.80, 125.20, 140.20, 143.10, 145.30, 150.30, 155.60, 165.80; MALDI-TOF MS: Calculated *m*/*z* for $C_{110}H_{174}N_4O_8$: 1680.62, found: 1680.84.

OPV-B: Yield-70 %; m.p.: 154 ± 2 °C; FT-IR (KBr): ν_{max} = 479, 509, 549, 602, 695, 720, 755, 849, 962, 1009, 1072, 1209, 1251, 1348, 1387, 1416, 1440, 1470, 1498, 1514, 1530, 1598, 1615, 1657, 2845, 2925, 3052, 3267 cm^{-1}; ^{1}H NMR (500 MHz, $CDCl_3$, TMS): δ (ppm): 0.85-0.89 (m, 18H), 1.25-1.70 (m, 120H), 3.9-4.10 (m, 12H), 6.65-6.69 (d, 2H), 7.04-7.6 (m, 18H), 7.97-8.00 (d, 2H); ^{13}C NMR (125 MHz, $CDCl_3$): δ (ppm): 14.22, 22.70, 25.93, 29.33, 29.60, 31.60, 69.00, 109.20, 114.80, 116.10, 118.80,121.50, 128.20, 130.40, 140.24, 143.14, 145.32, 150.31, 155.60, 165.84; MALDI-TOF MS: Calculated *m*/*z* for $C_{112}H_{176}N_2O_8$: 1678.65, found:1678.89.

Synthesis of 1-Hexylheptylamine (13): A 250 mL round-bottom flask was charged with 7-tridecanone (10.4 g, 52.50 mmol), NH_4OAc (40.1 g, 0.52 mol), $NaBH_3CN$ (2.3 g, 38 mmol) and MeOH (75 mL). The mixture was stirred at room temperature for 48 h, until the starting material was absent by checking with TLC. The reaction was quenched by drop wise addition of conc. HCl (6 mL), and the solvents removed by rotary evaporation. The resulting white solid was dissolved in H_2O (500 mL) and

adjusted to pH ~ 10 with solid KOH, then extracted with $CHCl_3$. The $CHCl_3$ extract was concentrated to give the product as pale yellow oil with 97% yield. ^{1}H NMR (500 MHz, MeOH-d_4, TMS): 0.84 (t, 6H), 1.12-1.19 (m, 16H), 1.48 (m, 4H), 2.79 (qn, 1H); ^{13}C NMR (125 MHz, MeOH-d_4) δ (ppm): 14.11, 22.73, 26.79, 29.37, 31.88, 37.90, 50.85; HRMS-FAB: Calculated [M^+] for $C_{13}H_{29}N$: 199.38, found: 199.71.

Synthesis of *N,N′*-bis(1-hexylheptyl)-3,4,9,10-perylene dicarboxamide (PBI-2): A mixture of perylene-3,4,9,10-tetracarboxylic dianhydride (**PBI-1**) (0.39 g, 1 mmol), zinc acetate (0.17 g, 0.75 mmol), imidazole (4 g) as solvent and 1-hexylheptylamine (**13**) (0.60 g, 3 mmol) was vigorously stirred at 160 °C for 2 h. After cooling to room temperature, the mixture was dissolved in minimum amount of THF and precipitated in 300 mL 2 N HCl/methanol 2:1 v/v. The precipitate was filtered and washed with water followed by methanol and dried at 80 °C under vacuum. The crude product was further purified by column chromatography over silica gel (50% $CHCl_3$/hexane). Yield: 65%; m.p.: 158 ± 2 °C; FT-IR (KBr): ν_{max} = 746, 810, 851, 1254, 1338, 1406, 1595, 1659, 1700, 2856, 2927 cm^{-1}; ^{1}H NMR (500 MHz, $CDCl_3$, TMS): δ (ppm): 0.83-0.81 (t, 12H), 1.33-1.22 (m, 32H), 1.87-1.83 (m, 4H), 2.27-2.21 (m, 4H), 5.21-5.15 (m, 2H), 8.70-8.64 (m, 8H); ^{13}C NMR (125 MHz, $CDCl_3$) δ (ppm): 14.10, 22.74, 26.73, 29.39, 31.83, 32.51, 53.74, 124.50, 126.17, 129.23, 130.94, 135.76, 159.07; HRMS-FAB: Calculated [M^+] for $C_{50}H_{62}N_2O_4$: 755.06, found: 755.23.

Synthesis of *N*-(1-hexylheptyl)perylene-3,4,9,10-tetracarboxylic-3,4-anhydride-9,10-imide (PBI-3): In a 250 mL round bottom flask, **PBI-2** (0.5 g, 0.66 mmol) was suspended in 70 mL *tert*-butanol and was treated with of 85% KOH. The reaction mixture was refluxed under vigorous stirring until the solution turned dark purple.

The mixture was cooled to room temperature, treated with 80 mL acetic acid and 40 mL 2 N HCl and stirred overnight. The dark red precipitate was filtered washed with water and dried at 130 °C. The solid was suspended in 150 mL 10% K_2CO_3 solution and refluxed for 30 minutes. The mixture was then cooled to room temperature and filtered. The filter cake was washed with warm 10% K_2CO_3 until the filtrate was clear, rinsed twice with approximately 100 mL 2 N HCl and rinsed thoroughly with water and dried at 130 °C. The solid was then suspended in 100 mL boiling water and triethylamine was added until a dark purple solution of the desired product was formed. Remaining starting material was filtered off and the dark filtrate was acidified with 30 mL 2 N HCl and stirred overnight. The resulting dark precipitate was filtered and rinsed with water and dried. Yield: 40%; m.p.: 208 ± 2 °C; FT-IR (KBr): ν_{max} = 841, 1214, 1378, 1423, 1605, 1669, 1712, 2812, 2932 cm^{-1}; ^1H NMR (500 MHz, $CDCl_3$, TMS): δ (ppm): 0.83-0.81 (t, 12H), 1.33-1.22 (m, 16H), 1.87-1.83 (m, 2H), 2.27-2.21 (m, 2H), 5.21-5.15 (m, 1H), 8.01 (m, 2H), 8.73-8.67 (m, 6H); ^{13}C NMR (125 MHz, $CDCl_3$) δ (ppm): 14.10, 22.71, 26.73, 29.36, 31.83, 32.51, 53.53, 124.51, 126.17, 129.23, 130.94, 135.76, 159.10; HRMS-FAB: Calculated [M^+] for $C_{37}H_{35}NO_5$: 573.69, found: 574.10.

General procedure for the synthesis of PBI-A and PBI-B: **PBI-3** (0.2 g, 0.349 mmol) and imidazole (1 g) were mixed with 4-aminobenzoic acid (143 mg, 1.046 mmol) for **PBI-A** and aniline (96 µL, 1.046 mmol) for **PBI-B**. The reaction mixture was vigorously stirred at 140 °C for 24 h. The crude product was diluted with CH_2Cl_2 (40 mL) and extracted with water. The organic layer was dried over $CaSO_4$ and

evaporated under vacuum. The crude product was purified by silica gel column chromatography (CH_2Cl_2 then CH_2Cl_2/MeOH: 97/3).

PBI-A: Yield-74%; m.p.: > 300 °C; FT-IR (KBr): ν_{max} = 811, 1343, 1579, 1594, 1658, 1698, 2850, 2922, 2952, 3306 cm^{-1}; ^1H NMR (500 MHz, $CDCl_3$, TMS) δ (ppm): 0.83 (t, 6H), 1.32-1.23 (m, 16H), 1.90-1.85 (m, 2H), 2.28-2.20 (m, 2H), 5.18 (hept, 1H), 7.37 (d, 2H), 7.53-7.49 (m, 1H), 7.60-7.57 (m, 2H), 8.72-8.60 (m, 8H); ^{13}C NMR (125 MHz, $CDCl_3$) δ (ppm): 14.11, 22.73, 26.78, 29.33, 31.82, 32.50, 53.44, 124.31, 124.53, 125.81, 126.14, 129.20, 130.55, 130.90, 135.79, 137.91, 158.65, 159.60, 169.34; HRMS-FAB: Calculated [M^+] for $C_{44}H_{40}N_2O_6$: 692.81, found: 693.21.

PBI-B: Yield-74%; m.p.: > 300 °C; FT-IR (KBr): ν_{max} = 845, 1243, 1532, 1579, 1688, 1706, 2841, 2923, 2961 cm^{-1}; ^1H NMR (500 MHz, $CDCl_3$, TMS) δ (ppm): 0.83 (t, 6H), 1.32-1.23 (m, 16H), 1.90-1.85 (m, 2H), 2.30-2.20 (m, 2H), 5.14 (hept, 1H), 7.33 (d, 2H), 7.52-7.50 (m, 1H), 7.64-7.54 (m, 2H), 8.73-8.63 (m, 8H); ^{13}C NMR (125 MHz, $CDCl_3$) δ (ppm): 14.10, 22.73, 26.70, 29.31, 31.82, 32.54, 53.48, 124.53, 126.61, 128.03, 128.12, 128.97, 129.20, 130.91, 132.74, 135.78, 158.65, 159.04; HRMS-FAB: Calculated [M^+] for $C_{43}H_{40}N_2O_4$: 648.8, found: 649.13.

3.5.2. Current Sensing (Conductive) Atomic Force Microscopy (C-AFM)

We have used the tapping mode to image the samples with a resonance frequency of 224 kHz and a spring constant of 6-22 Nm^{-1}. Micro-fabricated diamond coating was doped with nitrogen cantilever tips (DCP11) and employed an operator-activated external circuit to switch to contact mode for point contact electrical characterization

of the selected positions. After completion of the measurement, we have deactivated the external circuit to return to the tapping mode feedback. This procedure prevents damage to the gel fibers and the metal coated tips by avoiding the frictional wear associated with the contact mode imaging. Samples for the imaging and electrical properties were prepared by drop casting the sample solution on highly ordered pyrolytic graphite (HOPG) at the required concentrations at ambient conditions. Conductance was measured on the bundled fibers at different positions before and after exposing to iodine vapors at different intervals. The value of the conductivity (σ) was calculated from the equation

$\sigma = d/(A_t R)$ S/cm

where 'σ' is the conductivity, and 'd' is the film thickness (~ 50-60 nm). 'A_t' is the area of the C-AFM probe in contact with the surface. 'A_t' was computed as 'πr^2', assuming that the contact radius between tip and sample is 70 nm. 'R' is the resistance of the sample, estimated from the inverse slope of the I-V curve.

3.5.3. Four-Probe dc Resistance Measurements

For conductivity measurements, xerogels were prepared on glass slides from the samples. Then xerogels were put on the base plate of the four probe arrangement. The probes were placed on the flat surface of the film. Current was passed through the two outer electrodes, and the floating potential was measured across the inner pair. In this measurement, a known current was applied and the potential across the probes was determined. This experiment was repeated three times and the average resistance values were taken. The value of the resistivity (r) was calculated from the equation

$\rho = (V/I) \times \pi t/\ln 2$

where t = thickness of the film. The conductivity (σ) was calculated from the equation, $\sigma = 1/\rho_{actual}$ (S/cm).

3.6. References

1. Buerkle, L. E., Rowan, S. J. *Chem. Soc. Rev*. **2012**, *41*, 6089-6102.
2. Raeburn, J., Adams D. J. *Chem. Commun*. **2015**, *51*, 5170-5180.
3. Ryan, D. M., Doran, T. M., Nilsson, B. L. *Chem. Commun*. **2011**, *47*, 475-477.
4. Hardy, J. G., Hirst, A. R., Smith, D. K., Brennan, C., Ashworth, I. *Chem. Commun*. **2005**, 385-387.
5. Das, R. K., Kandanelli, R., Linnanto, J., Bose, K., Maitra, U. *Langmuir* **2010**, *26*, 16141-16149.
6. Steed, J. W. *Chem. Soc. Rev*. **2010**, *39*, 3686-3699.
7. Piotrowiak, P. *Chem. Soc. Rev*. **1999**, *28*, 143-150.
8. Shu, T., Wu, J., Lu, M., Chen, L., Yi, T., Li, F., Huang, C. *J. Mater. Chem*. **2008**, *18*, 886-893.
9. Bouteiller, L., Colombani, O., Lortie, F., Terech, P. *J. Am. Chem. Soc*. **2005**, *127*, 8893-8898.
10. Ryan, D. M., Doran, T. M., Nilsson, B. L. *Langmuir* **2011**, *27*, 11145-11156.
11. Jiang, W., Winkler, H. D. F., Schalley, C. A. *J. Am. Chem. Soc*. **2008**, *130*,13852-13853.
12. Sempere, M. M. S., Fernandez, G., Wurthner, F. *Chem. Rev*. **2011**, *111*, 5784-5814.

13. Yan, X., Xu, D., Chi, X., Chen, J., Dong, S., Ding, X., Yu, Y., Huang, F. *Adv. Mater*. **2012**, *24*, 362-369.
14. van Herrikhuyzen, J., Syamakumari, A., Schenning, A. P. H. J., Meijer, E. W. *J. Am. Chem. Soc*. **2004**, *126*, 10021-10027.
15. Sugiyasu, K., Kawano, S., Fujita, N., Shinkai, S. *Chem. Mater*. **2008**, *20*, 2863-2865.
16. Prasanthkumar, S., Ghosh, S., Nair, V. C., Saeki, A., Seki, S., Ajayaghosh, A. *Angew. Chem. Int. Ed*. **2015**, *54*, 946-950.
17. Narayan, B., Bejagam, K. K., Balasubramanian, S., George, S. J. *Angew. Chem. Int. Ed*. **2015**, *54*, 13053-13057.
18. Elemans, J. A. A. W., Lei, S., De Feyter, S. *Angew. Chem. Int. Ed*. **2009**, *48*, 7298-7332.
19. Jolliffe, K. A., Timmerman, P., Reinhoudt, D. N. *Angew. Chem. Int. Ed*. **1999**, *38*, 933-937.
20. Corbin, P. S., Lawless, L. J., Li, Z., Ma, Y., Witmer, M. J., Zimmerman, S. C. *Proc. Natl. Acad. Sci. U.S.A.* **2002**, *99*, 5099-5104.
21. Ma, Y., Kolotuchin, S. V., Zimmerman, S. C. *J. Am. Chem. Soc*. **2002**, *124*, 13757-13769.
22. Caulder, D. L., Raymond, K. N. *Angew. Chem. Int. Ed. Engl*. **1997**, *36*, 1440-1442.
23. Enemark, E. J., Stack, T. D. P. *Angew. Chem. Int. Ed*. **1998**, *37*, 932-935.
24. Barboiu, M., Dumitru, F., Legrand, Y.-M., Petita, E., van der Lee, A. *Chem. Commun*. **2009**, 2192-2194.

25. Shaller, A. D., Wang, W., Gan, H., Li, A. D. Q. *Angew. Chem. Int. Ed*. **2008**, *47*, 7705-7709.

26. Bilgicer, B., Xing, X., Kumar, K. *J. Am. Chem. Soc*. **2001**, *123*,11815-11816.

27. Schnarr, N. A., Kennan, A. J. *J. Am. Chem. Soc*. **2003**, *125*, 667-671.

28. Das, A., Ghosh, S. *Chem. Commun*. **2011**, *47*, 8922-8924.

29. Rao, K. V., Jayaramulu, K., Maji, T. K., George, S. J. *Angew. Chem. Int. Ed*. **2010**, *49*, 4218-4222.

30. Foster, J. A., Edkins, R. M., Cameron, G. J., Colgin, N., Fucke, K., Ridgeway, S., Crawford, A. G., Marder, T. B., Beeby, A., Cobb, S. L., Steed, J. W. *Chem. Eur. J*. **2014**, *20*, 279-291.

31. Guerzo, A. D., Olive, A. G. L., Reichwagen, J., Hopf, H., Desvergne, J.-P. *J. Am. Chem. Soc*. **2005**, *127*, 17984-17985.

32. Rao, K. V., George, S. J. *Chem. Eur. J*. **2012**, *18*, 14286-14291.

33. Kato, T., Frechet, J. M. J. *J. Am. Chem. Soc*. **1989**, *111*, 8533-8534.

34. Lee, J. Y., Painter, P. C., Coleman, M. M. *Macromolecules* **1988**, *21*, 954-960.

35. Fujita, N., Yamashita, T., Asai, M., Shinkai, S. *Angew. Chem. Int. Ed*. **2005**, *44*, 1257-1261.

36. Xue, P., Xu, Q., Gong, P., Qian, C., Zhang, Z., Jia, J., Zhao, X., Lu, R., Ren, A., Zhang, T. *RSC Adv*. **2013**, *3*, 26403-26411.

37. Xue, P., Wang, P., Yao, B., Sun, J., Gong, P., Zhang, Z., Qian, C., Lu, R. *ACS Appl. Mater. Interfaces* **2014**, *6*, 21426-21434.

38. Xue, P., Wang, P., Yao, B., Sun, J., Gong, P., Zhang, Z., Lu, R. *RSC Adv.* **2015**, *5*, 75425-75433.

39. Charvet, R., Yamamoto, Y., Sasaki, T., Kim, J., Kato, K., Takata, M., Saeki, A., Seki, S., Aida, T. *J. Am. Chem. Soc*. **2012**, *134*, 2524-2527.

40. Bhosale, S., Sisson, A. L., Talukdar, P., Furstenberg, A., Banerji, N., Vauthey, E., Bollot, G., Mareda, J., Roger, C., Wurthner, F., Sakai, N., Matile, S. *Science* **2006**, *313*, 84-86.

41. Zhang, X., Wang, C. *Chem. Soc. Rev*. **2011**, *40*, 94-101.

42. Jonkheijm, P., Stutzmann, N., Chen, Z., de Leeuw, D. M., Meijer, E. W., Schenning, A. P. H. J., Wurthner, F. *J. Am. Chem. Soc*. **2006**, *128*, 9535-9540.

43. Wurthner, F., Chen, Z., Hoeben, F. J. M., Osswald, P., You, C.-C., Jonkheijm, P., Herrikhuyzen, J., Schenning, A. P. H. J., van der Schoot, P. P. A. M., Meijer, E. W., Beckers, E. H. A., Meskers, S. C. J., Janssen, R. A. J. *J. Am. Chem. Soc*. **2004**, *126*, 10611-10618.

44. Kartha, K. K., Praveen, V. K., Babu, S. S., Cherumukkil, S., Ajayaghosh A. *Chem. Asian J*. **2015**, *10*, 2250-2256.

45. Sandeep, A., Praveen, V. K., Kartha, K. K., Karunakaran, V., Ajayaghosh, A. *Chem. Sci*. **2016**, *7*, 4460-4467.

46. Wescott, L. D., Mattern, D. L. *J. Org. Chem*. **2003**, *68*, 10058-10066.

47. Salavagione, H. J., Martinez, G., Gomez, R., Segura, J. L. *Journal of Polymer Science: Part A: Polymer Chemistry* **2010**, *48*, 3613-3622.

48. Stepanenko, V., Li, X.-Q., Gershberg, J., Würthner, F. *Chem. Eur. J*. **2013**, *19*, 4176-4183.

49. Chen, Z., Lohr, A., Saha-Moller, C. R., Wurthner, F. *Chem. Soc. Rev*. **2009**, *38*, 564-584.

50. Smulders, M. M. J., Nieuwenhuizen, M. M. L., de Greef, T. F. A., van der Schoot, P., Schenning, A. P. H. J., Meijer, E. W. *Chem. Eur. J*. **2010**, *16*, 362-367.

51. Smulders, M. M. J., Schenning, A. P. H. J., Meijer, E. W. *J. Am. Chem. Soc*. **2008**, *130*, 606-611.

52. Li, J.-L., Liu, X.-Y. *Adv. Funct. Mater*. **2010**, *20*, 3196-3216.

53. Adhia, Y. J., Schloemer, T. H., Perez, M. T., McNeil, A. J. *Soft Matter* **2012**, *8*, 430-434.

54. Huang, R., Qi, W., Feng, L., Su, R.., He, Z. *Soft Matter* **2011**, *7*, 6222-6230.

55. Mukherjee, A., Desiraju, G. R. *Cryst. Growth Des*. **2014**, *14*, 1375-1385.

56. Li, T., Zhou, P., Mattei, A. *CrystEngComm* **2011**, *13*, 6356-6360.

57. Bugenhagen, B., Jasemb, Y. A., Thiemann, T. *IUCrData* **2016**, *1*, x160647.

58. Dale, S. H., Elsegood, M. R. J., Hemmings, M., Wilkinson, A. L. *CrystEngComm* **2004**, *6*, 207-214.

59. Lou, B.-Y., Huang, X.-D., Lin, X.-C. *Acta Cryst*. **2006**, *C62*, o310-o311.

60. Dubey, R., Desiraju, G. R. *Chem. Commun*. **2014**, *50*, 1181-1184.

61. Saeki, A., Koizumi, Y., Aida, T., Seki, S. *Acc. Chem. Res*. **2012**, *45*, 1193-1202.

62. Seki, S., Saeki, A., Sakurai, T., Sakamaki, D. *Phys. Chem. Chem. Phys*. **2014**, *16*, 11093-11113.

Chapter 4

Improving Intermolecular Packing and Semiconducting Property of Donor-Acceptor π-Conjugated Polymers by Backbone Engineering

4.1. Abstract

Semiconducting property of π-conjugated polymers depend on the conjugation length, functional groups and order of the molecular packing in the solid state. Three-component random copolymers having different ratios of [1]benzothieno[3,2-b]benzothiophene (BTBT) and diketopyrrolopyrrole (DPP) units were synthesized, and their application in organic field effect transistors (OFET) has been discussed in this chapter. These low band gap polymers exhibit p-type semiconducting properties and it has been observed that increase in the percentage composition of the fused chalcogenophene (BTBT) in the polymer backbone significantly improves the charge carrier mobility (μ_h) to 2.47 $cm^2V^{-1}s^{-1}$. The grazing incidence X-ray diffraction (GIXRD) technique and atomic force microscopy (AFM) have been used to explain the influence of BTBT on the nature of molecular packing in the polymer thin films. These diffraction data reveal that the incorporation of rigid planar chalcogenophene (BTBT) in the backbones favors the efficient packing of alkyl chains and enhance the interchain π-π interactions. These results unveil the role of the effective conjugation length as well as the intermolecular ordering of the polymer chains on the charge carrier transport in OFET.

4.2. Introduction

Organic field effect transistors (OFETs) have received increasing attention because of their potential application in various areas.[1-3] Among the successful organic semiconductors, conjugated polymers rule over small molecules due to their better solution processability, flexibility, and stability. These advantages encouraged significant research activities on the semiconducting polymers.[4-7] Polymeric semiconductors typically exhibit minimal grain boundaries and excellent film-forming properties, which are essential requirements for fabrication of large-area devices by printing.[4-10] Semiconducting properties of the conjugated polymers depend on various factors such as molecular orbital energy levels, inter/intramolecular interactions, thin film morphology, etc. Thus, the polymer backbone as well as the alkyl side chains play a vital role in determining the field effect mobility.[11-14] Generally OFET performance not only depend on the inherent molecular nature but also on several factors, such as molecular orientation, crystallinity of the film, uniformity and connectivity between crystalline grains. Efficient transport of charge carrier from one molecule to other depends on the electron cloud on the molecules as well as the extent of π-overlap between the neighboring molecules.[15-20] Hence, a proper understanding of the structure-property relationship is crucial in designing polymers with extensive intermolecular ordering and charge carrier mobility in solid state.

Efficient performance of an OFET is eventually determined by the transfer integral and reorganization energy.[15-22] High transfer integral and low reorganization energy favor good charge carrier mobility.[21,22] In order to achieve these, recently a lot

of attempts have been made in functional group engineering on the π-conjugated polymer systems.[11,12,23-25] The transfer integral and reorganization energy are significantly affected by the packing (arrangement) of the π-conjugated systems.

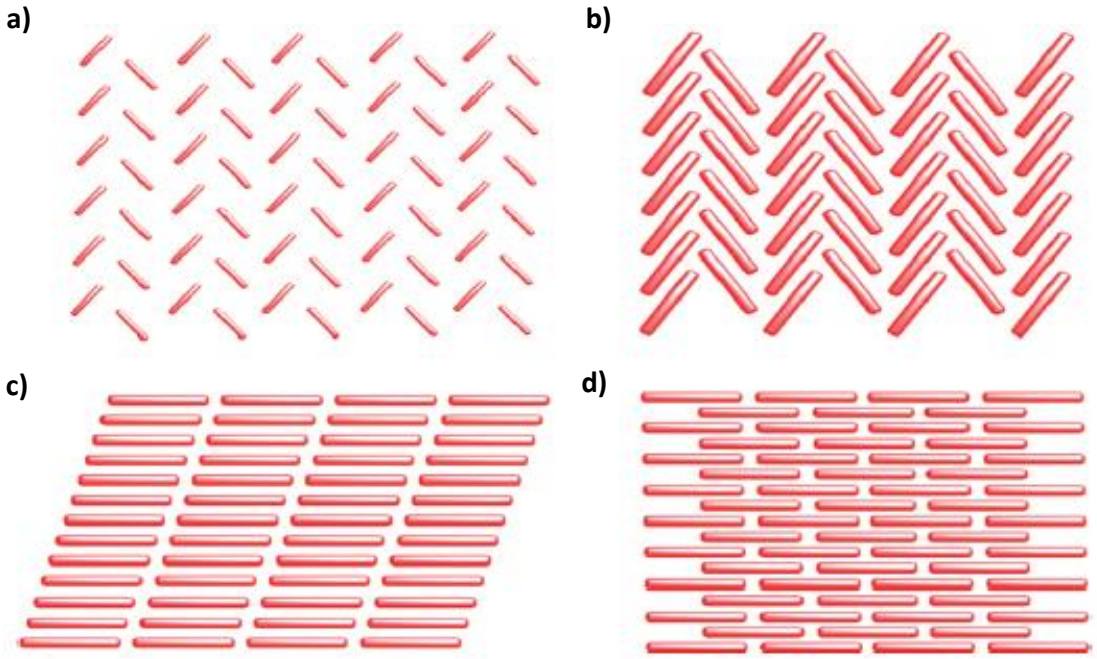

Figure 4.1. Different types of molecular packing models in organic semiconducting systems. a) Herringbone packing (face-to-edge) without π-π overlap, b) herringbone packing with π-π overlap, c) lamellar packing motif, 1D π-stacking and d) lamellar packing motif, 2D π-stacking.

There are mainly four different kinds of molecular packing; (i) herringbone packing without π-π overlap between adjacent π-conjugated systems; (ii) herringbone packing with π-π overlap between adjacent molecules (slipped π-stacking); (iii) one-dimension (1D) π-stacking, and (iv) two-dimensional (2D) π-stacking (Figure 4.1).[1] Among the four kinds of packing motifs, that of 2D π-stacking is believed to be the most efficient for charge transport because it can increase the transfer integrals to the maximum and transport the charge carriers through a shortest pathway. Ideally for the

efficient charge transport, the organic molecules should pack along the current direction in the conducting channel. Hence in high performance organic field-effect transistors semiconducting molecules usually adopt an edge-on orientation.[1,11]

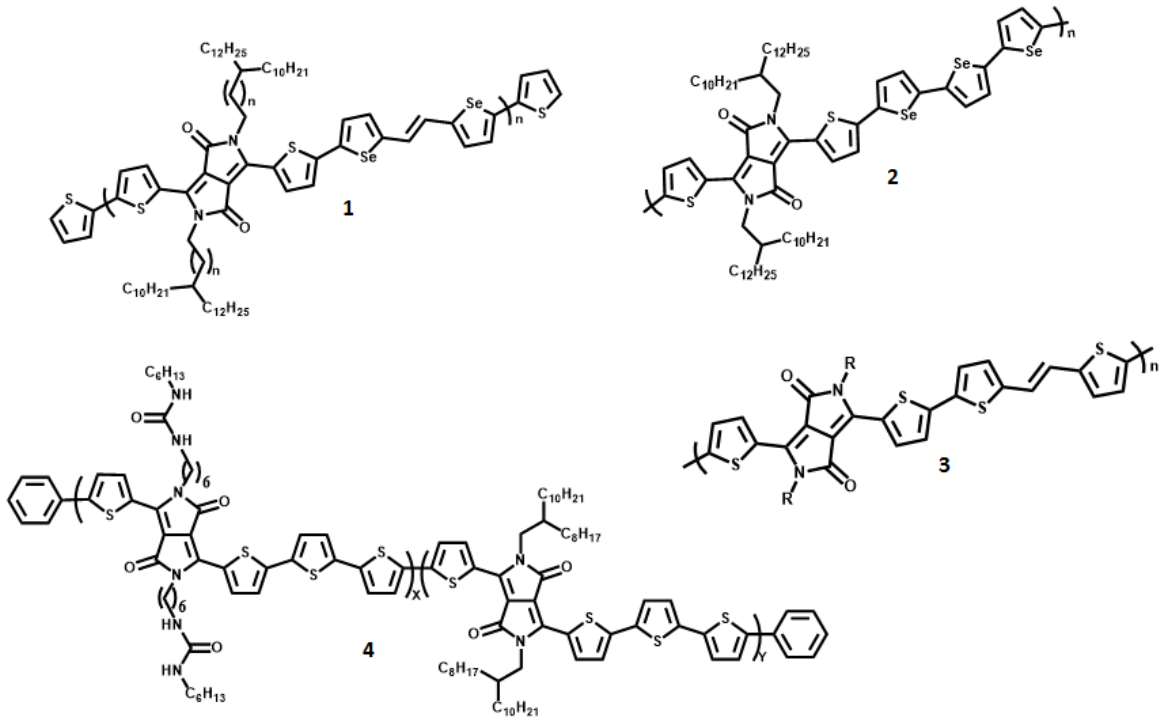

Figure 4.2. Chemical structures of highly efficient DPP-based donor-acceptor semiconducting polymers.

Inter- as well as intramolecular interactions among the polymer chains increase the self-assembling ability of the semiconductors which in turn enhances the π-π overlap of adjacent monomer units.[26-29] Conjugated polymers with alternate donor-acceptor (D-A) units is a widely adopted choice in this regard.[4,30-32] Among the various electron-deficient π-conjugated systems, diketopyrrolopyrrole (DPP) occupies a unique position for the construction of numerous efficient semiconducting materials for OFET applications.[33-39] Low band gap polymers having good charge carrier

mobility can be made by the proper functionalization of DPP with suitable electron-rich systems (Figure 4.2).[23,40-44] Among the vast number of polymer semiconductors, DPP-based polymers exhibit high mobility above 1 $cm^2V^{-1}s^{-1}$. Kim et al. have reported highly efficient semiconducting polymers based on DPP showing high charge carrier mobility which can compete with the performance of amorphous silicon.[40]

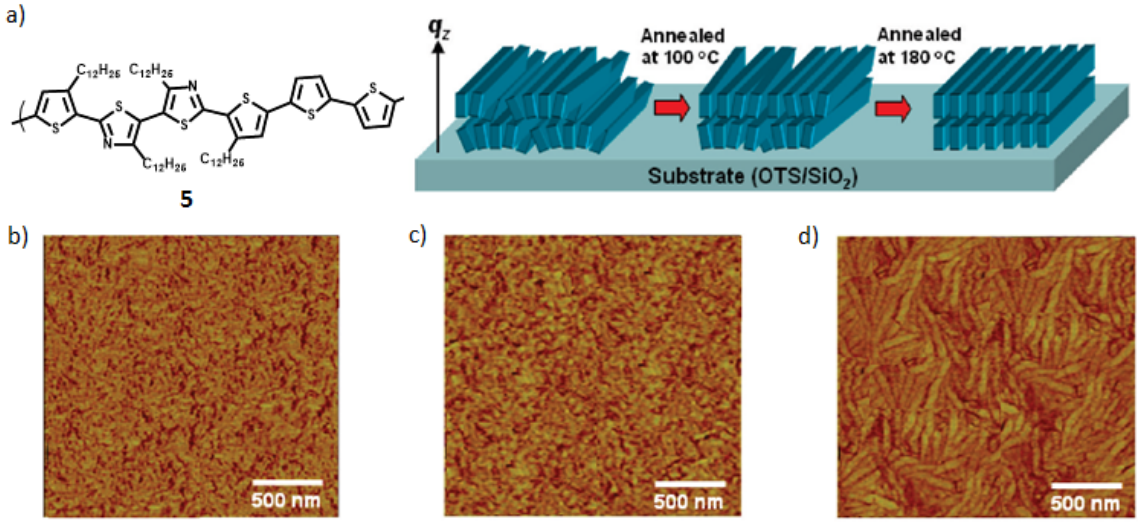

Figure 4.3. a) Chemical structure of polymer (**5**) and schematic representation of the polymer domains in the thin film at various annealing temperatures. AFM images of the polymer thin films spin-coated onto the octadecyltrimethoxysilane treated SiO_2 substrates for various annealing temperatures; b) as-spun, c) 100 °C and d) 180 °C.

Improved degree of ordered molecular packing can facilitate the charge carrier mobility by reducing the reorganization energy and increasing the transfer integral.[21,22] Lee et al. have demonstrated bottom-up assembly of the semiconducting

copolymer (**5**) based on electron-donating quaterthiophene and electron accepting 5,5′-bithiazole units for facile fabrication of highly ordered conducting channel with remarkable electrical stability (Figure 4.3). Thermal annealing of the polymer films leads to self-organization of individual polymer chains with nanostructural anisotropy. This can be ascribed due to the intermolecular interactions in the liquid-crystalline mesophase which form highly ordered semiconducting channel with a minimal concentration of charge traps.[45]

Heteroatom substitution of the aromatic core has a huge influence on the electronic properties as well as crystal packing. Incorporation of π-conjugated fused heteroarenes into the polymer backbone is another approach to enhance conjugation length and the intermolecular π-overlap.[26,46] Among the fused aromatic rings sulfur containing derivatives exhibit excellent OFET performance.[47,48] This can be explained by the ability of sulfur atoms to introduce S•••H, S•••S, and S•••π intermolecular interactions which enhance intermolecular packing. Hence, many thiophene-based organic semiconductors, including π-extended oligothiophenes and fused-thiophene compounds (thienoacenes) have been developed and examined as the active material for OFETs. DeLongchamp et al. have demonstrated the influence of incorporation of thienothiophene on the nature of molecular packing of DPP based donor-acceptor polymer (Figure 4.4).[49]

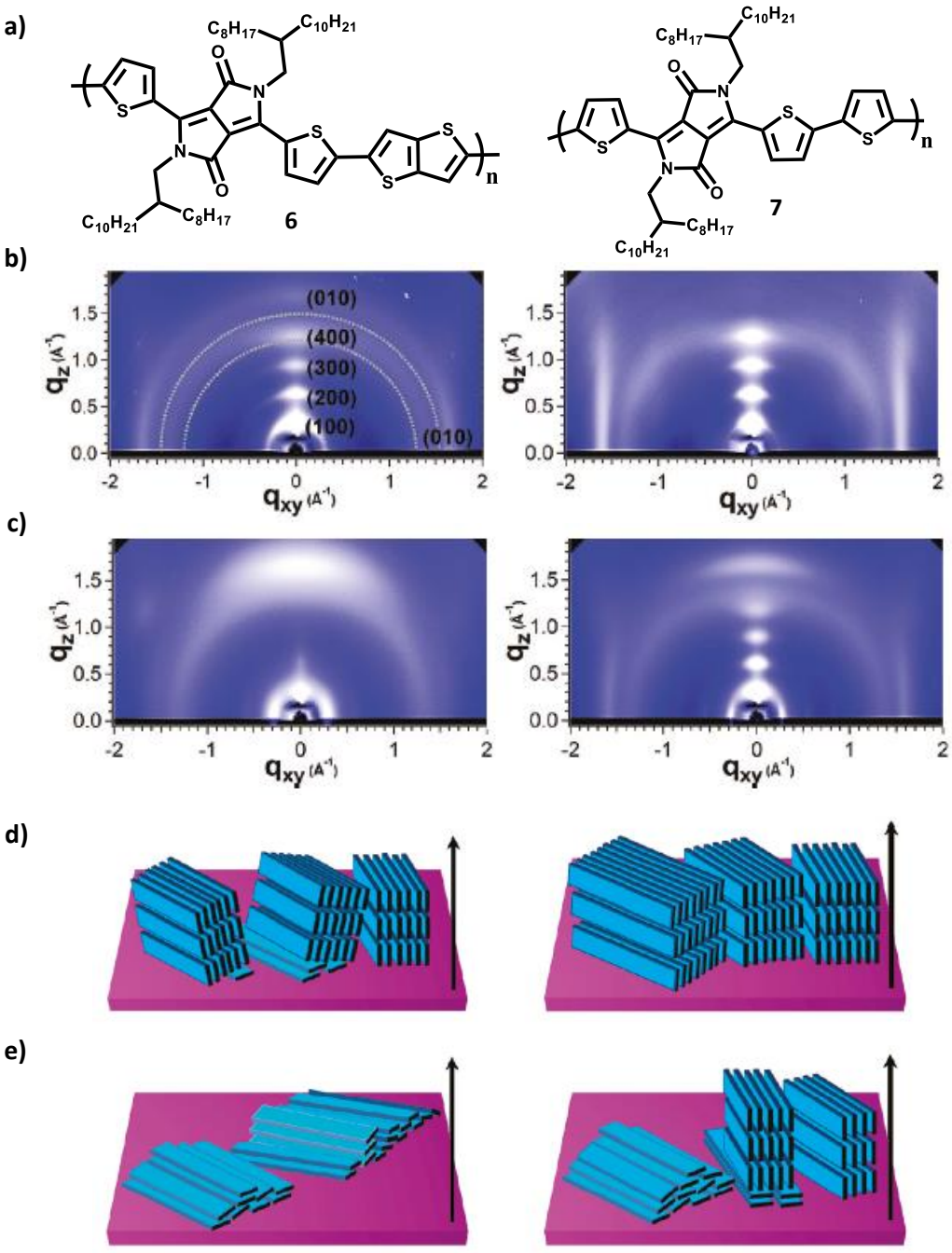

Figure 4.4. a) Chemical structures of polymers (**6** and **7**). Two-dimensional grazing incidence X-ray diffraction (GIXRD) from thin films of b) **6** as-spun (left) and annealed (right) and c) **7** as-spun (left) and annealed (right). Schematic illustration of the molecular packing of d) **6** and e) **7** [as-spun (left) and annealed (right)].

The molecular packing behavior of **6** shows lamellar packing motif with mixture of edge-on and face-on conjugated planes of the backbone. Face-on population and the misoriented edge-on domains are significantly reduced by the thermal annealing. The backbone organization of DPP-thiophene polymer (**7**) film is remarkably different from DPP-thienothiophene (**6**) based polymers, which highlight the importance of local ring co-planarity of thienothiophene units. Edge-on backbone orientation ensures the effective percolation pathways for charge transport across the length of OFET channel. [1]-Benzothieno[3,2-*b*]benzothiophene (BTBT) is one of the promising fused chalcogenophenes used for the OFET applications. Efficient field effect mobility of BTBT derivatives has been well established in small molecule based OFETs.[50-54] BTBT possess appropriate HOMO spatial distribution for effective intermolecular orbital overlap. It has been proved that BTBT based semiconducting materials mostly yield transistors with excellent charge carrier mobility regardless of the molecular dimension or the chemical substitution of the aromatic core.[55]

In most of the cases, molecular arrangement of BTBT in semiconducting layer is identified as the herringbone structure. Molecules can pack in two ways namely edge-to-edge pairs (stacking pair) and edge-to-face pairs. Sulfur atoms in the thienothiophene moiety can not only make effective intermolecular interaction, but also can lead to effective intermolecular HOMO overlap. These effects result in the large intermolecular transfer integrals ($t_{stacking}$), effective HOMO overlap in the edge-to-face molecular pairs ($t_{transverse}$) and two-dimensional (2D) electronic structure is realized in the semiconducting channel (Figure 4.5).

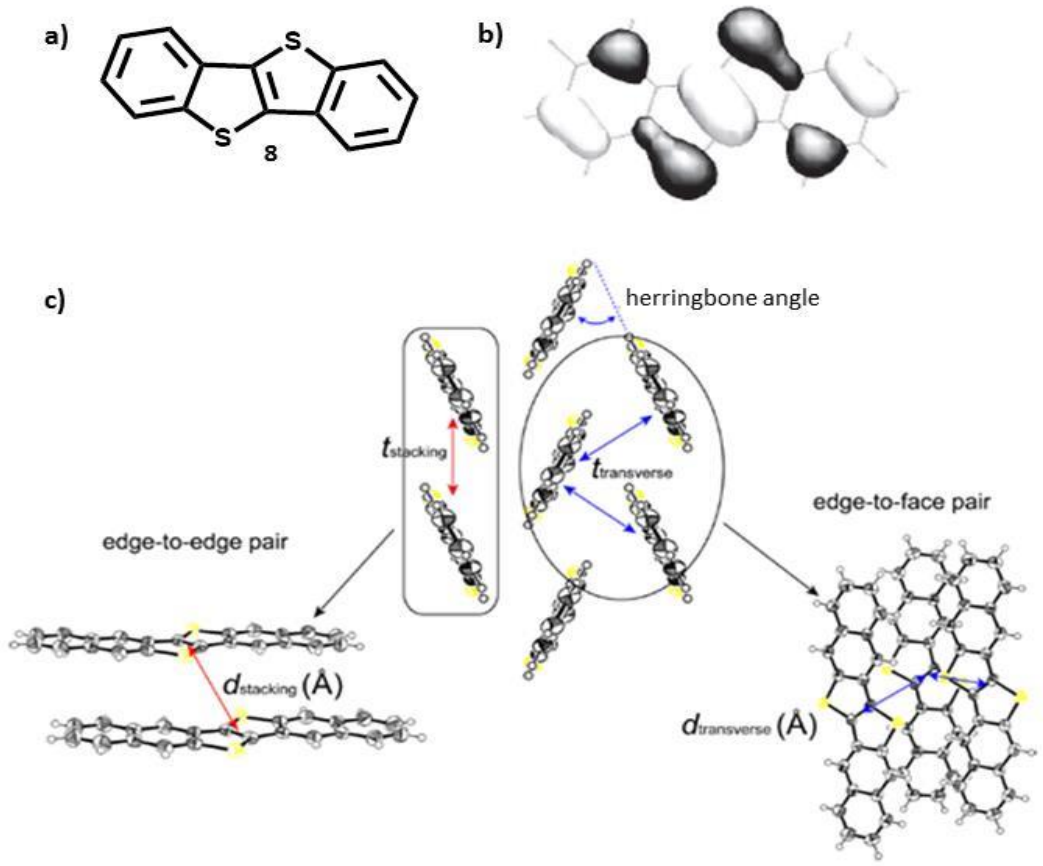

Figure 4.5. a) Chemical structure of BTBT core (**8**). b) Spatial distributions of HOMO and contribution of sulfur atoms to HOMO. c) Molecular arrangement and packing fashion of BTBT-cores in the solid state (Intermolecular distance and transfer integrals are shown for both edge-to-edge pair and edge-to-face pair).

Takimiya et al. have reported the synthesis of 2,7-diphenyl[1]benzothieno[3,2-*b*][1]-benzothiophene (DPh-BTBT), the fabrication of its evaporated thin-film-based OFET, and the excellent FET characteristics in air.[50] Molecular arrangement of DPh-BTBT is nearly perpendicular to the substrate and is independent of the various surface treatments as well as substrate temperatures. All the devices constructed from DPh-BTBT showed typical *p*-channel field effect transistor characteristics in ambient

conditions with mobilities of ~ 2.0 $cm^2V^{-1}s^{-1}$ and $I_{on/off}$ of 10^7 (Figure 4.6). Same research group has reported solution-processable organic semiconductors based on the BTBT core structure, in which two solubilizing long alkyl groups are introduced in the molecular long-axis direction of the core to facilitate lateral intermolecular interaction (Figure 4.6b).[51] Irrespective of the length of the alkyl chain length, the BTBT derivatives showed similar molecular packing behavior. Regardless of the structural dissimilarity, thin films of BTBT derivatives acted as a superior *p*-type semiconducting channel and μ_{FET} of the devices was > 0.1 $cm^2V^{-1}s^{-1}$.

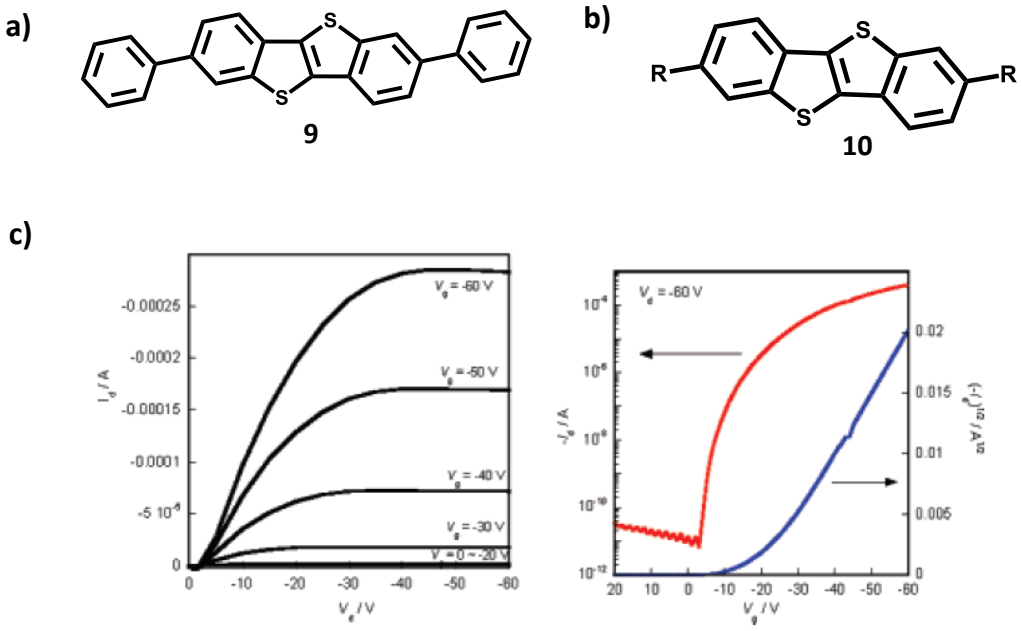

Figure 4.6. a,b) Molecular structures of BTBT derivatives (**9** and **10**) used for the OFET applications. c) FET characteristics of devices constructed from **9**. Output characteristics (left) and transfer characteristics at V_{DS} = -60 V (right).

Hasegawa et al. demonstrated a technique of antisolvent crystallization with inkjet printing to produce organic semiconducting thin films of high crystalline 2,7-dioctyl[1]benzothieno[3,2-*b*][1]benzothiophene.[52] Thin-film transistors constructed

by this method showed average carrier mobility as high as 16.4 $cm^2V^{-1}s^{-1}$. However, there are not many reports on the efficient semiconducting polymers based on BTBT due to the limited solubility of BTBT core.[56]

Herein we report three-component random D-A copolymers having different percentage of DPP and BTBT units in the polymer backbone (Scheme 4.1). A strategy to incorporate BTBT in conjugated D-A polymers is to replace partially the electron donors in the backbones with BTBT to generate three component conjugated polymers. In order to understand the structure-property relationship of the polymer materials, the percentage composition of BTBT unit in the polymer chain is varied as 5%, 10%, and 20%. Irrespective of the structural composition of the backbone, all these low band gap polymers exhibit *p*-type semiconducting behavior. With the higher proportion of rigid planar BTBT unit in conjugated π-backbone, the degree of molecular packing in the polymer thin films increases, ultimately leading to high charge carrier mobilities (μ_h) up to 2.47 $cm^2V^{-1}s^{-1}$.

4.3. Results and Discussion

4.3.1. The Design Strategy

The monomers and polymers were synthesized according to the reported experimental procedures (Scheme 4.2 and Scheme 4.3).[35,38,57] Stille coupling was carried out between 3,6-dibromothiophen-2-yl-*N*,*N*-bis(2-octyldodecyl)-1,4-dioxopyrrolo [3,4-*c*]pyrrole, 2,7-diiodo[1]benzothieno[3,2-*b*]benzothiophene, and respective bis-stannylated derivatives of heteroarenes in the presence of $Pd_2(dba)_3$ (dba = dibenzylideneacetone) and the active ligand P(*o*-tol)$_3$ in nitrogen atmosphere.

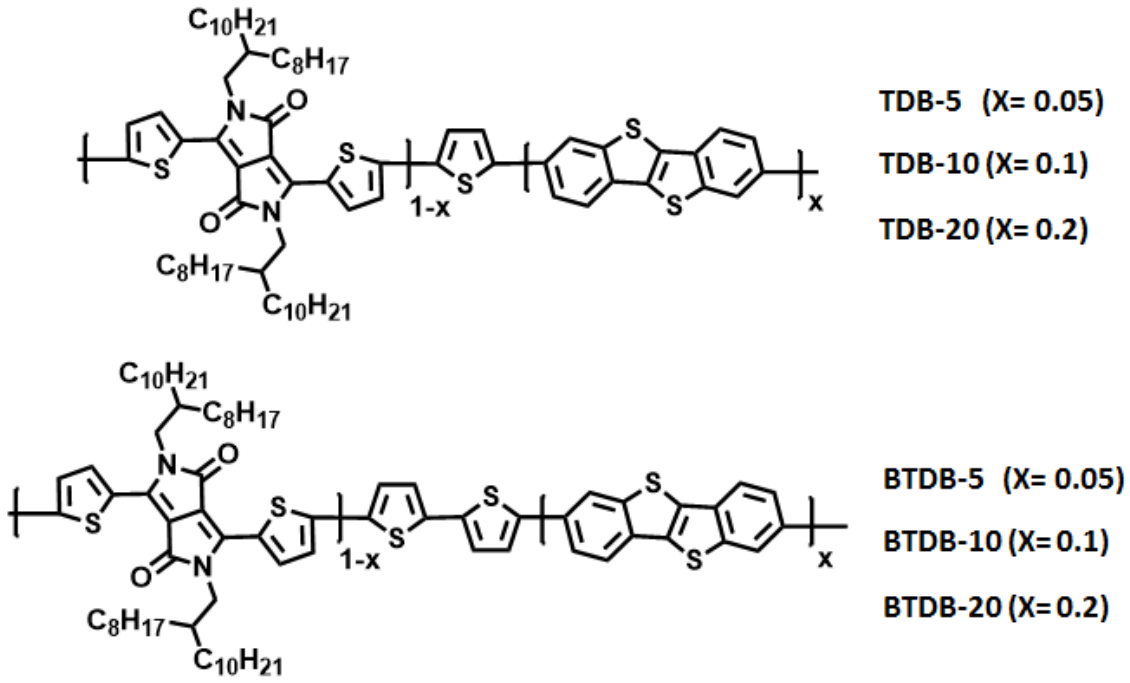

Scheme 4. 1. Chemical structures of polymers **TDB**s and **BTDB**s.

The resulting polymers were subjected to Soxhlet extraction using methanol, acetone, *n*-hexane, and chloroform sequentially to remove the monomers and oligomers and other impurities. The percentage composition of BTBT monomer in the polymer chain was estimated based on the elemental analysis data. Polymers were then characterized by high-temperature gel permeation chromatography (GPC) with 1,2,4-trichlorobenzene as eluent and polystyrene as standard at 150 °C. The molecular weights of all six polymers and the respective polydispersity indices are listed in Table 4.1

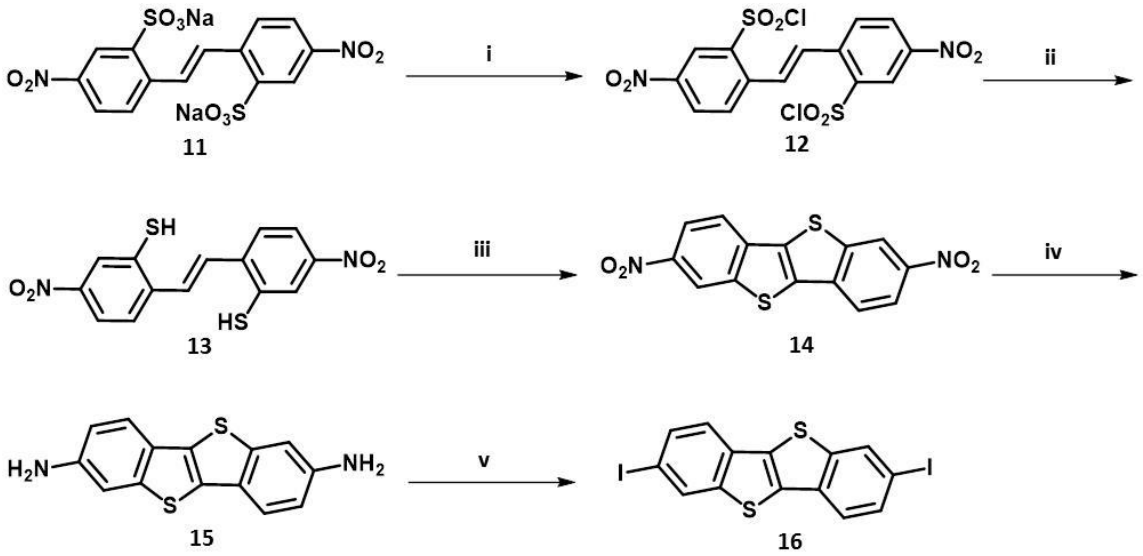

Scheme 4.2. Reagents and conditions: i) PCl_5, 120 ^oC, 2 h, ii) 55 % HI, acetic acid, 20 ^oC, 12 h, iii) Br_2, acetic acid, 2 h, iv) Sn, con.HCl, acetic acid and v) $NaNO_2$, con.H_2SO_4, KI, 0-5 ^oC, ethanol.

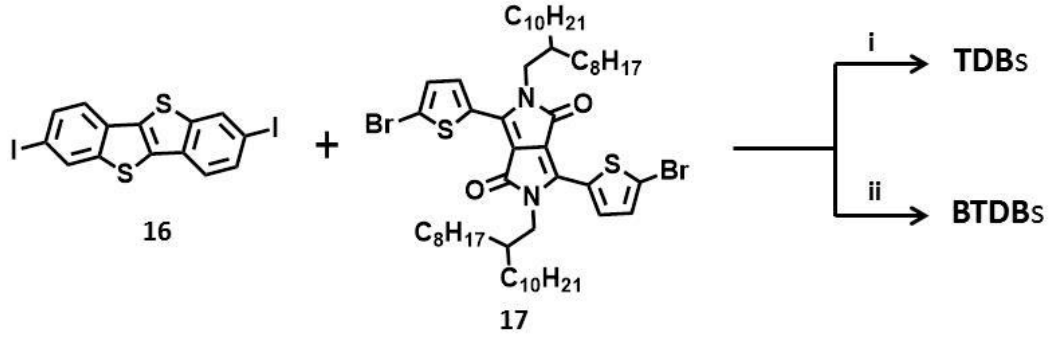

Scheme 4.3. Reagents and conditions: i) 2,5-bis(trimethylstannyl)thiophene, $Pd_2(dba)_3$, P(*o*-tol)$_3$, 90 ^oC, 48 h and ii) 5,5'-bis(trimethylstannyl)-2,2'-bithiophene, $Pd_2(dba)_3$, P(*o*-tol)$_3$, 90 ^oC, 48 h.

Table 4.1. Optical and Electrochemical Properties of TDBs and BTDBs

Polymer	λ_{max} (nm)		HOMO[a]	LUMO[a]	ΔE_g^{CV}	ΔE_{op}[b]	M_n/M_w	PDI
	Solution	Film	(eV)	(eV)	(eV)	(eV)	(Kg mol^{-1})	
TDB-5	785	747, 808	-5.17	-3.79	1.38	1.32	43/130	3.0
TDB-10	790	793	-5.17	-3.82	1.35	1.32	38/127	3.3
TDB-20	759, 806	757, 820	-5.16	-3.80	1.36	1.31	46/140	3.0
BTDB-5	777	788	-5.22	-3.74	1.48	1.34	38/103	2.7
BTDB-10	723, 789	727, 800	-5.09	-3.76	1.33	1.33	64/240	3.8
BTDB-20	720, 780	743, 807	-5.08	-3.79	1.30	1.31	51.3/230	4.5

[a]Estimated from the onset of oxidation and reduction potential of cyclic voltammogram using the following equations: LUMO = -(E_{red}^{onset} + 4.4) eV; HOMO = -(E_{ox}^{onset} + 4.4) eV. [b]Calculated from the onset of thin film state absorption spectra.

Among the polymers, **TDB-20** and **BTDB-10** show high number average molecular weight (M_n) and weight-average molecular weight (M_w), and the polydispersity indices of the polymers are varied from 2.7 to 4.5. Thermogravimetric analysis was carried out to understand the thermal stability of the polymers. Figure 4.7 illustrates the absence of any characteristic phase transitions and all the polymers are quite stable up to 350 °C.

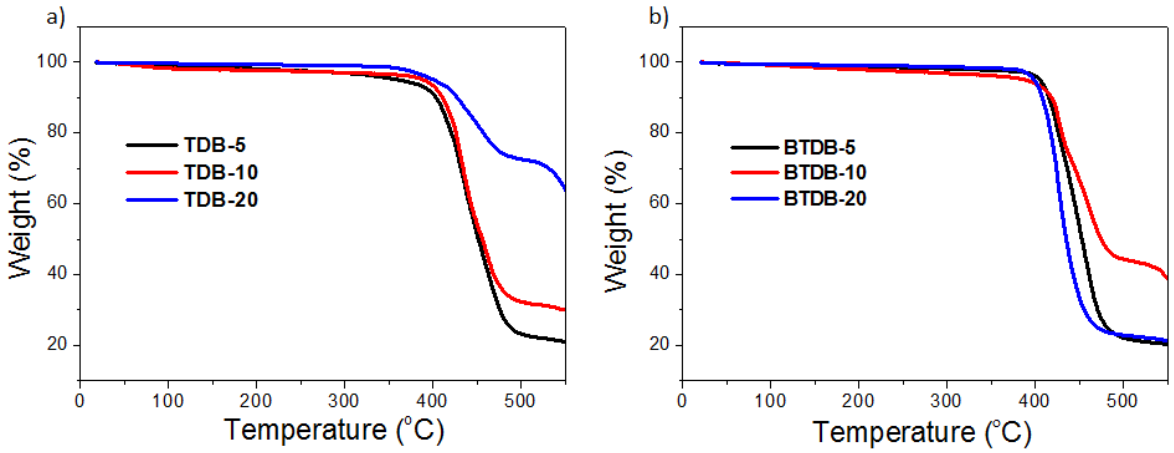

Figure 4.7. TGA curves of a) **TDB**s and b) **BTDB**s.

4.3.2. Optical and Electrochemical Properties

UV-vis absorption spectra of **TDB**s were recorded in solution state and film state (Figure 4.8). Irrespective of the aromatic backbone composition, all the polymers showed dual band absorptions.[58,59] A less intense π-π* band was observed at the shorter wavelength region, and an intense intramolecular charge transfer band was observed at longer wavelength region. Figure 4.8a illustrates a slight red-shift in the solution state absorption with increase in the ratio of BTBT unit. Whereas, film state absorption spectra showed a substantial bathochromic shift (≈ 70 nm) with the rise in the percentage composition of BTBT core in the polymer backbone (Figure 4.8b). This significant red-shift in the film state absorption spectra of **TDB**s implies the presence of strong inter- as well as intramolecular D-A interactions among the polymer chains.[60]

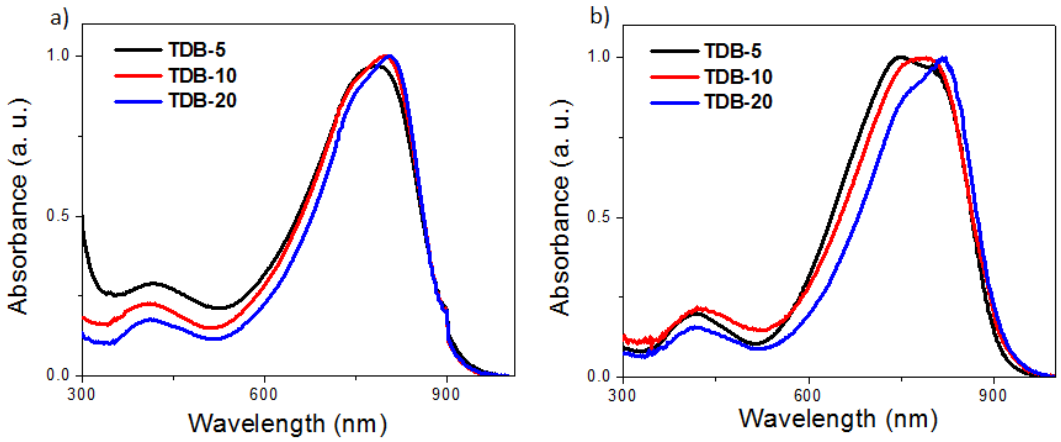

Figure 4.8. UV-vis absorption spectra of **TDB**s in a) solution state and b) film state.

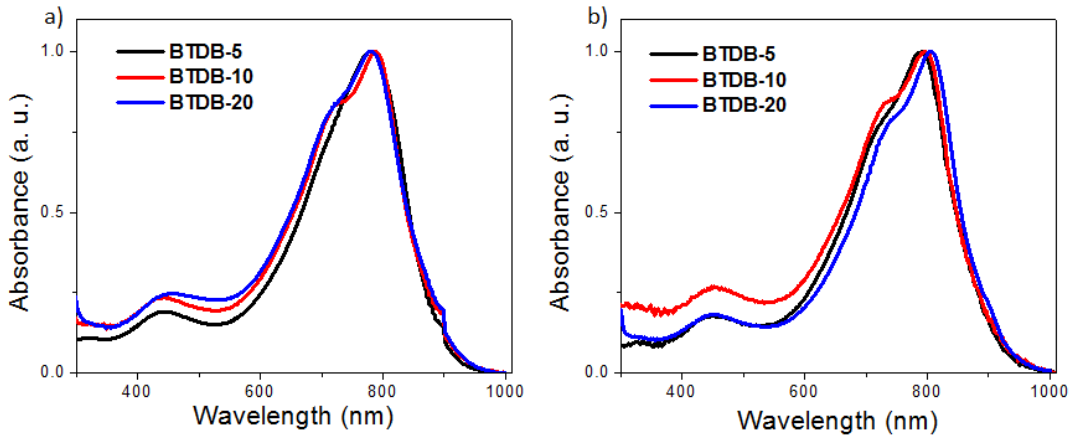

Figure 4.9. UV-vis absorption spectra of **BTDB**s in a) solution state and b) film state.

In solution and film states, **BTDB**s display absorption onset approximately at 950 nm (Figure 4.9). Except **BTDB-5** (≈ 1.5 eV), all polymers showed optical band gap of < 1.4 eV which may be due to the efficient intramolecular charge transfer (Table 4.1).[11,61,62] Relatively higher bandgap of **BTDB-5** may be ascribed to the defect in the random polymerization. Energy levels of frontier molecular orbitals

were determined by carrying out the cyclic voltammetry of all the polymers in the film state (Figure 4.10).

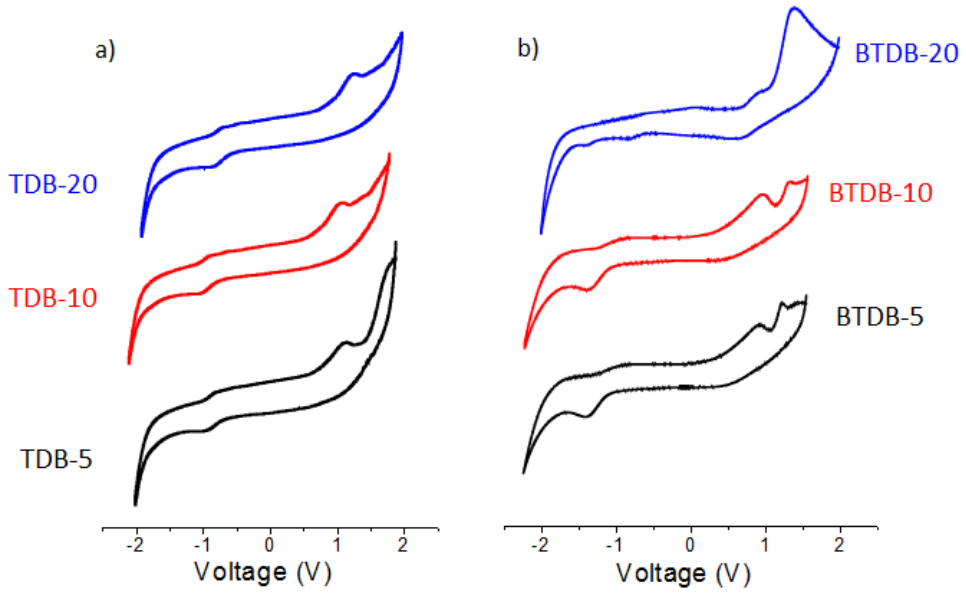

Figure 4.10. Cyclic voltamogram of polymers **TDB**s and **BTDB**s in film state. The films were prepared by drop-casting polymer solution in *o*-DCB with a concentration of 3 mg/mL.

Energy levels of HOMO and LUMO were calculated from the onset of oxidation potential and reduction potential respectively (Table 4.1). Molecular orbitals have a crucial role in deciding the semiconducting behavior of polymers. Insertion of planar fused chalcogenophene is expected to enhance the delocalization of the HOMO throughout the polymer backbone by improving the π-conjugation.[30]

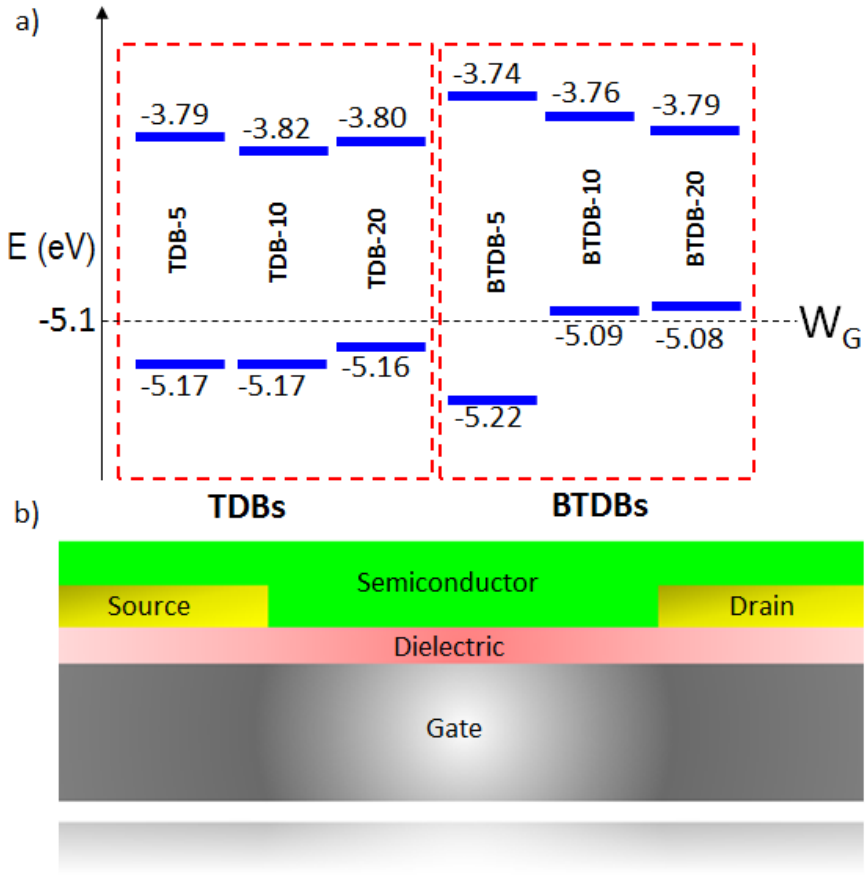

Figure 4.11. a) Energy level diagram of the polymers with respect to work function of gold (W_G) (Upper and lower values represent LUMO and HOMO, respectively). b) Schematic diagram of bottom gate-bottom contact (BG/BC) OFET architecture.

Energy levels of HOMOs were increased by increasing the BTBT amount in both **TDB**s and **BTDB**s copolymers whereas the energy levels of LUMOs were decreased. For example, **BTDB-5** showed deepest lying HOMO (-5.22 eV), whereas energy levels of orbitals raised to -5.09 and -5.08 eV for **BTDB-10** and **BTDB-20**, respectively. LUMO of **BTDB-5** was calculated to be -3.74 eV, and it decreased to -3.76 and -3.79 eV for **BTDB-10** and **BTDB-20**, respectively (Figure 4.11). Incorporation of BTBT units in the backbones enhances the HOMO levels which are

close to the work function of Au. Such HOMO energetic engineering will benefit the hole injection and thus improve field effect properties according to previous reports.[63]

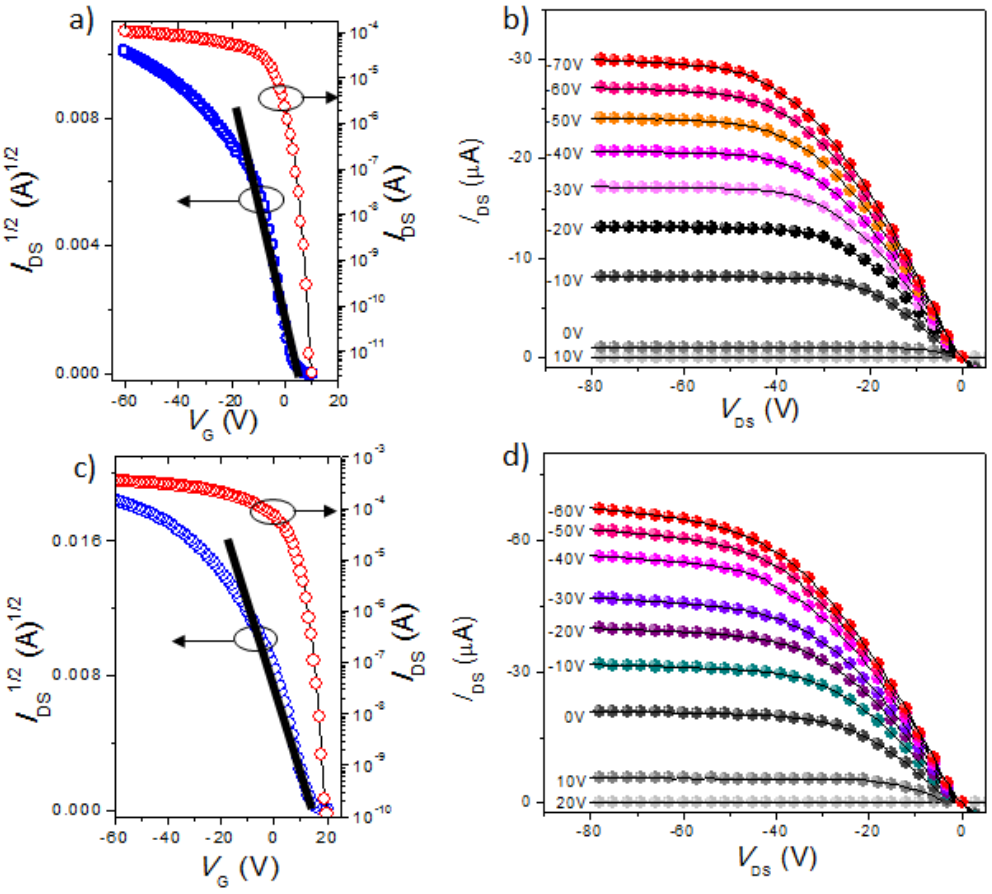

Figure 4.12. a, c) Transfer (V_{DS} = -60 V) and b, d) output characteristics of OFETs from thin films of (a, b) **TDB-20** and (c, d) **BTDB-20** after thermal annealing at 100 °C [Channel length (L) and width (W) were 50 and 1400 μm, respectively].

These results indicate that the HOMO levels decrease while the LUMO levels increase by the incorporation of BTBT units in the backbones. However, it is expected that the presence of BTBT in the conjugated backbone can prolong the

conjugation length as the BTBT is a larger conjugated moiety than thiophene or bithiophene.

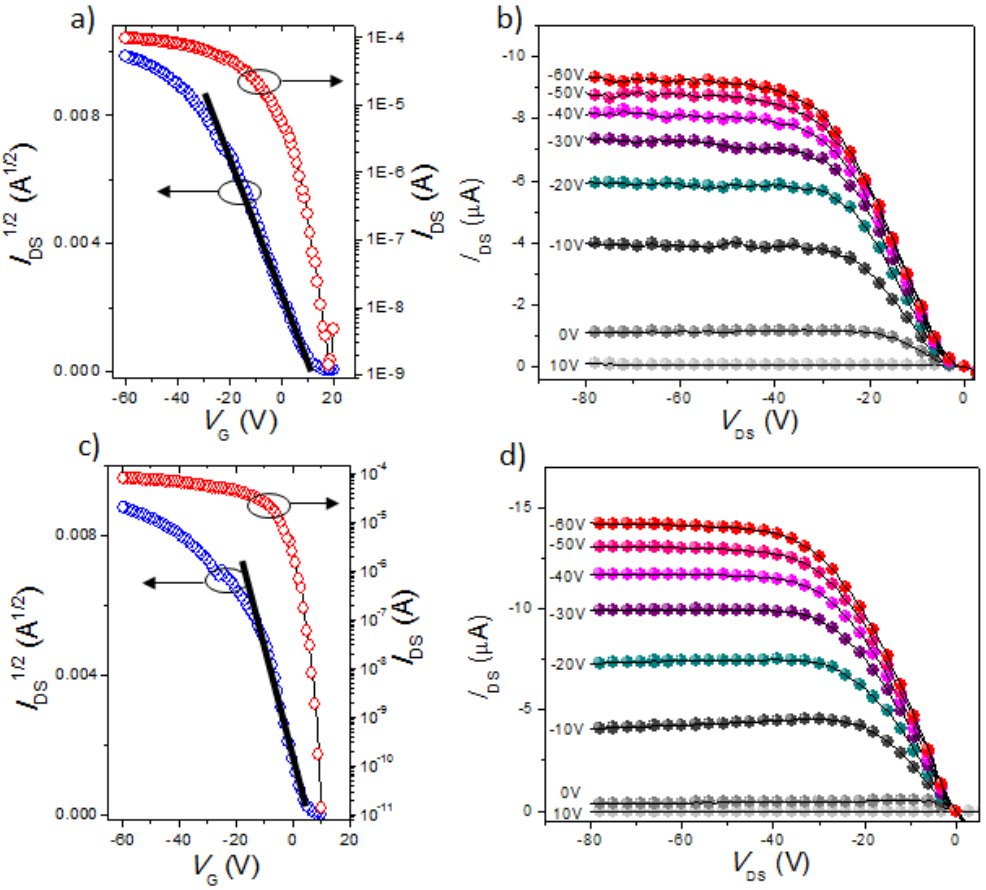

Figure 4.13. a, c) Transfer (V_{DS} = -60 V) and b, d) output characteristics of OFETs from thin films of (a, b) **TDB-5** and (c, d) **TDB-10** after thermal annealing at 100 °C [Channel length (L) and width (W) were 50 μm and 1400 μm, respectively].

4.3.3. Field-Effect Transistor Measurements

Thin films of these polymers were used to fabricate the BG/BC (bottom gate/bottom contact) FETs with gold as source/drain electrodes (Figure 4.11b). The measurements were carried out in ambient conditions. Figure 4.12 shows the transfer and output curves of FETs with thin films of **TDB-20** and **BTDB-20** after thermal annealing at

100 °C, and those of with thermally annealed thin films of **TDB-5**, **TDB-10**, **BTDB-5**, and **BTDB-10** are displayed in Figure 4.13 and Figure 4.14.

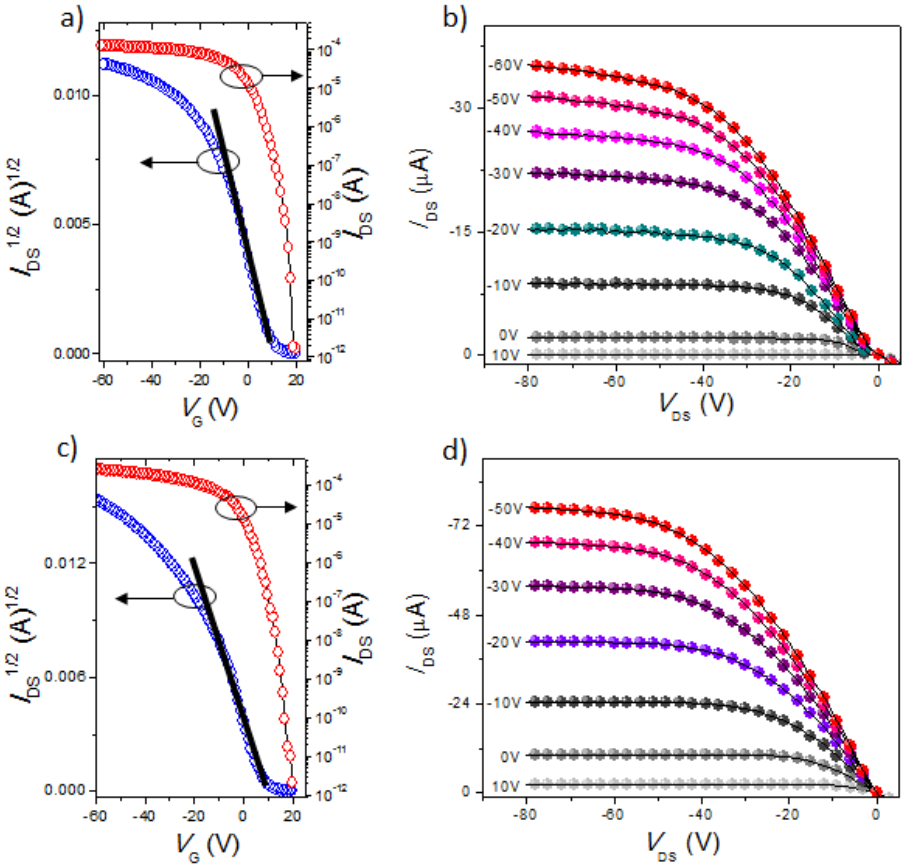

Figure 4.14. a, c) Transfer (V_{DS} = -60 V) and b, d) output characteristics of OFETs from thin films of (a, b) **BTDB-5** and (c, d) **BTDB-10** after thermal annealing at 100 °C [Channel length (L) and width (W) were 50 μm and 1400 μm, respectively].

The output and transfer curves reveal that all six polymers exhibit *p*-type semiconducting behavior. We notice that the plots of $I_{DS}^{1/2}$ vs V_G are linear at low gate voltage and become deviated from the linear relations at high gate voltage. Similar non-ideal electrical characteristics have been reported for DPP-based conjugated D-A polymers, and its origins are not clearly understood.[3, 23, 31, 64-66] Such

non-ideal electrical behaviors lead to the dependence of charge mobility on the gate voltage as illustrated in Figure 4.15. For comparing the semiconducting performances of these six polymers, we estimate their hole mobilities by fitting the linear regions of the respective plots of $I_{DS}^{1/2}$ vs V_G. The respective device characteristics are listed in Table 4.2 and Table 4.3.

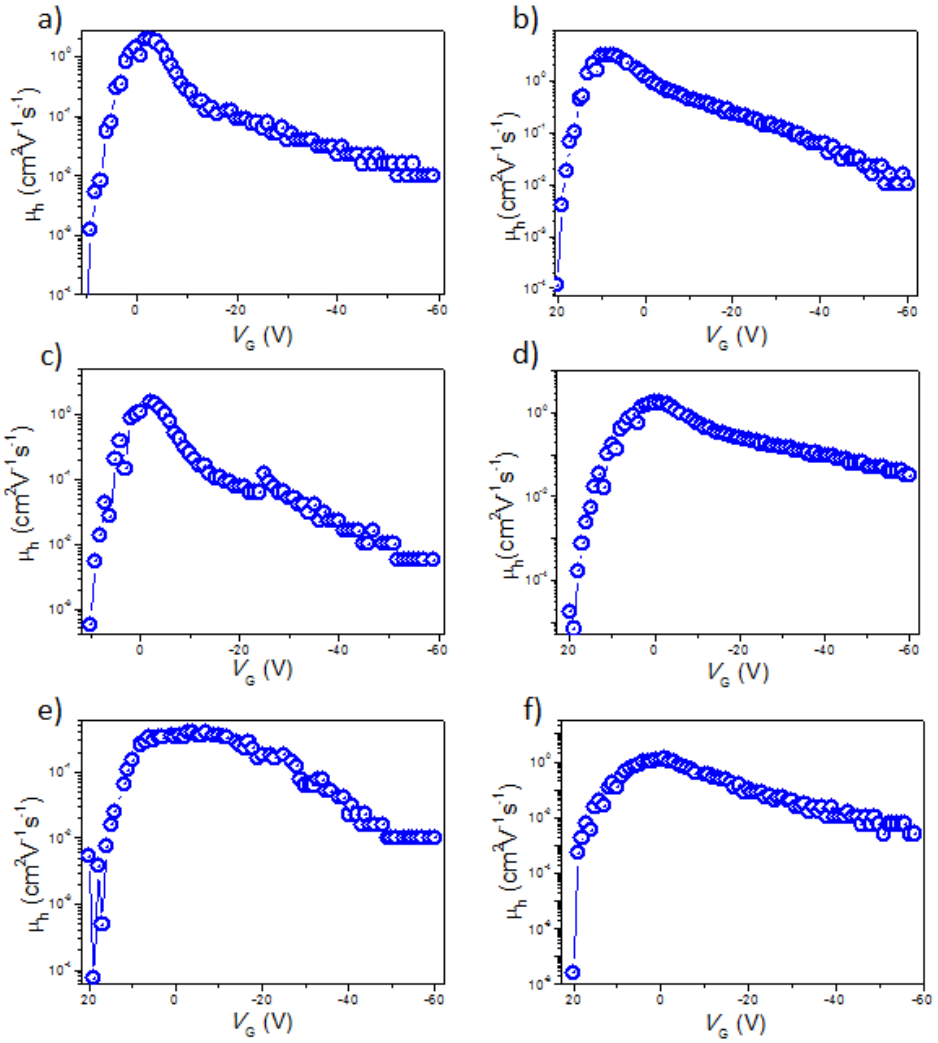

Figure 4.15. Mobilities (μ_h) as a function of gate voltage (V_G) a) **TDB-20**, c) **TDB-10**, e) **TDB-5**, b) **BTDB-20**, d) **BTDB-10**, f) **BTDB-5**.

For each polymer, the hole mobility increased after thermal annealing. For instance, hole mobility of **TDB-20** was enhanced from 0.34 $cm^2V^{-1}s^{-1}$ for the as-prepared thin film to 1.47 $cm^2V^{-1}s^{-1}$ after thermal annealing at 100 °C. But, hole mobility started to decrease after increasing the annealing temperature to 120 °C (Table 4.2).

Table 4.2. Hole Mobilities (μ_h), Threshold Voltage (V_{th}), $I_{on/off}$ of OFET Devices from Polymers on OTS-modified SiO_2/Si Substrates and Gold Electrodes at Different Annealing Temperatures.

Polymer	Temperature (°C)	μ_h [a] ($cm^2V^{-1}s^{-1}$)	V_{th} (V)	$I_{on/off}$
TDB-5	RT	0.09/0.06	10-15V	10^5-10^6
	80	0.17/0.13	10-15V	10^5-10^6
	100	0.35/0.28	10-15V	10^5-10^6
	120	0.21/0.18	10-15V	10^5-10^6
TDB-10	RT	0.21/0.14	5-10V	10^5-10^6
	80	0.41/0.38	5-10V	10^5-10^6
	100	0.92/0.73	5-10V	10^5-10^6
	120	0.70/0.65	5-10V	10^5-10^6
TDB-20	RT	0.34/0.31	5-10V	10^5-10^6
	80	0.88/0.78	5-10V	10^5-10^6
	100	1.47/0.99	5-10V	10^5-10^6
	120	1.02/0.92	5-10V	10^5-10^6

[a]Data were obtained based on the performance of more than 20 different FETs, and presented in "highest/average" form.

Table 4.3. Hole Mobilities (μ_h), Threshold Voltage (V_{th}), $I_{on/off}$ of OFET Devices from Polymers on OTS-modified SiO_2/Si Substrates and Gold Electrodes at Different Annealing Temperatures.

Polymer	Temperature (°C)	μ_h [a] ($cm^2V^{-1}s^{-1}$)	V_{th} (V)	$I_{on/off}$
BTDB-5	RT	0.48/0.37	10-20V	10^6-10^7
	80	0.76/0.67	10-20V	10^6-10^7
	100	1.04/0.87	10-20V	10^6-10^7
	120	0.90/0.80	10-20V	10^6-10^7
BTDB-10	RT	0.78/0.64	10-20V	10^6-10^7
	80	1.24/0.91	10-20V	10^6-10^7
	100	1.64/1.37	10-20V	10^6-10^7
	120	1.43/1.18	10-20V	10^6-10^7
BTDB-20	RT	0.99/0.88	10-20V	10^5-10^6
	80	1.78/1.37	10-20V	10^5-10^6
	100	2.47/1.66	10-20V	10^5-10^6
	120	2.17/1.48	10-20V	10^5-10^6

[a]Data were obtained based on the performance of more than 20 different FETs, and presented in "highest/average'' form.

The highest hole mobilities were found to be 0.35, 0.92, and 1.47 $cm^2V^{-1}s^{-1}$ for **TDB-5**, **TDB-10**, and **TDB-20**, respectively, whereas those of **BTDB-5**, **BTDB-10**, and **BTDB-20** were 1.04, 1.64, and 2.47 $cm^2V^{-1}s^{-1}$, respectively, after thermal annealing at 100 °C. The highest mobility was obtained for **BTDB-20** (2.47 $cm^2V^{-1}s^{-1}$) after thermal annealing (Table 4.3).[46,49] These data show that (i) hole mobility is enhanced by incorporating more BTBT in the conjugated backbones of these polymers and (ii) the polymers with bithiophene as electron donor display higher hole mobility than those containing thiophene as the electron donor. These are

understandable by considering the fact that the rigid, planar, and large conjugated moieties such as [1]benzothieno[3,2-*b*]benzothiophene in the backbones of polymers are favorable for interchain π-π interactions and thus beneficial for charge transporting.[55,67]

4.3.4. GIXRD and AFM Studies

Thin films of these conjugated polymers were characterized with GIXRD (grazing-incidence X-ray diffraction) and AFM techniques. Figure 4.16 shows the out-of plane and in-plane diffraction patterns of the thermally annealed thin films of **TDB**s. In the out-of-plane direction, thin films of **TDB-5**, **TDB-10**, and **TDB-20** exhibit a diffraction at q_z = 0.31 Å^{-1}, corresponding to a *d*-spacing of ~ 20.3 Å and an additional diffraction signal at q_z = 1.79 Å^{-1}, corresponding to a *d*-spacing of ~ 3.5 Å emerges for **TDB-10** and **TDB-20** as depicted in Figure 4.16a.

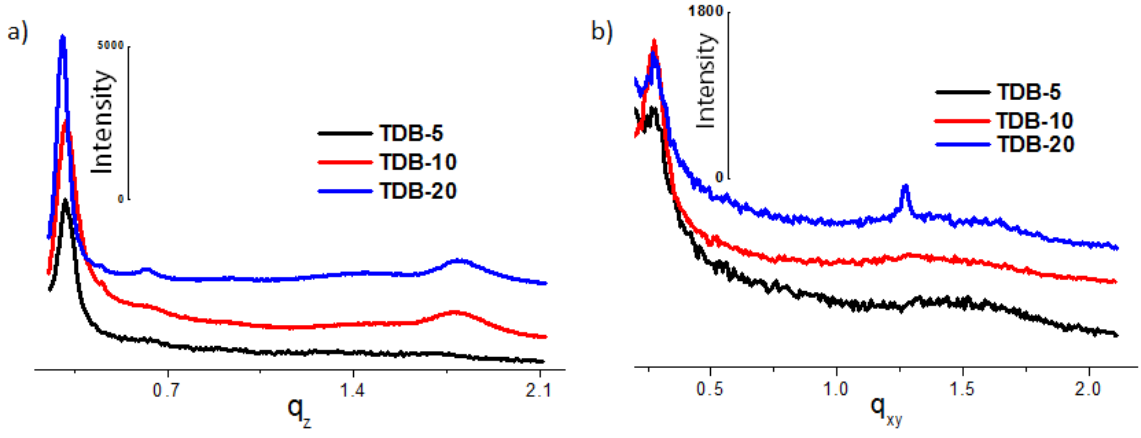

Figure 4.16. 1D GIXRD patterns of the annealed thin films of **TDB**s. a) Out-of-plane and b) in-plane.

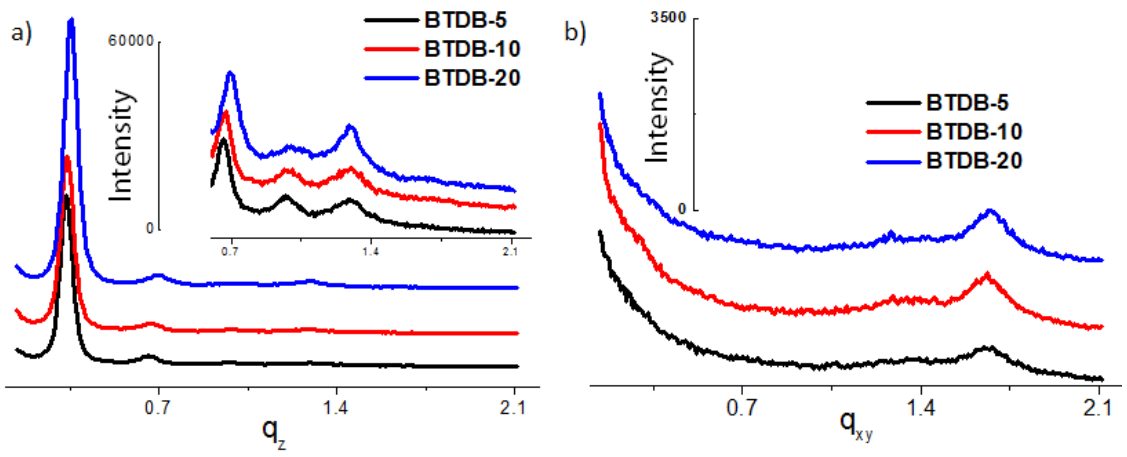

Figure 4.17. 1D GIXRD patterns of the annealed thin films of **BTDB**s. a) Out-of-plane and b) in-plane [Inset of a) shows zoomed region].

In the in-plane direction, thin films of **TDB-5**, **TDB-10**, and **TDB-20** display one weak diffraction at q_{xy} = 0.27 Å^{-1}, corresponding to a *d*-spacing of ~ 23.3 Å. The appearance of both out-of-plane and in-plane diffractions for the side alkyl chains implies the coexistence of edge-on and face-on packing modes within thin films of **TDB-5**, **TDB-10**, and **TDB-20**. The diffraction intensities at q_z = 0.31 Å^{-1} for **TDB-10** and **TDB-20** are relatively higher than that for **TDB-5**. These diffraction data reveal that the incorporation of BTBT units in the backbones is beneficial for improving the interchain packing order. This agrees well with the observation that hole mobilities increase by incorporating more BTBT units in the polymer backbones (Table 4.2). In the out-of- plane direction, the thermally annealed thin film of **BTDB-5** shows diffractions up to fourth order at q_z = 0.33, 0.66, 0.97, and 1.30 Å^{-1}, which correspond to a *d*-spacing of ~ 19.0 Å. Thin films of **BTDB-10** and **BTDB-20** exhibit almost the same diffractions up to fourth order in the out of-plane direction as shown

in Figure 4.17a. Thus, the lamellar stacking of alkyl chains are more ordered for **BTDB-5**, **BTDB-10**, and **BTDB-20** in comparison with **TDB-5**, **TDB-10**, and **TDB-20**. Furthermore, weak diffraction at q_{xy} = 1.68 $Å^{-1}$, corresponding to π-π stacking of ~ 3.7 Å, was observed for thin films of **BTDB-5**, **BTDB-10**, and **BTDB-20** (Figure 4.17b). Thus, polymer chains of **BTDB-5**, **BTDB-10**, and **BTDB-20** mainly adopt the edge-on packing mode in their thin films. These diffraction data reveal that the incorporation of rigid planar chalcogenophene (BTBT) in the backbones favors the efficient packing of alkyl chains and enhance the interchain π-π interactions. It is noted that the *d*-spacing for the lamellar packing of alkyl chains for **BTDB**s is slightly different from that for **TDB**s although two series of polymers possess the same alkyl chains. This may be explained by considering the fact that the backbones of two series of polymers are different, which can lead to different interchain packing and with different degree of alkyl chain interdigitation.

Figure 4.18 shows AFM images of thin films of **TDB-5**, **TDB-10**, **TDB-20**, **BTDB-5**, **BTDB-10**, and **BTDB-20** after thermal annealing at 100 °C. The root-mean-square roughnesses (R_{RMS}) were 0.33, 0.39, and 0.42 nm for thermally annealed thin films of **TDB-5**, **TDB-10**, and **TDB-20**, respectively, whereas those for thin films of **BTDB-5 BTDB-10**, and **BTDB-20** were 1.41, 1.55, and 2.67 nm, respectively. Sizes of domains are increased with increasing BTBT contents for both **TDB**s copolymers and **BTDB**s copolymers, especially for **BTDB**s copolymers. Furthermore, the domains were more interconnected for thin films of **BTDB-10** and **BTDB-20** which contain more chalcogenophene (BTBT) in the backbones. In fact, extended nanoscale domains are observed while increasing the percentage of BTBT

unit in the polymer backbone. Interconnected crystalline domains are essential requirement for the efficient charge carrier transport. Hence, AFM images are consistent with the observation that thin film hole mobility of these conjugated polymers are enhanced by incorporating more chalcogenophene (BTBT) in the backbones.

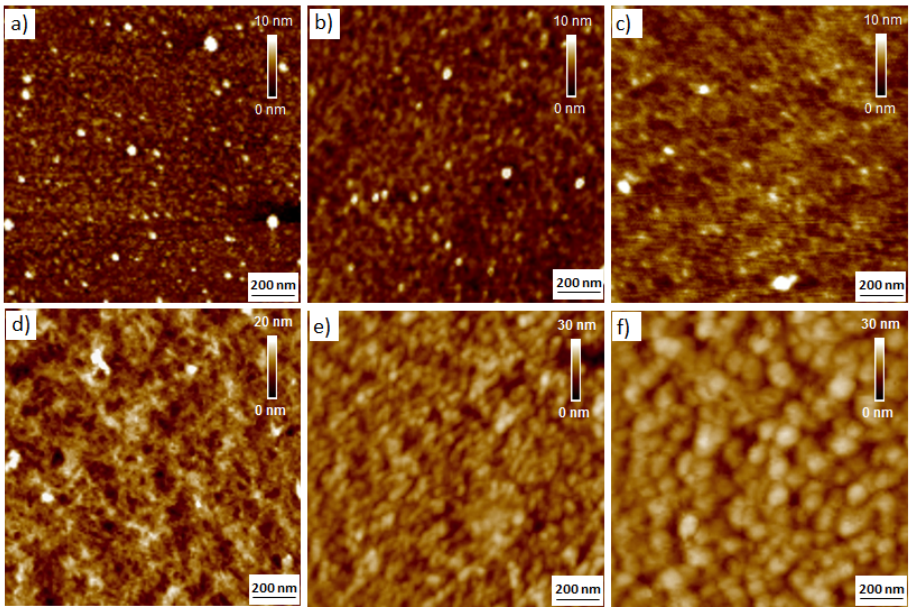

Figure 4.18. Tapping mode AFM images of annealed thin films of a) **TDB-5**, b) **TDB-10**, c) **TDB-20**, d) **BTDB-5**, e) **BTDB-10** and f) **BTDB-20** (Polymer films were made by spin coating the *o*-DCB solutions on OTS modified SiO_2/Si substrate).

4.4. Conclusions

In summary, we report new conjugated D-A polymers with diketopyrrolopyrrole (DPP) as the electron acceptor and thiophene or bithiophene together with [1]benzothieno[3,2-*b*]benzothiophene (BTBT) as co-electron donors. The ratios of DPP vs BTBT are varied in order to study the effect of the fused chalcogenophene on

the molecular packing of polymers in thin films and its simultaneous impact on the charge carrier transport properties in field effect transistors (FETs). All the polymers exhibit *p*-type semiconducting characteristics in bottom gate/bottom contact (BG/BC) device configuration. Thermally annealed devices exhibited high hole mobility (μ_h) up to 2.47 $cm^2V^{-1}s^{-1}$ with increasing the BTBT percentage in the polymer chain. Further work includes improving the solubility of polymers by introducing longer side chains in the DPP units and optimization of the thin film morphologies of the polymers for enhancing the charge carrier mobility.

4.5. Experimental Section

4.5.1. Synthesis and Characterization

Unless otherwise stated, all the starting materials and reagents were purchased from commercial sources and used without any further purification. High temperature ^{1}H NMR spectra were recorded on Bruker AVANCE III 500 MHz spectrometer. Elemental analysis was performed on a Carlo Erba model 1160 elemental analyzer. The number-average molecular weight (M_n), weight-average molecular weight (M_w) and polydispersity index (PDI = M_w/ M_n) of all polymers were determined by gel permeation chromatography (GPC) at 150 °C using polystyrenes as standards with 1,2,4-trichlorobenzene as the eluent.

2,7-Diiodo[1]benzothieno[3,2-*b*]benzothiophene was readily prepared by reported procedures.[38,46,52] 3,6-Bis(5-bromothiophen-2-yl)-2,5-bis(2-octyldodecyl) pyrrolo[3,4-*c*]pyrrole-1,4(2H,5H)-dione, 2,5-bis(trimethylstannyl)thiophene and 5,5′-bis(trimethylstannyl)-2,2′-bithiophene were commercially available and used without

further purification. Stille coupling of 2,7-diiodo[1]benzothieno[3,2-*b*]benzothiophene with the corresponding stannyl derivatives of heteroarenes and bromothiophen-2-yl)-2,5-bis(2-octyldodecyl)pyrrolo[3,4-*c*]pyrrole-1,4(2H,5H)-dione yield required polymers.

Synthesis of 4,4'-dinitrostilbene-2,2'-disulphonyl chloride (**12**): Solid mixture of disodium 4,4'-dinitrostilbene-2,2'-disulfonate (**11**) (3 g, 6.32 mmol) and phosphorous pentachloride (6 g, 28.81 mmol) was heated at 120 ^{o}C for 2 h, cooled and decomposed by the addition of finely crushed ice. The precipitate was filtered, washed with water and dried under vacuum. For purification, the product was dissolved in chloroform, the solution was passed through a layer of silica gel, the light yellow solution was concentrated and residue was washed with a small amount of ether. Compound was recrystallized from chloroform as light yellow solid. Yield-65%; m.p.: 248 ± 2 ^{o}C; ^{1}H NMR (500 MHz; CCl_4, TMS) δ (ppm): 7.31 (s, vinylic), 7.95 (d, 2H, aromatic) 8.4 (d, 2H, aromatic), 8.7 (s, 2H, aromatic); ^{13}C NMR (125 MHz; $CDCl_3$) δ (ppm): 124.35, 127.41, 128.52, 130.61, 139.33, 142.79, 148.31; EI-MS: 467.2 (M^+); Calculated elemental composition for $C_{14}H_8Cl_2N_2O_8S_2$: C, 35.99; H, 1.73; N, 6.00; S, 13.72; found: C, 35.97; H, 1.73; N, 6.01; S, 13.72.

Synthesis of 4,4'-dinitrostilbene-2,2'-dithiol (**13**): To a suspension of disulfonyl chloride (**12**) (2 g, 4.28 mmol) in acetic acid, heated at 100 ^{o}C, added 60 mL 55 % hydroiodic acid. The mixture was left at 20 ^{o}C for 12 h. It was then diluted with water and decolorized with a solution of sodium bisulfite. The yellow precipitate filtered off, washed with water and dried. Yield-57%; m.p.: 212 ± 2 ^{o}C; ^{1}H NMR (500 MHz; Methanol-d_4, TMS) δ (ppm): 7.28 (s, vinylic), 7.52 (d, 2H, aromatic) 7.86 (d, 2H,

aromatic), 8.04 (s, 2H, aromatic); ^{13}C NMR (125 MHz; Methanol-d_4) δ (ppm): 120.63, 121.11, 125.92, 127.40, 127.60, 134.18, 147.44; EI-MS: 334.36 (M^+); Calculated elemental composition for $C_{14}H_{10}N_2O_4S_2$: C, 50.29; H, 3.01; N, 8.38; S, 19.18; found: C, 50.27; H, 3.01; N, 8.38; S, 19.18.

Synthesis of 2,7-dinitro[1]benzothieno[3,2-*b*][1]benzothiophene (**14**): Dithiol (**13**) (2 g, 5.98 mmol) was suspended in acetic acid, and to this was added bromine (2 mL) and boiled for 2 h. The solution is cooled and washed with dil. NaOH. Compound is obtained after filtration as yellow solid. Yield-73%; m.p.: > 300 ºC; ^{1}H NMR (500 MHz; $CDCl_3$, TMS) δ (ppm): 8.26 (d, 2H, aromatic) 8.61 (d, 2H, aromatic), 8.88 (s, 2H, aromatic); ^{13}C NMR (125 MHz; $CDCl_3$) δ (ppm): 117.72, 119.42, 122.70, 124.10, 140.82, 144.34, 145.92; EI-MS: 330.33 (M^+); Calculated elemental composition for $C_{14}H_6N_2O_4S_2$: C, 50.90; H, 1.83; N, 8.48; S, 19.41; found: C, 50.92; H, 1.83; N, 8.48; S, 19.42.

Synthesis of 2,7-diamino[1]benzothieno[3,2-*b*][1]benzothiophene (**15**): Compound **14** (1 g, 3.03 mmol) and tin powder (0.9 g, 7.58 mmol) were added to acetic acid and heated. Then the 5 mL con. HCl was added gradually. Mixture is heated for 2 h. 2,7-Diamino[1]benzothieno[3,2-*b*][1]benzothiophene was obtained as a white precipitate. Compound is filtered and dried under vacuum. Yield-80%; m.p.: > 300 ºC; ^{1}H NMR (500 MHz; THF-d_8, TMS) δ (ppm): 7.45 (d, 2H, aromatic) 7.66 (s, 2H, aromatic), 8.12 (d, 2H, aromatic); ^{13}C NMR (125 MHz; THF-d_8) δ (ppm): 109.25, 110.96, 122.70, 124.04, 129.86, 140.72, 142.63; EI-MS: 270.37 (M^+); Calculated elemental composition for $C_{14}H_{10}N_2S_2$: C, 62.19; H, 3.73; N, 10.36; S, 23.72; found: C, 62.23; H, 3.72; N, 10.36; S, 23.73.

Synthesis of 2,7-diiodo[1]benzothieno[3,2-*b*][1]benzothiophene (**16**): To an ice-cooled mixture of 2,7-diamino[1]benzothieno[3,2-*b*][1]benzothiophene (1.0 g, 3.7 mmol), sulfuric acid (2 mL) in ethanol , aqueous sodium nitrite solution (624 mg, 9 mmol in water 10 mL) is added below 5 ºC. After the mixture was stirred for 1 h, aqueous potassium iodide (3.1 g, 19 mmol in water 40 mL) was added, and the resulting mixture was refluxed for 3 h. Sodium hydrogen sulfite was added to reduce liberated iodine, and the resulting precipitate was collected by filtration, washed with methanol, and dried. Extraction by refluxing chloroform from the crude product gave **16** as pale yellow solid. Pure compound is obtained by the recrystallization from *o*-dichlorobenzene. Yield-60 %; m.p.: > 300 ºC; ^{1}H NMR (500 MHz; $CDCl_3$, TMS) δ (ppm) 8.26 (d, J = 1.4 Hz, 2H), 7.75 (dd, J = 1.4, 8.4 Hz, 2H), 8.16 (d, J = 8.4 Hz, 2H); ^{13}C NMR (125 MHz; $CDCl_3$) δ (ppm): 113.22, 122.70, 124.83, 131.55, 135.51, 138.72, 141.56; EI-MS: 492 (M^+); Calculated elemental composition for $C_{14}H_6I_2S_2$: C, 34.17; H, 1.23; found: C, 34.13; H, 1.18.

Synthesis of TDBs. 2,7-Diiodo[1]benzothieno[3,2-*b*]benzothiophene (**16**), 3,6-dibromo thiophen-2-yl-*N*,*N*-bis(2-octyldodecyl)-1,4-dioxopyrrolo[3,4-*c*]pyrrole (**17**) and 2,5-bis(trimethylstannyl)thiophene were taken in a Schlenk tube under nitrogen atmosphere with 10 mL of anhydrous toluene. Tris(dibenzylideneacetone)dipalladium (0) ($Pd_2(dba)_3$) and tri(*o*-tolyl)phosphine (P(*o*-tol)$_3$) were added in one portion. The tube was charged with nitrogen through a freeze-pump-thaw cycle for three times. The reaction was stirred at 90 °C for 48 h under nitrogen atmosphere. Then, a toluene solution of tributyl(phenyl)stannane was added, and the mixture was stirred for an additional 2 h, followed by the addition of a few drops of bromobenzene and further

stirring for 2 h. The resulting mixture was poured into methanol and stirred for 3 h. The dark precipitate was filtered off and subjected to Soxhlet extraction for 48 h successively with methanol, acetone, hexane and chloroform for the removal of remaining monomers, oligomers, and catalytic impurities. The remaining precipitate dried under vacuum at 50 ^{o}C and used for the characterization.

For synthesis of TDB-5. Compound **16** (5 mg, 0.01 mmol), **17** (194 mg, 0.19 mmol) and 2,5-bis(trimethylstannyl)thiophene (82 mg, 0.2 mmol), P(*o*-tolyl)$_3$ (6 mg, 0.02 mmol), and $Pd_2(dba)_3$ (9 mg, 0.01 mmol) were used. Polymer was obtained as dark blue solid (146 mg, 80% yield). ^{1}H NMR (500 MHz; 1,1,2,2-tetrachloroethane-d_2; 100 ^{o}C) δ (ppm): 0.83 (m, br), 1.34-1.22 (m, br), 1.95 (m, br), 3.98 (m, br), 7.22-6.88 (m, br), 8.84 (m, br); GPC: M_n = 43000, M_w = 130000, PDI = 3.0; Calculated elemental composition for $(C_{56}H_{84}N_{1.9}O_{1.9}S_3)_n$: C, 73.87; H, 9.30; N, 2.92; S, 3.34; found: C, 73.65; H, 9.34; N, 2.93; S, 3.33.

For synthesis of TDB-10. Compound **16** (10 mg, .02 mmol), **17** (183 mg, 0.18 mmol) and 2,5-bis(trimethylstannyl)thiophene (82 mg, 0.2 mmol), P(*o*-tolyl)$_3$ (6 mg, 0.02 mmol), and $Pd_2(dba)_3$ (9 mg, 0.01 mmol) were used. Polymer was obtained as dark blue solid (123 mg, 70% yield).^{1}H NMR (500 MHz; 1,1,2,2-tetrachloroethane-d_2; 100 ^{o}C) δ (ppm): 0.87 (m, br), 1.34-1.22 (m, br), 1.95 (m, br), 3.97 (m, br), 7.03-6.88 (m, br), 8.83 (m, br); GPC: M_n = 38000, M_w = 127000, PDI = 3.3; Calculated elemental composition for $(C_{54}H_{80}N_{1.8}O_{1.8}S_3)_n$: C, 73.75; H, 9.17; N, 2.87; S, 10.94; found: C, 73.60; H, 9.12; N, 2.88; S, 10.95.

For synthesis of TDB-20. Compound **16** (20 mg, 0.04 mmol), **17** (163 mg, 0.16 mmol) and 2,5-bis(trimethylstannyl)thiophene (82 mg, 0.2 mmol), P(o-tolyl)$_3$ (6 mg,

0.02 mmol), and $Pd_2(dba)_3$ (9 mg, 0.01 mmol) were used. Polymer was obtained as dark blue solid (140 mg, 85% yield). ^{1}H NMR (500 MHz; 1,1,2,2-tetrachloroethane-d_2; 100 ^{o}C) δ (ppm): 0.85 (m, br), 1.34-1.25 (m, br), 1.95 (m, br), 3.99 (m, br), 7.15 (m, br), 8.79 (m, br); GPC: M_n = 46000, M_w = 140000, PDI = 3.0; Calculated elemental composition for $(C_{50}H_{72}N_{1.6}O_{1.6}S_3)_n$: C, 73.48; H, 8.88; N, 2.74;S, 11.77; found: C, 73.77; H, 8.89; N, 2.74; S, 11.82.

Synthesis of BTDBs. Similar procedure as for **TDB**s is followed while instead of 2,5-bis(trimethylstannyl)thiophene, 5,5′-bis(trimethylstannyl)-2,2′-bithiophene has been used.

For synthesis of BTDB-5. Compound **16** (10 mg, 0.02 mmol), **17** (387 mg, 0.38 mmol) and 5,5′-bis(trimethylstannyl)-2,2′-bithiophene (197 mg, 0.4 mmol), P(*o*-tolyl)$_3$ (12 mg, 0.04 mmol), and $Pd_2(dba)_3$ (18 mg, 0.02 mmol) were used. Polymer was obtained as dark blue solid (308 mg, 77% yield).^{1}H NMR (500 MHz; 1,1,2,2-tetrachloroethane-d_2; 100 ^{o}C) δ (ppm): 0.83 (m, br), 1.57-1.22 (m, br), 1.97 (m, br), 3.98 (m, br), 7.02-6.89 (m, br), 8.79 (m, br); GPC: M_n = 38000, M_w =103000, PDI = 2.7; Calculated elemental composition for $(C_{60}H_{86}N_{1.9}O_{1.9}S_4)_n$: C, 72.60; H, 8.73; N, 2.68;S, 12.92; found: C, 72.16; H, 8.70; N, 2.67; S, 12.91.

For synthesis of BTDB-10. Compound **16** (15 mg, 0.03 mmol), **17** (275 mg, 0.27 mmol) and 5,5′-bis(trimethylstannyl)-2,2′-bithiophene (148 mg, 0.3 mmol), P(*o*-tolyl)$_3$ (9 mg, 0.03 mmol), and $Pd_2(dba)_3$ (14 mg, 0.015 mmol) were used. Polymer was obtained as dark blue solid (202 mg, 70% yield).^{1}H NMR (500 MHz; 1,1,2,2-tetrachloroethane-d_2; 100 ^{o}C) δ (ppm): 0.83 (m, br), 1.34-1.22 (m, br), 1.95 (m, br), 3.99 (m, br), 7.30-7.05 (m, br), 8.74 (m, br); GPC: M_n = 64000, M_w =240000, PDI =

3.8; Calculated elemental composition for $(C_{58}H_{82}N_{1.8}O_{1.8}S_4)_n$: C, 72.45; H, 8.60; N, 2.62;S, 13.34; found: C, 72.38; H, 8.57; N, 2.63; S, 13.27.

For synthesis of BTDB-20. Compound **16** (30 mg, 0.06 mmol), **17** (245 mg, 0.24 mmol) and 5,5′-bis(trimethylstannyl)-2,2′-bithiophene (148 mg, 0.3 mmol), P(*o*-tolyl)$_3$ (9 mg, 0.03 mmol), and $Pd_2(dba)_3$ (14 mg, 0.015 mmol) were used. Polymer was obtained as dark blue solid (225 mg, 83% yield).^{1}H NMR (500 MHz; 1,1,2,2-tetrachloroethane-d_2; 100 ^{o}C) δ (ppm): 0.83 (m, br), 1.34-1.22 (m, br), 1.95 (m, br), 3.98 (m, br), 7.37-6.97 (m, br), 8.74 (m, br); GPC: M_n = 51300, M_w = 230000, PDI = 4.5; Calculated elemental composition for $(C_{54}H_{74}N_{1.6}O_{1.6}S_4)_n$: C, 72.11; H, 8.29; N, 2.49;S, 14.26; found: C, 72.33; H, 8.26; N, 2.49; S, 14.32.

4.5.2. Characterization of Polymers

Solution and thin film absorption spectra were measured with JASCO V-570 UV-vis spectrophotometer. TGA (SHIMADZU DTG-60) measurements were performed under nitrogen atmosphere at a heating rate of 10 K/min. A conventional three-electrode cell was used for the cyclic voltammetric measurements. Platinum is used as working and counter electrodes, and an Ag/AgCl (saturated KCl) reference electrode are used in a computer-controlled CHI660C instruments at room temperature. Films were prepared by drop-casting *o*-dichlorobenzene (*o*-DCB) solution of polymers on the working electrode. All the measurements were done in anhydrous acetonitrile with *n*-tetrabutylammonium hexafluorophosphate (*n*-Bu_4NPF_6) as the conducting electrolyte. The GIXRD data were obtained at beamline of BL14B1 of the Shanghai Synchrotron Radiation Facility (SSRF). Polymer thin film surfaces

were examined under ambient conditions using NTEGRA (NT-MDT) operating under a tapping mode regime.

4.5.3. Fabrication of OFET Devices

A heavily doped *n*-type Si wafer and a layer of dry oxidized SiO_2 (300 nm, with roughness lower than 0.1 nm and capacitance of 11 $nFcm^{-2}$) were used as a gate electrode and gate dielectric layer, respectively. The drain-source (D-S) gold contacts were fabricated by photolithography. The substrates were cleaned in water, deionized water, isopropanol, and rinsed in acetone. Then, the surface was modified with *n*-octadecyltrichlorosilane (OTS). After that, the substrates were cleaned in *n*-hexane, $CHCl_3$ and isopropanol sequentially. Polymers were dissolved in hot *o*-dichlorobenzene (3 mg/mL) and spin-coated on above substrates at 2000 rpm for 60 s. The annealing process was carried out in vacuum for 2 h at each temperature. In all the devices channel length (L) and width (W) were 50 μm and 1400 μm, respectively. Field-effect characteristics of the devices were determined in air by using a Keithley 4200 SCS semiconductor parameter analyzer. Hole mobility (μ_h) of all the field effect transistors was calculated by fitting a straight line to the plot of the square root of I_{DS} vs V_G in the saturation region using the equation.

4.6. References

1. Wang, C. L., Dong, H. L., Hu, W. P., Liu, Y. Q., Zhu, D. *Chem. Rev*. **2012**, *112*, 2208-2267.
2. Forrest, S. R. *Nature* **2004**, *428*, 911-918.

3. Sirringhaus, H. *Adv. Mater*. **2014**, *26*, 1319-1335.
4. Mei, J., Diao, Y., Appleton, A. L., Fang, L., Bao, Z. *J. Am. Chem. Soc*. **2013**, *135*, 6724-6746.
5. Tsumura, A., Koezuka, H., Ando, T. *Appl. Phys. Lett*. **1986**, *49*, 1210-1212.
6. Guo, X., Facchetti, A., Marks, T. J. *Chem. Rev*. **2014**, *114*, 8943-9021.
7. Zhao, X., Zhan, X. *Chem. Soc. Rev*. **2011**, *40*, 3728-3743.
8. Sirringhaus, H., Kawase, T., Friend, R. H., Shimoda, T., Inbasekaran, M., Wu, W., Woo, E. P. *Science* **2000**, *290*, 2123-2126.
9. Katz, H. E., Bao, Z. *J. Phys. Chem. B* **2000**, *104*, 671-678.
10. Garnier, F., Hajlaoui, R., Yassar, A., Srivastava, P. *Science* **1994**, *265*, 1684-1686.
11. Wu, W., Liu, Y., Zhu, D. *Chem. Soc. Rev*. **2010**, *39*, 1489-1502.
12. Kang, I., Yun, H.-J., Chung, D. S., Kwon, S.-K., Kim, Y.-H. *J. Am. Chem. Soc*. **2013**, *135*, 14896-14899.
13. Brédas, J.-L., Beljonne, D., Coropceanu, V., Cornil, J. *Chem. Rev*. **2004**, *104*, 4971-5004.
14. Fei, Z., Pattanasattayavong, P., Han, Y., Schroeder, B. C., Yan, F., Kline, R. J., Anthopoulos, T. D., Heeney, M. *J. Am. Chem. Soc*. **2014**, *136*, 15154-15157.
15. Brédas, J. L., Calbert, J. P., da Silva Filho, D. A., Cornil, J. *Proc. Natl. Acad. Sci. U. S. A*. **2002**, *99*,5804-5809.
16. Bromley, S. T., Torrent, M. M., Hadley, P., Rovira, C. *J. Am. Chem. Soc*. **2004**, *126*, 6544-6545.
17. Balan, B., Vijayakumar, C., Saeki, A., Koizumi, Y., Seki, S. *Macromolecules* **2012**, *45*, 2709-2719.

18. Babu, S. S., Prasanthkumar, S., Ajayaghosh, A. *Angew. Chem., Int. Ed*. **2012**, *51*, 1766-1776.

19. Saeki, A., Fukumatsu, T., Seki, S. *Macromolecules* **2011**, *44*, 3416-3424.

20. Yagi, S., Ezoe, M., Yonekura, I., Takagishi, T., Nakazumi, H. *J. Am. Chem. Soc*. **2003**, *125*, 4068-4069.

21. Hutchison, G. R., Ratner, M. A., Marks, T. J. *J. Am. Chem. Soc*. **2005**, *127*, 2339-2350.

22. da Silva Filho, D. A., Kim, E.-G., Brédas, J.-L. *Adv. Mater*. **2005**, *17*, 1072-1076.

23. Lee, J., Han, A.-R., Yu, H., Shin, T. J., Yang, C., Oh, J. H. *J. Am. Chem. Soc*. **2013**, *135*, 9540-9547.

24. Lei, T., Dou, J.-H., Cao, X.-Y., Wang, J.-Y., Pei, J. *J. Am. Chem. Soc*. **2013**, *135*, 12168-12171.

25. Zhang, F., Hu, Y., Schuettfort, T., Di, C., Gao, X., McNeill, C. R., Thomsen, L., Mannsfeld, S. C. B., Yuan, W., Sirringhaus, H., Zhu, D. *J. Am. Chem. Soc*. **2013**, *135*, 2338-2349.

26. Tsao, H. N., Cho, D. M., Park, I., Hansen, M. R., Mavrinskiy, A., Yoon, D. Y., Graf, R., Pisula, W., Spiess, H. W., Müllen, K. *J. Am. Chem. Soc*. **2011**, *133*, 2605-2612.

27. Cai, Z., Luo, H., Qi, P., Wang, J., Zhang, G., Liu, Z., Zhang, D. *Macromolecules* **2014**, *47*, 2899-2906.

28. Lei, T., Wang, J.-Y., Pei, J. *Acc. Chem. Res*. **2014**, *47*, 1117-1126.

29. Varma, P. C. R., Namboothiry, M. A. G. *Phys. Chem. Chem. Phys*. **2016**, *18*, 3438-3443.

30. Bronstein, H., Chen, Z., Ashraf, R. S., Zhang, W., Du, J., Durrant, J. R., Tuladhar, P. S., Song, K., Watkins, S. E., Geerts, Y., Wienk, M. M., Janssen, R. A. J., Anthopoulos, T., Sirringhaus, H., Heeney, M., McCulloch, I. *J. Am. Chem. Soc*. **2011**, *133*, 3272-3275.
31. Li, J., Zhao, Y., Tan, H. S., Guo, Y., Di, C. -A., Yu, G., Liu, Y., Lin, M., Lim, S. H., Zhou, Y., Su, H., Ong, B. S. *Sci. Rep*. **2012**, *2*, 754.
32. Kang, T. E., Choi, J., Cho, H.-H., Yoon, S. C., Kim, B. J. *Macromolecules* **2016**, *49*, 2096-2105.
33. Liu, Z., Zhang, G., Cai, Z., Chen, X., Luo, H., Li, Y., Wang, J., Zhang, D. *Adv. Mater*. **2014**, *26*, 6965-6977.
34. Yi, Z., Wang, S., Liu, Y. *Adv. Mater*. **2015**, *27*, 3589-3606.
35. Sonar, P., Singh, S. P., Li, Y., Soh, M. S., Dodabalapur, A. *Adv. Mater*. **2010**, *22*, 5409-5413.
36. Bijleveld, J. C., Zoombelt, A. P., Mathijssen, S. G. J., Wienk, M. M., Turbiez, M., de Leeuw, D. M., Janssen, R. A. J. *J. Am. Chem. Soc*. **2009**, *131*, 16616-16617.
37. Li, J., Ong, K.-H., Lim, S.-L., Ng, G.-M., Tan, H.-S., Chen, Z.-K. *Chem. Commun*. **2011**, *47*, 9480-9482.
38. Bürgi, L., Turbiez, M., Pfeiffer, R., Bienewald, F., Kirner, H.-J., Winnewisser, C. *Adv. Mater*. **2008**, *20*, 2217-2224.
39. Li, Y., Sonar, P., Murphy, L., Hong, W. *Energy Environ. Sci*. **2013**, *6*, 1684-1710.
40. Back, J. Y., Yu, H., Song, I., Kang, I., Ahn, H., Shin, T. J., Kwon, S.-K., Oh, J. H., Kim, Y.-H. *Chem. Mater*. **2015**, *27*, 1732-1739.

41. Yi, Z., Sun, X., Zhao, Y., Guo, Y., Chen, X., Qin, J., Yu, G., Liu, Y. *Chem. Mater*. **2012**, *24*, 4350-4356.

42. Kang, I., An, T. K., Hong, J.-a., Yun, H. -J., Kim, R., Chung, D. S., Park, C. E., Kim, Y.-H., Kwon, S. -K. *Adv. Mater*. **2013**, *25*, 524-528.

43. Cho, M. J., Shin, J., Yoon, S. H., Lee, T. W., Kaur, M., Choi, D. H. *Chem. Commun*. **2013**, *49*, 7132-7134.

44. Yao, J., Yu, C., Liu, Z., Luo, H., Yang, Y., Zhang, G., Zhang, D. *J. Am. Chem. Soc*. **2016**, *138*, 173-185.

45. Kim, D.H., Lee, B.-L., Moon, H., Kang, H. M., Jeong, E. J., Park, J.-I., Han, K. -M., Lee, S., Yoo, B. W., Koo, B. W., Kim, J. Y., Lee, W. H., Cho, K., Becerril, H. A., Bao, Z. *J. Am. Chem. Soc*. **2009**, *131*, 6124-6132.

46. Li, W., Hendriks, K. H., Furlan, A., Roelofs, W. S. C., Wienk, M. M., Janssen, R. A. J. *J. Am. Chem. Soc*. **2013**, *135*, 18942-18948.

47. Garnier, F., Yassar, A., Hajlaoui, R., Horowitz, G., Deloffre, F., Servet, B., Ries, S., Alnot, P. *J. Am. Chem. Soc*. **1993**, *115*, 8716-8721.

48. Takimiya, K., Shinamura, S., Osaka, I., Miyazaki, E. *Adv. Mater*. **2011**, *23*, 4347-4370.

49. Zhang, X., Richter, L. J., DeLongchamp, D. M., Kline, R. J., Hammond, M. R., McCulloch, I., Heeney, M., Ashraf, R. S., Smith, J. N., Anthopoulos, T. D., Schroeder, B., Geerts, Y. H., Fischer, D. A., Toney, M. F. *J. Am. Chem. Soc*. **2011**, *133*, 15073-15084.

50. Takimiya, K., Ebata, H., Sakamoto, K., Izawa, T., Otsubo, T., Kunugi, Y. *J. Am. Chem. Soc*. **2006**, *128*, 12604-12605.

51. Ebata, H., Izawa, T., Miyazaki, E., Takimiya, K., Ikeda, M., Kuwabara, H., Yui, T. *J. Am. Chem. Soc*. **2007**, *129*, 15732-15733.

52. Minemawari, H., Yamada, T., Matsui, H., Tsutsumi, J., Haas, S., Chiba, R., Kumai, R., Hasegawa, T. *Nature* **2011**, *475*, 364-367.

53. Um, M.-C., Kwak, J., Hong, J.-P., Kang, J., Yoon, D. Y., Lee, S. H., Lee, C., Hong, J.-I. *J. Mater. Chem*. **2008**, *18*, 4698-4703.

54. Yuan, Y., Giri, G., Ayzner, A. L., Zoombelt, A. P., Mannsfeld, S. C. B., Chen, J., Nordlund, D., Toney, M. F., Huang, J., Bao, Z. *Nat. Commun*. **2014**, *5*, 3005.

55. Takimiya, K., Osaka, I., Mori, T., Nakano, M. *Acc. Chem. Res*. **2014**, 47, 1493-1502.

56. Osaka, I., Abe, T., Shinamura, S., Miyazaki, E., Takimiya, K. *J. Am. Chem. Soc*. **2010**, *132*, 5000-5001.

57. Zherdeva, S. Y., Barudi, A., Zheltov, A. Y., Stepanov, B. I. *Zh. Org. Khim*. **1980**, *16*, 430-438.

58. Meager, I., Ashraf, R. S., Mollinger, S., Schroeder, B. C., Bronstein, H., Beatrup, D., Vezie, M. S., Kirchartz, T., Salleo, A., Nelson, J., McCulloch, I. *J. Am. Chem. Soc*. **2013**, *135*, 11537-11540.

59. Zhou, X., Ai, N., Guo, Z.-H., Zhuang, F.-D., Jiang, Y.-S., Wang, J.- Y., Pei, J. *Chem. Mater*. **2015**, *27*, 1815-1820.

60. Liu, Y., Zhao, J., Li, Z., Mu, C., Ma, W., Hu, H., Jiang, K., Lin, H., Ade, H., Yan, H. *Nat. Commun*. **2014**, *5*, 5293.

61. Henson, Z. B., Zhang, Y., Nguyen, T.-Q., Seo, J. H., Bazan, G. C. *J. Am. Chem. Soc*. **2013**, *135*, 4163-4166.

62. Li, Y., Singh, S. P., Sonar, P. A. *Adv. Mater*. **2010**, *22*, 4862-4866.

63. Cai, Z., Guo, Y., Yang, S., Peng, Q., Luo, H., Liu, Z., Zhang, G., Liu, Y., Zhang, D. *Chem. Mater*. **2013**, *25*, 471-478.

64. Venkateshvaran, D., Nikolka, M., Sadhanala, A., Lemaur, V., Zelazny, M., Kepa, M., Hurhangee, M., Kronemeijer, A. J., Pecunia, V., Nasrallah, I., Romanov, I., Broch, K., McCulloch, I., Emin, D., Olivier, Cornil, J., Beljonne, D., Sirringhaus, H. *Nature* **2014**, *515*, 384-388.

65. Chen, Z., Lee, M. J., Ashraf, R. S., Gu, Y., Albert-Seifried, S., Nielsen, M. M., Schroeder, B., Anthopoulos, T. D., Heeney, M., McCulloch, I., Sirringhaus, H. *Adv. Mater*. **2012**, *24*, 647-652.

66. Chen, H., Guo, Y., Yu, G., Zhao, Y., Zhang, J., Gao, D., Liu, H., Liu, H. *Adv. Mater*. **2012**, *24*, 4618-4622.

67. Yang, H., Zhang, R., Wang, L., Zhang, J., Yu, X., Liu, J., Xing, R., Geng, Y., Han, Y. *Macromolecules* **2015**, *48*, 7557-7566.

List of Publications

1. Cyclotriphosphazene Appended Porphyrins And Fulleropyrrolidine Complexes as Supramolecular Multiple Photosynthetic Reaction Centers: Steady And Excited States Photophysical Investigation. **Nair, V. S**., Pareek, Y., Karunakaran, V., Ravikanth, M., & Ajayaghosh, A.

   Phys.Chem.Chem.Phys., **2014**, *16*, 10149-10156.

2. Conjugated Random Donor-Acceptor Copolymers of [1]Benzothieno [3,2-*b*] benzothiophene and Diketopyrrolopyrrole Units for High Performance Polymeric Semiconductor Applications. **Nair, V. S**., Sun, J., Qi, P., Yang, S., Liu, Z., Zhang, D., & Ajayaghosh, A.

   Macromolecules, **2016**, *49*, 6334-6342.

3. A π-gel scaffold for assembling fullerene to photoconducting supramolecular rods. **Nair, V. S**., Mukhopadhyay, R. D., Saeki, A., Seki, S., & Ajayaghosh, A.

   Sci. Adv. **2016**, *2*, e1600142.

4. Formation of Coaxial Nanocables with Amplified Supramolecular Chirality through an Interaction between Carbon Nanotubes and a Chiral π-Gelator. Vedhanarayanan, B., **Nair, V. S**., Nair, V. C., & Ajayaghosh, A.

   Angew. Chem. Int. Ed. **2016**, *55*, 10345-10349.

Papers Presented at Conferences (Posters/Oral)

1. Hybrid Donor-Acceptor Assembly for Improved Charge Carrier Generation. **V. S. Nair**, K. K. Kartha & A. Ajayaghosh.

   A Poster Presented at 2nd TAPSUN Conference, CSIR-CLRI, Chennai, India. 2013, September 13-14.

2. Assembly of C_{60} to Photoconducting Supramolecular Rods in a π-Gel Medium. **V. S. Nair**, R. D. Mukhopadhyay & A. Ajayaghosh.

   Oral presentation at 12th JNC Research Conference on Chemistry of Materials, Trivandrum, Kerala, India, 2016, September 23-15.

3. Diketopyrrolopyrrole and [1]Benzothieno[3,2-*b*]benzothiophene Containing Donor-Acceptor Copolymers for Organic Field Effect Transistors. **V. S. Nair** & A. Ajayaghosh.

   A Poster Presented at Indo-Japan Joint Symposium on Polymeric Materials, Trivandrum, Kerala, India, 2017, January 31- February 1.